Acoustofluidic Levitation in Organoid Cultures

Tuning Ultrasound to Cluster Cells

Pradnya Gharpure

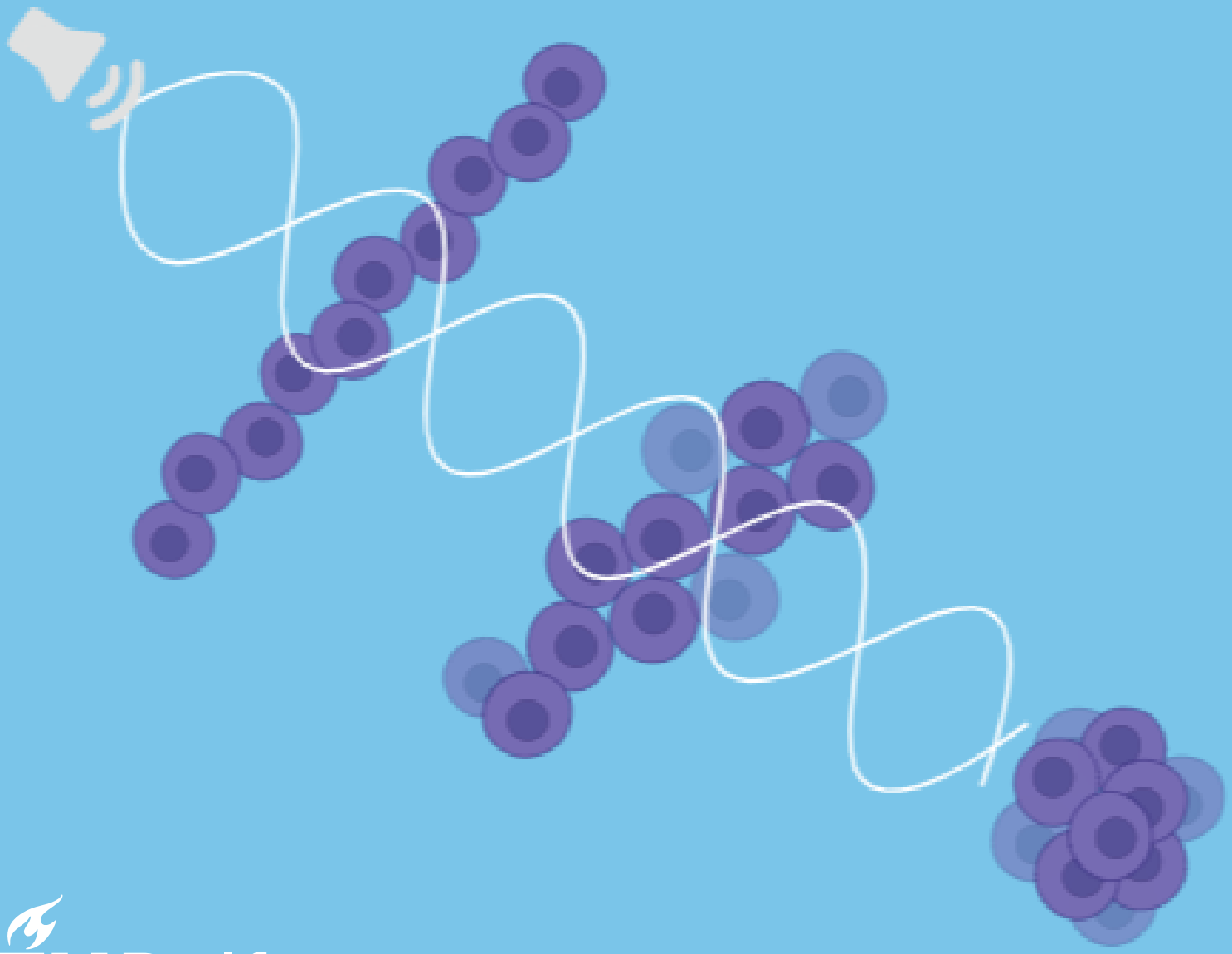

Delft University of Technology

TU Delft

Acoustofluidic Levitation in Organoid Cultures

Tuning Ultrasound to Cluster Cells

by

Pradnya Gharpure

to obtain the degree of Master of Science
at the Delft University of Technology,
to be defended publicly on Friday 30th August 2024 at 9:30 AM.

Student Name	Student Number
Pradnya Gharpure	5763681

BM51035:	BME MSc Thesis
Master Programme:	Biomedical Engineering
Committee Chair, Supervisor :	Dr. Massimo Mastrangeli
Supervisor :	Dr. Sabina Caneva
Daily Supervisor :	Ir. Hande Nur Açıkgöz
Thesis Committee :	Dr. Tiago Lopes Marta da Costa
Thesis Committee :	Dr. Sophinese Iskander-Rizk

An electronic version of this thesis is available at http://repository.tudelft.nl/

TU Delft

Acknowledgements

”*The explorative journey of research is made worthwhile as much as by the co-adventurers, as much as by the splendor of science*!”

The positive power of good collaborations has been my greatest takeaway experience from this MSc endeavor which comes to a close today. This thesis project depicts the culmination of my graduate journey at TU Delft and the realization of a long-sought dream of contributing to the exciting domain of bio-microtechnologies. As I wrap up this final milestone in my journey at TU Delft, I firstly thank my parents for being the subtlest yet strongest support, and for believing in me while they taught me to be brave enough to believe in myself on this interdisciplinary path of research I took up in Delft.

I am extremely thankful to my supervisors Dr. Massimo Mastrangeli and Dr. Sabina Caneva for encouraging me to take up my collaborative project idea, the first between the two groups, and guiding me through the wind roads and hurdles to bring it to fruition. Their feedback and advice at each juncture in the project have enabled me to develop a critical scientific attitude towards my work which is a lifelong learning for me. I would like to thank my daily supervisor Hande Nur Açıkgöz for always being available for coffee-table discussions on even the minutest of aspects, be it experiments or computations. I am also grateful to Dr. Jean-Philippe Frimat from the Leiden University Medical Centre (LUMC) for providing an insightful biological viewpoint on my research objective and the discussion on the broader impact and feasibility aspects of the same. Setting up a multi-group collaboration can be a daunting task, however, I was fortunate to find wonderful friends in fellow researchers both in PME and ECTM, who always gave an eager ear when I wished to discuss research, and also pitched in and helped when needed. The group discussions and meetings with each of the groups added a lot of value to my project and boosted my morale as a budding researcher from time to time.

I am thankful to Dr. Tiago Costa and Dr. Sophinese Iskander-Rizk for taking the time to assess my work as my external committee. I am very thankful to the PME and ECTM lab support for their cooperation throughout my time at the labs. Experimental work can be challenging and sometimes one seems to hit blank walls, however, I am thankful to each person who came by me in the labs and offered advice and help. Lastly, I have been fortunate to find like-minded friends in Delft even as an introvert, and they always kept me going when I was melancholy, be it with joyful birding walks or merry musical talks.

The robust and tenacious faith of my parents, the persevering support and guidance of my supervisors, and the warmth of my close friends and fellow researchers have molded me into the person I am today, who can dare to dream of embarking on more challenging research endeavors in the future! Each of them will always possess a very special place in my academic diary!

Pradnya Gharpure
Delft, October 2024

Abstract

In-vitro 3D organoid cultures constitute an essential component of modern-day biological research, with key application areas in drug and therapy testing, and Organ-on-a-Chip models. The increasing demand for reliable models comes with the challenge of boosting the throughput of production of these cultures. The currently researched 3D culture methods pose the challenge of not being contact-free, of limited versatility and throughput in organoid culturing, and often lack a stimulus to promote cell agglomeration. This work presents acoustofluidics as a stimulus-driven solution to promote the clustering of cells in a levitated, suspended environment. In order to establish this objective experimentally, an SBAW resonator was designed, fabricated, and tested as a PoC (Proof-of-Concept). The experiments were carried out with the fabricated PoC which was characterized to assess the trapping performance and determine the controllable experimental variables to tune the acoustofluidic effects aptly, leading to the formation of stable clusters in SBAW nodal planes. On successful fabrication, the device showed repeatable trapping over a wide bandwidth of 300 kHz, and trap stiffnesses of up to 1.7 fN/μm determined experimentally based on the processing of particle agglomerate imaging. It was observed that the trap stiffness was adequate for levitation over several hours, and yet allowed for the formation of a 3D agglomerate of particles. It was also shown that a frequency-sweep actuation was successful in overcoming fabrication limitations and suppressing streaming, and a suitable working range of experimental parameters could be determined to achieve initial clustering in under 3 minutes. A futuristic outlook on the in-plane particle confinement methods to further improve the target performance, and considerations for biological experiments as the immediate next step have been presented as a concluding note in this thesis. This work thus paves the way for the integration of this technique into laboratory organoid culture formats. This positively complements the objective of cutting down the agglomeration time for initial organoid clustering, for an anticipated positive impact on the production throughput and developmental aspects of organoid cultures, with the *in-house fabricated and characterized PoC* presented in this work as an *enabler*.

Keywords: BAW resonators, 3D Organoid Cultures, Acoustic Trapping, Primary Radiation Force, Resonant Cavity, Contact-free Clustering.

Contents

List of Figures

Nomenclature

Abbreviations

Abbreviation	Definition
2PP	Two Photon Polymerization
ARF	Acoustic Radiation Force
BAW	Bulk Acoustic Wave
DoF	Degree of Freedom
DRIE	Deep Reactive Ion Etching
ECM	Extra Cellular Matrix
FEM	Finite Element Method
FFT	Fast Fourier Transform
FZP	Fresnel Zone Plate
IDT	Inter-Digitated Transducer
IPA	Isopropyl Alcohol
LDV	Laser Doppler Vibrometry
PDMS	Poly-Dimethyl-Siloxane
PoC	Proof-of-Concept
PRF	Primary Radiation Force
PZT	Piezoelectric Transducer
SAW	Surface Acoustic Wave
SBAW	Standing Bulk Acoustic Wave
SRF	Secondary Radiation Force
WLI	White Light Interferometry

Symbols

Symbol	Definition	Unit
f	Drive Frequency of Piezoelectric Transducer	[Hz]
ρ_0	Density of Fluid/Medium	[kg/m^3]
ρ_p	Density of Particles	[kg/m^3]
β_0	Compressibility of Fluid	[Pa^{-1}]
β_p	Bulk Modulus of Particle	[Pa^{-1}]
v	Acoustic Velocity	[m/s]
v_p	Particle Velocity	[m/s]
η	Dynamic Viscosity	[Pa.s]
ϕ	Acoustic Contrast Factor	-
p	Acoustic Pressure	[Pa]

Symbol	Definition	Unit
p_1	First-order Pressure	[Pa]
p_2	Second-order Pressure	[Pa]
p_a	Pressure Amplitude	[Pa]
λ	Acoustic Wavelength	[m]
λ_d	Laser Wavelength	[m]
f_D	Doppler Frequency Shift	[Hz]
a	Particle Diameter	[m]
F_{rad}	Acoustic Radiation Force	[N]
F_{drag}	Drag Force	[N]
E_{ac}	Acoustic Energy Density	[J/m^3]
k	Wave Number	[m^{-1}]
T	Absolute Temperature	[K]
k_B	Boltzmann Constant	[J/K]
k_a	Acoustic Trap Stiffness	[pN/μm]
γ	Normalized cross-correlation coefficient	-
d	Interparticle Distance	[m]
$Z_{acoustic}$	Acoustic Impedance	[MRayl]
V	Voltage	[V]

1 Introduction

1.1. Background

The increasing need for personalized medicine, therapies, and the associated biological research as well as the necessity for drug modeling with growing cases of degenerative diseases have led to the demand for more representative in-vitro models in recent times. In-vitro organ models are laboratory culture models, wherein pluripotent stem cells or embryonic cells are cultured in controlled and sophisticated environments with ambient controls as well as stimulation approaches to create organ-like 3D structures on maturation. The resulting 'organoids' are then utilized for various research directions such as testing responses to electrical stimulation or assessing the efficacy of a certain drug.

A wide range of cell culture techniques has been developed over the last century, starting from the first cell cultures [1] in the early 1900s to modern-day systems such as Integrated functional Multi-Well Plates [2]. However, they present potential scope for exploration and added bio-technical functionalities to enhance the overall performance of the techniques. This work presents acoustofluidics as an exciting research avenue for improving the throughput and developmental aspects of 3D organoid model cultures.

1.2. Synergy of the Fields

Acoustofluidics, signifying the manipulation of particles in microfluidics with acoustic waves, is a new paradigm in biomedical applications. This technique has been used extensively at micron and sub-micron scale for applications such as patterning and transport of entities [3, 4, 5, 6, 7]. There is, however, scope for exploration to extrapolate the technique to handle and localize sub-mm size objects which points perfectly to the organoid lengthscale regime. Furthermore, a key aspect of interest also lies in assessing the impact of acoustic forces as a mechanical stimulus in organoid culture research. This work bridges this gap between acoustofluidics and organoid cultures by presenting a synergy of the two fields as depicted in Figure 1.1.

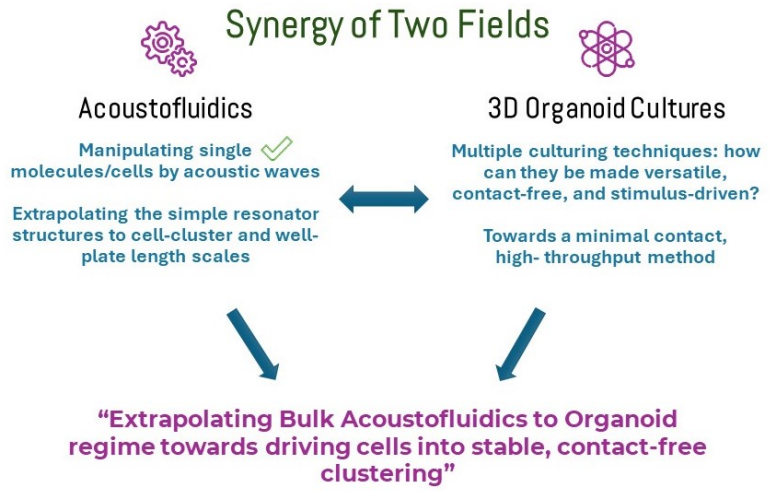

Figure 1.1: Acoustofluidics and Organoid Cultures : The Synergy.

This thesis discusses the demonstration of the above-envisioned synergy through a combined two-way computational-experimental approach (via a fabricated Proof-of-Concept) to employ Bulk Acoustofluidic Resonators to drive particle clustering. This paves the way for the development of integrable acoustofluidic systems with potential avenues in organoid culture research. The work concludes by outlining the suitable parameters and actuation techniques within the scope of the project to achieve the required function and presents a futuristic outlook on the additions and improvements to take the system suitability even closer to the intended point-of-use.

1.3. Outline of Thesis

To set the context of the methods and techniques adopted in this work and define the project goals, a concise review of the state-of-the-art, both from the biological and technical viewpoints is presented first. The qualitative research objective is presented herein by highlighting the missing links from the literature review. This is then succeeded by an analytical overview of the governing physics involved in acoustofluidics, the underlying mathematics, and physical (sub)phenomena that result, with a concluding note on the relevance and applicability of the discussed physical phenomena to the research objective under consideration. As a summary, the research objective is quantified, linking the qualitative picture presented previously to the target functional values in this work.

Next, the design, fabrication, computational, as well as characterization methods used as a part of this work are explained in detail with suitable depictions and linkages to put forth a holistic methodical picture. This is followed by an extensive description of the results of computational studies, fabrication, chip characterization, and trapping experiments. These results are discussed and linked for traceability to the objectives put forth in the previous chapters, and to outline the suitable operating conditions to fulfill the same within the scope of this project. Finally, a concluding note is presented to highlight the linkage of this work to the bigger application-oriented picture, followed by a futuristic outlook into the possible improvements in the system.

2

Review of State-of-the-Art

2.1. In-Vitro Organ Models: The Concept

An in-vitro organ model refers to a group of methods by which an organ is represented outside a living organism (in-vitro), typically in miniaturized devices. Preliminary in-vitro models began from 'cell-cultures', the simplest representations consisting of a 2D cell layer cultivated under body-like chemical and ambient conditions [8]. The very first cell cultures were experimented with in the early 20th century, wherein cell monolayers originating from embryonic or pluripotent stem cells were cultivated on adherent cell culture plates, and conditions such as temperature, humidity, and gas exposure were controlled [1]. The objective of the technique has been to create a close replica of the in-vivo tissue structure and microenvironment of the tissue, ex-vivo. This led to the group of in-vitro devices and technologies called 'Organ Models'. The relevance of such models is the possibility of reduction, and, in the long term, the possible elimination of human and animal trials in drug discovery and in the development of therapies such as neuromodulation, deep-brain stimulation, and similar applications.

Though the advent of the concept of an ambient-controlled 2D culture plate was a significant step in itself, it did not represent the in-vivo tissue structures to a satisfactory extent. The major shortcoming herein was the fact that a 2D model performs quite differently in terms of the maturation and development of the cells of the cluster/agglomerate, as well as in terms of the cell-cell interactions as compared to in-vivo conditions. This emphasized the necessity of systems to culture better 3D mimics of the target tissues/organs in-vitro [9]. Some of these comparative aspects are depicted in Figure 2.1.

2.2. Paradigm Shift from 2D to 3D models

The shift from 2D to 3D organ models and cultures can be attributed to multiple biological aspects wherein the 3D models perform better as organ mimics. Firstly, structurally, the body tissues and organs assemble into complex 3D structures and then mature physiologically and morphologically into organs. When cells adhere to a surface such as a culture plate, they spread out over the surface and cannot maintain and replicate the natural cell shape. Instead, they grow into networked sheets as they can spread only in two directions. A heterogeneous, or multilayered tissue construct formation is therefore not possible. On the other hand, 3D cultures enable a 3-dimensional form of agglomeration, in which the cells differentiate while maintaining shapes closer to in-vivo morphology, and also depict cell-cell interactions similar to those seen in-vivo [9]. In terms of drug and stimulation therapy trials,

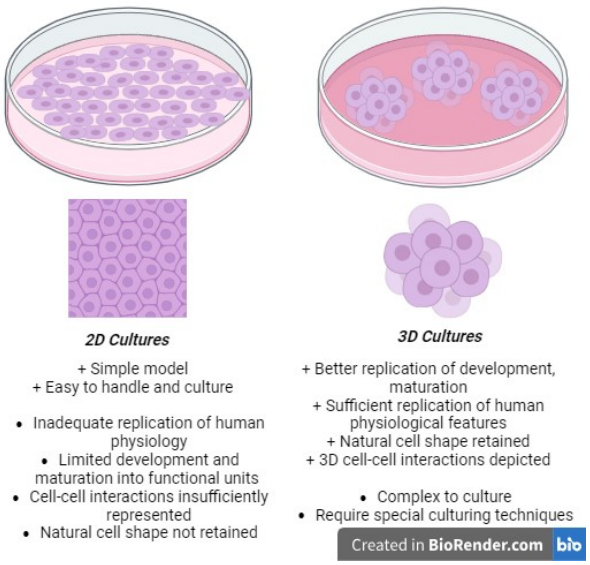

Figure 2.1: Comparative Features of 2D and 3D In-Vitro Models.

the 3D models produce more analogic (correspond-able) results to human and animal trials, and can eliminate the false positives or negatives that might be brought in by 2D culture results [9]. Thus, there was a research-driven paradigm shift from 2D to 3D culture models in the first decade of the 21st century [10], which was enabled by the rapid advancement in microfabrication and additive manufacturing technologies with scales and precision matching with the target culture entities.

Two typical biological working units of a 3D in-vitro organ model are spheroids and organoids (depicted in Figure 2.2). The terms are often used in similar contexts, however, they signify different properties in terms of the models they represent. Spheroids, as the name suggests, are spherical agglomerates primarily used as tumor models, and thus are derived from cancer cell lines. They are primarily used in cancer drug testing, which is of key importance in modern oncology. On the other hand, organoids are derived from embryonic or pluripotent stem cells, which are in the early stage of development and, with time, mature into highly functional replicas of organs in the microenvironment provided to them. Just as cells are the basic unit of life, organoids can be considered to be the basic functional units of a living organ. In principle, organoids differ greatly from spheroids given that they depict physiological functions, gene expression, morphology, and intercellular interactions similar to an organ itself, thus reaching high levels of complexity compared to simply an agglomerate of cells (i.e. spheroids) [11, 12]. To facilitate the cultivation of such 3D cellular structures, there have been multiple methods and technological models developed, the principles of which have been discussed in the next section.

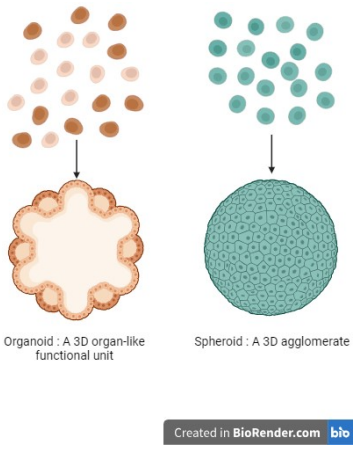

Figure 2.2: Spheroids and Organoids: Comparative Features.

2.3. State-of-the-Art Methods and Models

Cells require a suitable microenvironment to thrive, differentiate, proliferate, and assemble into 3D structures. The generation of such environments has been facilitated by microfabrication techniques that scale down to the length scales of cells and organoids (ranging from a few microns for cells to a millimeter for organoids). Various system models have been developed depending on the type of cell culture intended and the intricacies involved. This section describes the prominently used culturing techniques, as well as their advantages and limitations with respect to the target applications.

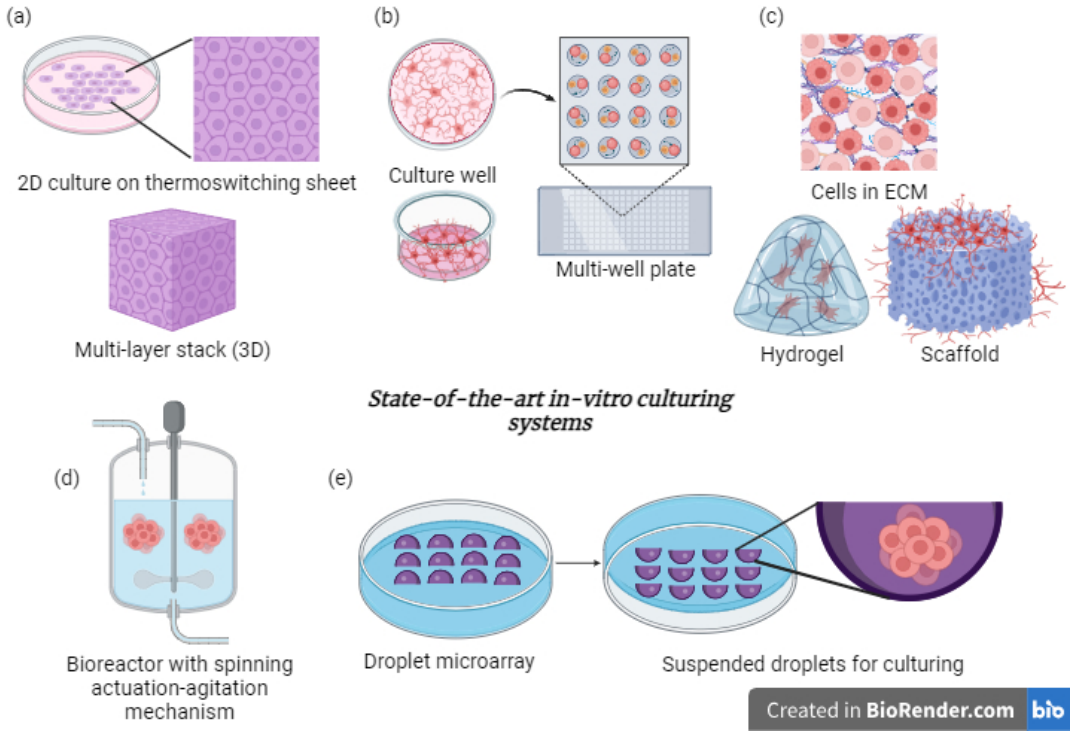

Figure 2.3: Pictorial depiction of the in-vitro culture techniques described in this section: (a) Cell sheets, (b) Culture plates and well plates, (c) ECM-based techniques, (d) Bioreactors, (e) Suspended droplet cultures.

2.3.1. Culture Well Plates

Cell culture plates were the first baseline environments in which in-vitro culturing took place. Given the need for multiplexing and parallel experiments, single culture wells were gradually scaled up into multi-well plates [1]. Building on the basic designs, there have been several advancements in the technology in terms of flexibility, added features such as integrated temperature control, fluidic arrangements, as well as surface functionalization of the well-plate for a particular cell-type dependent target function [13, 14]. Cell culture research has revolved around culture plates for quite a while, and in particular, surface functionalization has been the primary focus for obtaining the desired environment according to the cell type. This includes designing the inner surface of the wells such that they interact as needed with the cell cluster, for example, coatings where the adherence of the cells to the surface is minimized, or an added gel-like layer to mimic the soft tissue properties. Though the system is simple in preparation and handling, it faces some challenges with the rapidly advancing demands from 3D cultures. Firstly, the functionalized plates rely heavily on cell-material interactions and biochemistry to yield well-functioning models. This prevents them from being versatile or 'non-specific' methods (in essence, they depend on biochemical interactions and specificity). Instead, the culture plates are often specific to cell types and properties. Though non-adherent culture plates are being explored for other cell types, they often cannot produce a 'suspended' organoid. A suspended culture is a better alternative for culturing, particularly than adherent cultures on rigid surfaces, as organoid maturation on rigid surfaces does not represent the in-vivo conditions well. Certain cell types such as embryonic, or region-specific neuronal cells also develop in a minimal contact environment in-vivo, which means that a suspended culture is a better model for their maturation [15, 16]. Thirdly, there are very limited instances where an actuation or agitation mechanism is used to promote agglomeration. Without such an external stimulus, the yield of 3D organoids that can be cultured is low. Without a driving mechanism, typical self-assembly timelines can range from a few days to weeks, followed by up to months for complete development and maturation of the organoid [15]. Magnetic-actuation-enabled well-plates have appeared as commercialized products lately for driving cells into a suspended agglomeration, however, they can pose challenges of complexity in setup, miniaturization limitations and lack of biocompatibility emerging from toxicity of the magnetic nanoparticles that are part of the system [17].

2.3.2. Hydrogel, Scaffold and ECM-based techniques

The simplicity of well-plates and the wide range of commercialized products developed do not outweigh the fact that most plate surfaces are not the best in-vivo mimics for growing cells. This is primarily because the mechanical properties of the plate materials differ significantly from those in-vivo. Hydrogels and scaffolds are tools for cell seeding which more closely resemble the cell ECM (Extra-Cellular Matrix) in terms of elasticity and biocompatibility [18]. Hydrogels are cross-linked polymeric networks which possess biocompatible properties and also the ability to store fluid, similar to the ECM [19, 20]. Closely related elements are scaffolds, which act as a porous template that aids the seeding and proliferation of cells into 3D structures. They are capable of providing channels for vascularization and stable mechanical structures for cell growth [21]. Both these systems have been successfully used in 3D cell cultures and also possess flexibility, ease of handling, and the possibility of integration with microfluidic setups [22]. However, three aspects are still missing in this context. Firstly, the techniques lack reproducibility in the properties of the produced hydrogels and scaffolds, and thus, there is batch-to-batch variation in the subsequent biological outcomes [23]. Secondly, the methods rely on the specific interactions of cells with the synthetic ECM, which once more, brings in specificity. This ensures that the ECM suits the cell-type, but in turn, the method lacks versatility as it cannot act as a template for multiple organoid types. Thirdly, the lack of integration with stimulation/actuation techniques for cell assembly once again limits the throughput of the cultured organoids.

2.3.3. Bioreactors

Bioreactors are all-in-one integrated culturing systems in which culture media, ambient control, fluid flow, actuation, sensing and at times imaging are carried out in a single unit. The technique has gained prominence due to its success in culturing of spheroids and organoids, particularly those derived from neuronal progenitors [17]. Organoids cultured in reactors can be agitated, stirred with the help of fluidic manipulation (similar to spinner flasks with a simple rotation function), and rotated to form spheroids [24]. The system also offers scope for automation and high throughput in terms of agglomerate formation and development. The complex system can also accommodate mechanical stimulation for cells using add-on systems such as electrically-actuated membranes and shear stresses resulting from laminar flow [25, 26]. However, the inherent complexity of the system makes it challenging to scale up due to the numerous components and modules involved in such a system. Miniaturization is also another challenge. Microfluidic chips with complex and versatile flow management are a step towards miniaturized bioreactors [27], and the miniaturization is being aided to some extent by high-precision additive manufacturing and microfabrication [28].

2.3.4. Cell Sheets

Cell sheets are essentially 2D surface-functionalized temperature or chemically-reactive polymer entities that are a new development in culture studies. In essence, they are sheets with a thermoswitching, or a chemical or photoresponsive function. Cells proliferate and grow on the surface with their ECM, followed by detachment from the surface after a temperature/pH switch [29]. This process produces basic monolayers, which subsequently form multilayers by successive growth and stacking cycles [30]. Due to the nature of the process that preserves the ECM and the sheet together, they have not only been successful as organ models, but also as regenerated tissue-culture systems for in-vivo transplant sources [31, 32]. The high biocompatibility of the technique is key in terms of its advantages; however, there is a specificity aspect and temperature dependence involved in the processes too, which limits versatility, and compatibility with desired cell ambient conditions[33]. To date, there is also little reported on the integration of the technique with physical cell agglomeration acceleration methods (instead of reliance on sheet-wise self-assembly), which limits the throughput of this process.

2.3.5. Suspended Droplet-based Cultures

The concept of hanging droplet-based culturing stems from the necessity of a biomimetic surface for the self-assembly-driven cell growth and culture. The arrangement of the culture system such that the organoids self-assemble into 3D structures by gravity in a droplet (instead of a rigid 2D surface) makes the system more physiologically relevant for organoid development. The possibility of sustained production of microscale droplets [34] and integration with well-plate platforms [35], and with paper-based microfluidics [36] is an added advantage. This technique relies on surface tension at the microscale to hold the droplet hanging in place, which makes system design crucial to its performance, for example, an insufficient stabilizing agent (surfactant) can hamper the system performance due to an inability to produce sustained droplet for longer culturing periods. Recently, microfabrication technologies have enabled the formation of robust droplet platforms through surface-patterned microdroplet arrays [37]. The method has been demonstrated to successfully culture spheroids for various in-vitro tumor models [38, 39]. However, hanging droplet systems rely on precise manipulation of surface tension and droplet stabilization (importantly, preventing evaporation), which limits commercialization, and makes integration with standard platforms a challenge.

2.4. Challenges in Current Methods

Organoids, in-vitro organ representatives, are crucial to the performance of complex in-vitro models, and they often constitute the key biomimetic features of the model. Various techniques are being researched for the culturing of these organoids, which have been outlined with their intricacies in the previous sections. Based on the concept of the maturation and development of an organoid from its progenitor stem cell, it is evident that the environment in which the cells are cultured plays a crucial role in the physiological, morphological changes, and in the expression of genes and protein markers the cell agglomerates show as they mature into organoids [40]. In 3D culture, cells adaptively mature and respond to the materials they are cultured in depending on their mechanical and chemical properties. Just as the culture medium (fluid) is crucial to their development, the surfaces they are in contact with also affect their maturation greatly. Cells mature depending on the environmental mechanical stimuli they are subjected to, similar to Wolff's law [41]; for example, rigid surfaces such as glass plates do not mimic the 'elastic' in-vivo environment, which is why the cells tend to lose their natural shape and properties in such an environment. To overcome this challenge, especially for cell types that benefit from a suspended culture such as hematopoietic, epithelial, and certain neuronal cells, surface functionalization (tuning the system such that the cell-cell forces are greater than the cell-surface forces) has been the primary solution for non-adherence [17]. However, this brings in specificity, and the technique is quite time-consuming as well. This calls for other solutions for suspended culturing for better bioenvironment depiction. Spinner flasks and reactors have been a common solution herein, however, the flow rate of the agitating mechanism is very crucial, as a low rate would cause settling, and a high rate would cause undesired high shear force on the cultured organoids [17]. Magnetic levitation, as an alternative, also has limitations due to the biocompatibility of the nanoparticles used in such a levitating system [17].

The second parameter of focus here is the cell agglomeration. Organoid cultures typically have coarsely two phases. Firstly, the one in which the cells form a primitive (early in the stage of development) agglomerate and show basic signs of development and agglomeration. The second step consists of the clusters then being seeded in a vascularized, appropriate chemical environment wherein they are provided with the required nutrients, gases, and are monitored until complete maturation. Each of these steps typically takes several weeks by conventional culture techniques. The formation of cell agglomerates is often completely reliant on self-assembly (no accelerating mechanism is present), which affects the throughput of such a system significantly. A lack of precise control over the organization of cells in an organoid also negatively affects their development and the repeatability and uniformity of the process [42]. Especially in applications such as the production of heterogeneous brain organoids, wherein specific assembly of cells is required, patterning methods for cells would be of great utility [43]. Without a driving mechanism for aggregation, the construction of dense tissue structures is often challenging and time-consuming [44]. Maturation of the constructs into a viable and developed organoid thus relies heavily on the initial assembly of the cells in the culture. Magnetic techniques and dielectrophoresis have been used particularly for this application, but raise questions about cell viability in a nanoparticle environment [17], and in high strength focus regions of non-uniform electric fields [45]. Figure 2.4 depicts the comparative challenging aspects of the techniques discussed in the previous sections.

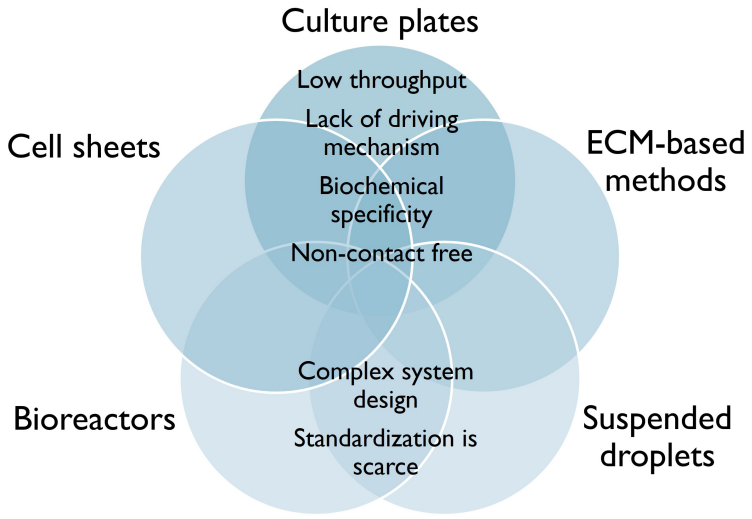

Figure 2.4: The Challenging Aspects of State-of-the-Art Culture Methods.

In essence, there is a need for a *reproducible technique* that can *accelerate the formation of initial cell agglomerates* (increase the throughput), facilitate their agglomeration, and also levitate/suspend the agglomerates in a sustained manner until their basic maturation, mimicking low-contact in-vivo conditions. This is particularly essential in view of the constantly increasing demand for in-vitro model systems with drug and therapy research growing rapidly. Simplicity in design and the possibility of integration with existing culturing techniques would be an added practical advantage.

2.5. Acoustofluidics in Biological Research

2.5.1. State-of-the-Art Biomedical Applications: Critical Review

Due to their biocompatible, contact-free, and integrable nature, acoustic techniques have found great utility in biological research applications. The use cases range from acoustic tweezers to manipulate single molecules [46, 47, 5], to larger scale applications such as cell seeding in hydrogel media [48]. Figure 2.5 depicts the typical time and length scales across which entity manipulations can be carried out by acoustic waves in biological application scenarios.

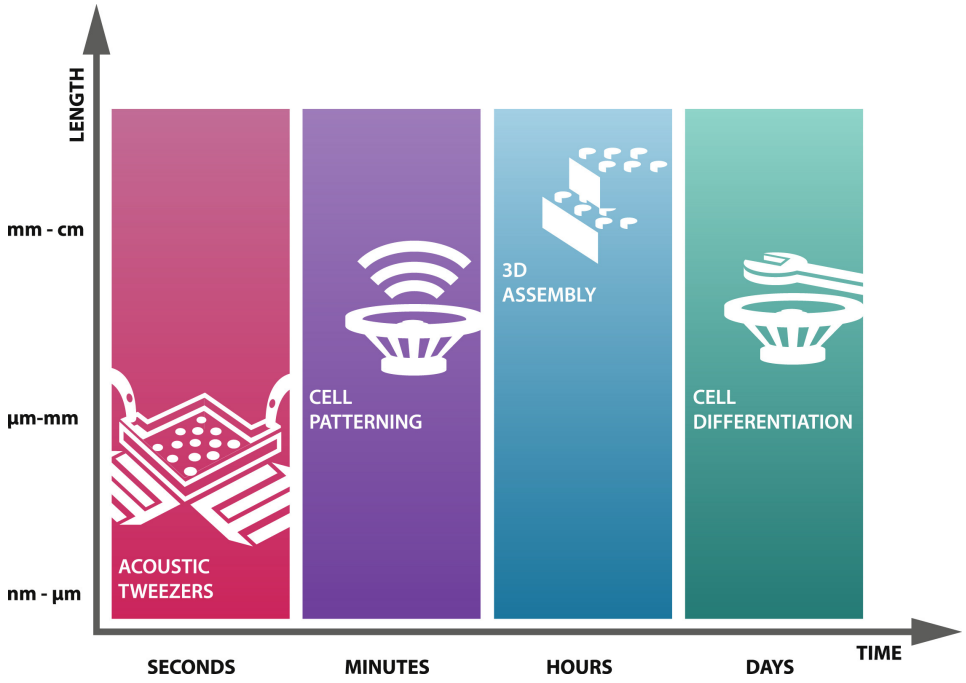

Figure 2.5: The typical time and length scales for biological applications of acoustofluidic devices, from [49].

Living cells in a microfluidic setup can be manipulated similar to particles in a microflow. Cells possess their own set of biological as well as mechanical properties. Mechanical characterization of the cell parameters (called cell mechanotyping) is of prime interest in understanding the mechanics of single cells which is an interesting application area in in-vitro organ model research [50]. For particles with a positive acoustic contrast, trapping occurs at the pressure nodes of a standing wave. Living cells typically exhibit a positive acoustic contrast, and the factor switches signs from positive to negative on cell death [51]. This simple fact regarding living cells has been used to sense cell death and study cell viability in a novel manner. The compressibility of tumor cells is an important parameter in differentiating cancerous cells from normal cells. Acoustic techniques possess the ability to separate entities based on differences in compressibility, and such a separation has been demonstrated using BAW waves in the cited work [52]. Acoustic streaming has also been used effectively to manipulate and pattern biological entities [53].

The target application of interest, and a widely evident application of acoustic wave techniques has, however, been the precise localization and trapping of particles. Standing wave modes are simple to set up and effective to work with for this application, and thus have been at the center of the trapping device technologies [54]. Acoustofluidic devices have been developed for versatile and tuneable applications to manipulate particles in fluidic suspensions by SAW wave devices using chirped IDTs [55]. Microfluidic cell patterning and spheroid generation have been promisingly demonstrated by SAW acoustofluidic methods [56]. Once localized, the cells can be allowed to proliferate into agglomerations, and it has been observed that the proliferation is not affected by the acoustic waves, and the cells proliferate based on their biological properties (depending on their original cell type). The agglomerate sizes can be controlled, though, by the concentration of cells in the system, which in turn governs the concentrations trapped at the acoustic nodes [57].

A cell culture dish was actuated with an ultrasound transducer to form trapping nodes for cell trapping [58]. On the other hand, well-free culturing of cells with SAW Lamb waves generated by focused IDTs has been demonstrated in a recent work [59]. Flexural plate waves, which propagate in a direction perpendicular to actuation usually observed in thin plates were utilized to pattern cells close to the surface of a culture plate [60]. Mesenchymal stem cell spheroids were assembled into multiple disk-like structures in a bulk wave device by acoustic levitation, and maintained in suspended form for up to 24 hours, during which they self-assembled into 3D forms from the initially formed sheets [61]. A

similar approach of self-assembly of trapped 2D cell sheets into spheroids was demonstrated in another work [62]. However, there is still a reliance on self-assembly for the formation of a 3D structure from a 2D sheet. This presents a scope to look into approaches to construct 3D structures acoustically.

Multicellular heterogenous spheroids were fabricated by SAW waves on a chip, with a high throughput and microstreaming for levitation of the spheroids [63]. A similar approach for 3D manipulation of cells using acoustic streaming for levitation with SAWs was demonstrated in [64]. Scaffold-free generation of heterotypic spheroids was carried out with SAW waves using gravity, in a non-contact-free way [57].

A SAW wave device for constructing long fiber-like tissue structures in a hydrogel medium [65], or SAW-based sorting of cells in a hydrogel [66] are applications that combine ECM-based techniques with acoustics. High throughput manufacturing of 3D spheroids in uncured hydrogels, followed by curing of the medium for further maturation was reported with a 3-orthogonal-transducer standing BAW device [48]. Cell patterning for complex patterns was also successfully demonstrated in hydrogels with 3D printed holograms [67]. Each of these techniques, however, calls for integration of the acoustic trapping with the hydrogel medium.

BAW and SAW devices have their own set of characteristics with respect to their suitability in organoid culture context. In simple terms, BAW devices can typically manipulate larger particles and aggregates even at a lower frequency (longer wavelength, as the Rayleigh criterion then holds for larger particles too - explained in Chapter 3), and are comparatively simpler to prototype [68, 69]. There have also been instances of single droplet handling by BAW microfluidics, with transversal 2-way trapping in standing waves [70]. The nature of BAW devices makes them versatile in design and setup as well. Concepts such as concave trapping surfaces can be implemented in a bulk device for a focused trapping spot [71].

The application areas focused on in this section depict the suitability of acoustic techniques to biological entity manipulation scenarios, and the versatility in their application, with respect to the possibility of manipulating a range of sizes and entities with varying biochemical nature. However, there are certain unexplored application links and interesting technological aspects, which have been outlined in the subsequent section.

2.5.2. The Missing Link

Acoustofluidics has been the method of choice for a large number of biological applications as discussed in the previous sections. The research in this domain demonstrates, however, a larger focus on SAW devices for the manipulation of single particles. In terms of BAW devices, the focus of applications in tissue engineering and organ models has been primarily the production of spheroids (simple agglomerates), rather than developmental organoids. However, an increased throughput in spheroid development without a compromise in cell viability demonstrates the possibility of extrapolating the concept to organoid development studies.

In terms of the biological findings, little has been documented concerning the impact of *acoustically-driven agglomeration* on the *throughput* of the primitive (early stage) organoid clusters, and this, thus, demonstrates the scope for a research direction. Findings regarding the *development and maturation* of the pluripotent cell clusters into organoids in terms of their response to the levitated, mechanically (in particular, acoustically) stimulated conditions of culturing have been scarce to find in the works presented. This opens up the path to investigating the impact of acoustic manipulation in the field of organoid development as a long-term research goal.

In terms of acoustic device technologies, controlling of 3D structures with 2D wave device designs is still a challenge to be explored [72]. Focusing of particles into *localized*, *suspended (contact-free)*

clusters without losing *optical access* for microscopy and with *minimal complexity in device setup* is still an underexplored domain, and opens up multiple technology exploration opportunities, which have been looked into in the project.

2.6. Defining the Research Objective

Based on the background presented by the review of state-of-the-art, the research objective is proposed as *"Employing BAW resonator PoCs (befitting organoid culture applications in the length-scale regime and material selection) to enhance the formation of sub millimeter-sized trapped particles into stable 3D clusters, towards demonstrating stimulus-driven, contact-free, high-throughput organoid culture avenues."* A representative depiction of this objective is presented in the Figure 2.6.

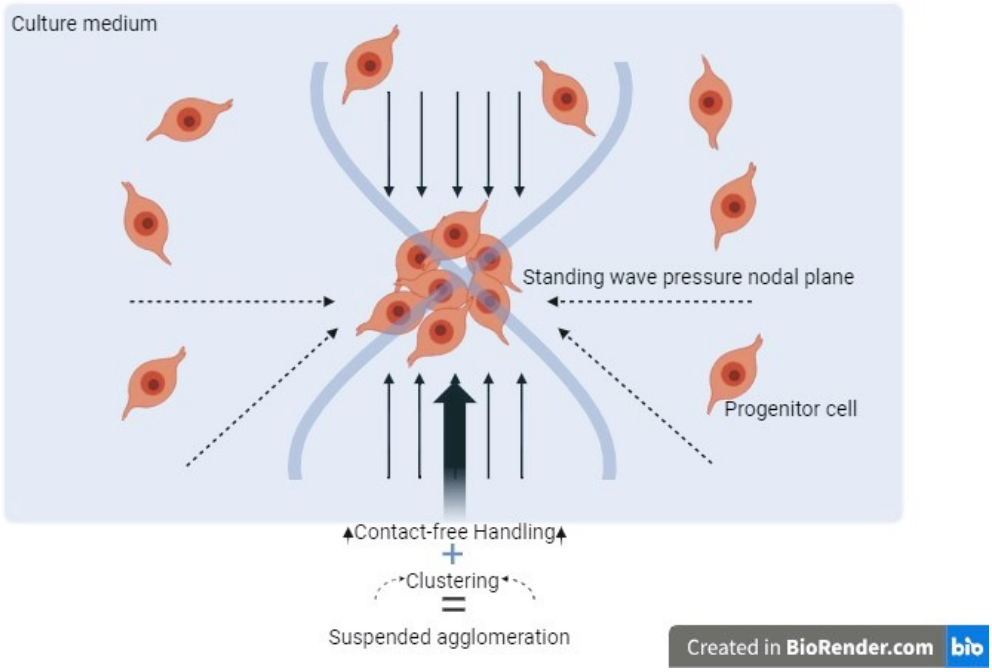

Figure 2.6: The Research Objective, pictorially.

This objective shall be targeted via the below sub-objectives:

- Development (analytical, computational design and fabrication) of a bulk acoustic wave device compatible (in setup, and in functionality) with in-vitro organoid cultures.
- Assessing experimental parameter optima and tuning the associated phenomena to achieve levitated nodal plane clustering of particles into early-stage organoid-like agglomerates.
- Characterizing the fabricated device, demonstrating the target functionality, and proposing the roadmap for the intended point-of-use.

3

Acoustofluidics: Setting the Context

3.1. Introduction

Building on the research gaps and avenues presented by organoid research described in the previous chapter and the introduction to acoustofluidics as a proposed solution pathway to address the current challenges, this chapter presents the outline of the fundamental physical concepts in acoustofluidics briefly with their relevance to the application under consideration.

Acoustofluidics, the confluence of acoustics and microfluidics, is a niche domain of research that paves avenues into contact-free, versatile manipulation of micro-scale entities in fluids, with minimal reliance on the chemical/surface interaction properties of the particles. The technique is finding relevance and application in many biological points-of-use in recent times as the lengthscales of biological entities, right from single molecules/DNA to cells and eventually organoids matches with the range of particle sizes that can be manipulated by acoustic waves in microsystems. In order to set the context of how this manipulation works, an analytical viewpoint is presented in this chapter. The analysis is based on the perturbation methods towards finding the solutions to the governing equations for fluid pressure and velocity fields (namely, the Navier-Stokes equations), and the acoustic wave is treated as a harmonic perturbation in the pressure (p), velocity (v) and the density (ρ) of the fluid medium of propagation.

3.2. Governing Equations

The Continuity Equation (3.1) and Navier-Stokes Equation (3.2) are the analytical starting points for evaluating the pressure field resulting from the acoustic wave propagation in the fluid. The propagation of the acoustic wave leads to Equation 3.3, depicting the pressure as a function of density ρ_0. The acoustic field solution lies in the solution of these three coupled non-linear, partial differential equations.

$$\frac{\delta \rho_0}{\delta t} + \nabla.(\rho_0 v) = 0 \tag{3.1}$$

$$\frac{\rho_0 \delta v}{\delta t} + \rho_0 (v.\nabla v)v = -\nabla p + \eta \nabla^2 v + \beta \eta \nabla(\nabla.v) \tag{3.2}$$

$$p = p(\rho_0) \tag{3.3}$$

where,
v is the velocity field

ρ_0 is the density of the fluid
∇ is the gradient operator
p is the pressure field
η is the dynamic viscosity
β is the compressibility
$F_{external}$ is the external body (volume) force vector

The above constitute the governing equations to derive the pressure fields under acoustic wave propagation. The analytical solution being challenging, the equations are best solved by perturbation methods, up to the second term [73]. This can be done by treating the pressure, velocity, and density perturbations resulting from the acoustic wave as perturbations up to the second order.

Assuming the fluid, before the acoustic wave propagation, has a constant density ρ_0 and pressure p_0, the perturbation caused by the acoustic wave is estimated by the solutions considered up to the second-order terms of form:

$$\begin{aligned} p &= p_0 + p_1 + p_2 \\ \rho &= \rho_0 + \rho_1 + \rho_2 \\ v &= 0 + v_1 + v_2 \end{aligned} \tag{3.4}$$

The first-order terms, in principle, dominate the second-order terms in magnitude greatly, however, in a time-averaged sense, the first-order terms would yield a zero value for harmonic perturbation, whereas the second-order terms which consist of products of first-order harmonic terms would yield a non-zero value. This is the origin of the acoustic effects that have been described and studied in this thesis. Herein, the time-averaged second-order pressure $< p_2 >$ is the source of the *acoustic radiation force*, whereas the time-averaged second-order velocity $< v_2 >$ gives rise to *acoustic streaming*.

In a physical sense, these second-order time-averaged effects originate from the interaction of the incident acoustic wave with the particles in its path (the ARF) and the fluid it propagates through (streaming). The acoustic radiation force originates from the interaction of the incident (primary) acoustic field with the particle-scattered (secondary) field, as the particles in the acoustic path act as scatterers [74]. Acoustic streaming, the generation of steady flow in the fluid medium of propagation of the acoustic wave, originates from the attenuation of the acoustic wave by the fluid [75], which then induces *streaming-based-drag* on the particles in the acoustofluidic domain.

This sets the context of the origins of the physical effects that are discussed in the coming section as a force interplay. Their relevance with regards to the target application of interest has also been discussed subsequently.

3.3. Force Interplay

The origin of the Acoustic Radiation Force experienced by a particle obeying the Rayleigh criteria ($a << \lambda$) and its analytical formulation was first presented by L.V. King [76] in the form:

$$F_{rad} = 4\pi\phi k a^3 E_{ac} \sin(2kz) \tag{3.5}$$

where,
F_{rad} is the acoustic radiation force experienced by a sphere in a plane standing wave,
ϕ is the Acoustic Contrast Factor,
k is the wave number,
a is the radius of the sphere,

E_{ac} is the Energy Density in the fluid cavity,

Here, ϕ, the Acoustic Contrast Factor determines how the particle is forced in a standing wave field. Particles with positive ϕ migrate to the pressure minima (nodes) and those with negative ϕ to the pressure maxima (antinodes). The Acoustic Contrast Factor is defined mathematically as:

$$\phi = \frac{5\rho_p - 2\rho_0}{2\rho_p + \rho_0} - \frac{\beta_p}{\beta_0} \tag{3.6}$$

where,
ρ_p and ρ_f are the densities of the particle and medium respectively,
β_p and β_f are the compressibilities of the particle and the fluid respectively.

Thus, a slight mismatch in the density or compressibility of a particle over the medium it is suspended in makes the particle 'visible' to the acoustic wave. This is the key concept enabling manipulation of microparticles by acoustic waves in fluids.

Later, Gorkov [77] presented an analytical treatment of the Radiation force on small spheres as the gradient of the potential function containing the time-averaged potential and kinetic energies of a stationary acoustic field. This potential function is now called the 'Gorkov' potential. The force resulting from the Gorkov potential is given by:

$$F_{radiation} = -\nabla U_{radiation} \tag{3.7}$$

where the potential function $U_{radiation}$ is defined by:

$$U_{radiation} = V_p[f_1 \frac{< p_1^2 >}{2\rho c^2} - f_2 \frac{3\rho < v_1^2 >}{4}] \tag{3.8}$$

where, f_1 and f_2 are scattering coefficients given by:

$$f_1 = 1 - \frac{\beta_0}{\beta_p} \tag{3.9}$$

$$f_2 = \frac{2(\rho_p - \rho_0)}{2\rho_p + \rho_0} \tag{3.10}$$

here,
V_p is the volume of the particle in the acoustic field
p_1 and v_1 are the first-order pressure and velocity respectively.
$<>$ is the time-averaging operator.
ρ_0 and ρ_p are the densities of the medium of propagation and the particle respectively, and
β_0 and β_p are the compressibilities of the medium and the particle, respectively.

The formulation by L.V. King and Gorkov sets the base for the analytical determination of the acoustic radiation force on particles obeying the Rayleigh criterion ($a << \lambda$) for inviscid fluids. Practically, this formulation is valid for particles larger than the viscous boundary layer which is of the order of 1 μm for the frequency ranges in consideration here [78]. The viscous boundary layer thickness is given by:

$$\delta_v = \sqrt{\frac{2\eta}{\rho_0 \omega}} \tag{3.11}$$

where,
η is the Dynamic Viscosity
ρ_0 is the Density of the Fluid Medium
ω is the Angular Frequency

This means that the forces on the particle sizes of interest of the order of 10 μm can be estimated by the formulations described in this section.
Typical force magnitudes range from a few nN to sub-pN magnitudes. It can be observed from the above relations that the Radiation Force scales with the particle volume V_p and thus is dominant for larger particles.

The above expressions analysis considers the *Primary* effect arising from the harmonic source field interacting with the particles in its path which act as scatterers. However, for high particle concentrations, the particle-particle interaction becomes significant giving rise to a *Secondary* effect arising from the interaction of the scattered fields of particles in the close vicinity of each other. This was first presented analytically by [79]. The approach used herein was to estimate the effect of the scattered field by one particle on another particle in its vicinity with a two-particle model. The analysis shows that the emerging in-plane Secondary Radiation Force component (SRF) can be denoted analytically as described in [79] and [80]:

$$F_{secondary,radial} = 4\pi a^6 (v^2(z) \frac{(\rho_p - \rho_0)^2 (3\cos^2(\theta) - 1)}{6\rho_0 d^4} - p^2(z) \frac{\omega^2 \rho_0 (\beta_p - \beta_0)^2}{9d^2}) \tag{3.12}$$

where,
a is the particle diameter,
$v(z)$ and $p(z)$ are the velocity and pressure fields in z direction respectively,
ρ_p and ρ_0 are the densities of the particle and fluid medium respectively,
θ is the angle between the wave propagation direction and the line connecting the centers of the two particles,
β_p and β_0 are the compressibilities of the particle and fluid medium respectively,
ω is the angular frequency,
d is the interparticle distance.

The first term of the SRF expression depends on the orientation of the particles with respect to the propagation direction of the incident wave. For two particular cases, the first term can be qualitatively interpreted. Firstly, if $\theta = 0^o$, which means that the particles are lined up parallel to the incident wave direction, the term has a positive contribution, depicting the repulsive nature of the force. On the other hand, if $\theta = 90^o$, the term has a negative sign depicting an attractive force. The interesting observation is also that the second term is zero at the nodal plane (as $p = 0$) and thus, once the particles are trapped in the nodal plane, the SRF is purely attractive in nature. The fact that the SRF scales with the inverse of d^4 means that at sufficiently small interparticle distances, the SRF can be strong enough to cause aggregation and clustering. This concept would be discussed in further chapters as well while linking the theory to experimental findings.

The second effect that participates in the force interplay in acoustofluidic manipulation systems is Acoustic Streaming. Initial studies of the onset of streaming in acoustically actuated systems were first carried out in the mid-1900s [81]. Acoustic streaming originates from the second-order velocity term $< v_2 >$, resulting from a non-zero time-averaged particle velocity resulting from viscous attenuation of the acoustic wave by the fluid. The time-averaged effect gives rise to steady flow vortices in the fluid bulk and boundary layers, which in turn result in a drag force on the particles in the fluid. This steady flow is usually of two types, namely the boundary layer streaming and the bulk (or Rayleigh) streaming. The bulk streaming causes particles to move with the fluid in vortices if the drag force dominates the radiation force.

The Drag Force is given by:

$$F_{drag} = 6\pi a \eta (v_{fluid} - v_{particle}) \tag{3.13}$$

where,
a is the radius of the particle in the acoustic field
η is the dynamic viscosity of the fluid medium
$v_{relative} = v_{fluid} - v_{particle}$ is the relative velocity of the particle.

A typical streaming pattern in half-wavelength resonators consists of a pair of counter-propagating fluid vertices per half-wavelength in the propagation direction of the acoustic wave [82] as shown in Figure 3.1. The physical origin of the streaming lies in the viscous boundary layers parallel to the wave propagation wherein there is a sharp velocity gradient and large viscous dissipation resulting in a steady vortex flow. The bulk flow is then set up as a counter-propagating vortex to the inner (boundary layer) streaming flow. This effect of the representative boundary layer δ_{v2} from Figure 3.1 that produces the bulk streaming is usually valid when the characteristic length h is of the order of λ. However, the bulk streaming can still be observed even if $h > \lambda$ resulting from the formation of another boundary layer (δ_{v1}) perpendicular to the wave propagation arising from the flexural vibrations of the matching and reflector layers [83, 84, 85]. The combined picture of the above-mentioned effects is shown in Figure 3.1.

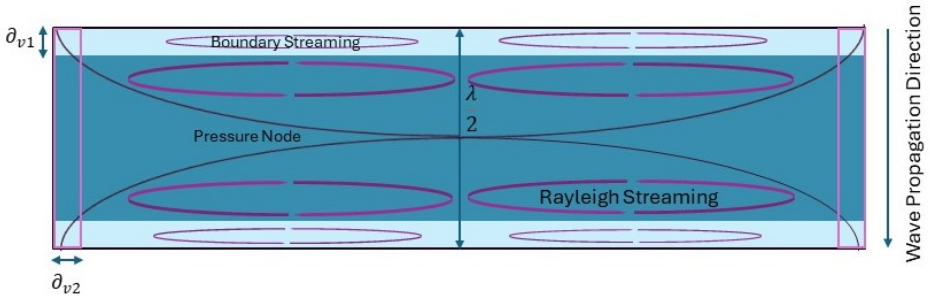

Figure 3.1: Outer and Inner Boundary Layer Streaming

From the above discussion and analytical formulation, it can be observed that the Drag Force is significant for smaller particles due to scaling with the particle radius.

Lastly, an important physical quantity of consideration from the point-of-view of acoustic device design is 'Acoustic Impedance'. The choice of materials for acoustics, and their performance depends on the acoustic impedance, a measure of the resistance offered by a material to the flow (or motion of particles) resulting from an acoustic pressure field. Numerically, the acoustic impedance is quantified as:

$$Z = \rho c \tag{3.14}$$

where,
ρ is the density of the material and c is the speed of sound in the material.
Interfaces of media reflect or transmit acoustic waves based on their relative acoustic impedance. The reflection coefficient of an interface is given by:

$$R_p = \frac{Z_2 - Z_1}{Z_2 + Z_1} \tag{3.15}$$

where,
Z_1 and Z_2 are the characteristic acoustic impedances of the first and second medium respectively.
The nature of the standing acoustic wavefield in heterogeneous resonators can be designed with careful considerations regarding characteristic impedances, and details of these have been provided in Chapter 4.

3.4. Relevance: Key Effects

The previous section outlined the governing principles for the primary and secondary acoustofluidic effects in a system similar to the one presented in this work. The 3 key players, the PRF, SRF, and Streaming contribute to the objective of achieving stable clustering in different functional ways, which is depicted in Figure 3.2. These key players have been linked to the experimental observations and inferences have been drawn on these grounds in Chapter 6.

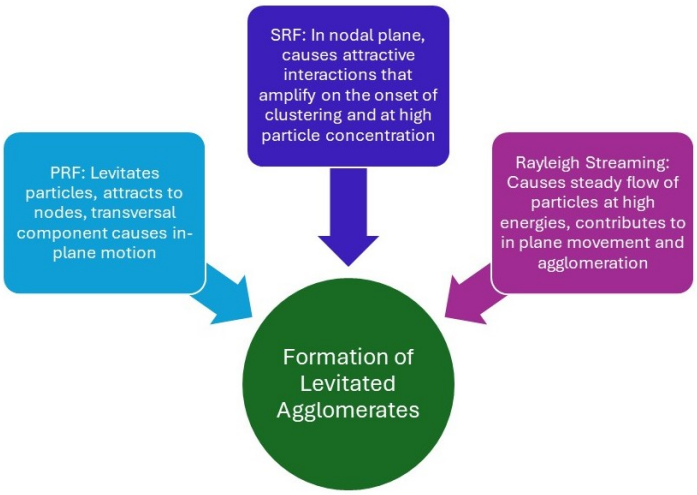

Figure 3.2: Force Interplay Considering the Application.

3.5. Quantifying the Research Objective

Building on the qualitative research objective presented in Chapter 2, the quantitative parameters of the research objective are outlined herein:

- Conceptualizing the device design to dimensionally accommodate particle clusters up to 500 μm in size, and the associated fluidic chamber relatable to 48 well plate structures.
- Demonstrating the manipulation technique for particle mimics for neuronal progenitor cells (cell body $\sim$ 10 μm in diameter).
- Achieving an initial clustering time of up to 5 minutes and system robustness to sustain the clusters for longer exposure periods.

4

Materials and Methods

4.1. Introduction to the Design

Building on the overview of acoustofluidics, governing principles, effects of interest, and their potential applications outlined in the previous chapter, this chapter presents the device design, right from conceptualization and rationale, to the simulations of the device performance.

BAW devices have been one of the preferred choices for integration with microfluidics for handling of particles in the μm length regime due to their ease of prototyping and modelling, effective transmission of acoustic energy from transducer to fluid through matching layers, and compatibility with applications such as cell sorting and handling [86]. Typically, for applications involving trapping and localization of particles, standing wave devices are a suited choice, owing to the simplicity of the device and performance design. However, they also pose some challenges over traveling wave devices, particularly in terms of the dimensional accuracy/tolerances that need to be achieved for the optimal generation of the standing wave.

Typically, standing wave modes are established in microfluidic systems either by pairs(s) of transducers that produce oppositely propagating waves that interfere constructively to form a standing wave, or, with pair(s) of transducers and reflectors wherein the reflected wave interferes constructively with the incident wave to form a standing wave. Although deploying multiple transducers in various directions offers a higher flexibility and spatial control over the standing acoustic field, there are two major drawbacks: firstly, it involves either complex circuitry which makes integration with biological experiments challenging, or calls for the design of a PCB exclusively for the purpose, which was out of the scope of the area of study; and secondly, multiple transducers pose the challenge of limited optical access (due to orthogonal transducers affixed on all surfaces of the device), which hinders the microscopic observation of cells (and microparticles) in live experiments. For the above-cited reasons, this work involved the creation of a ‘resonator’, or a *transducer-reflector pair-based* trapping device.

4.2. Acoustic Resonators and Choice of Device Structure

Acoustic resonators are the group of devices that employ transducer-reflector pair(s) to set up ‘resonances’, or standing wave(s) in the target medium. They generally have a stacked structure, which consists of the transducer, matching layer(s), the resonant cavity, and the reflector. This stacked structure can be employed in two different modes, namely the ‘Layered’ mode and the ‘Transversal’ mode. Figure 4.1 depicts these two modes of resonators in BAW acoustofluidic devices.

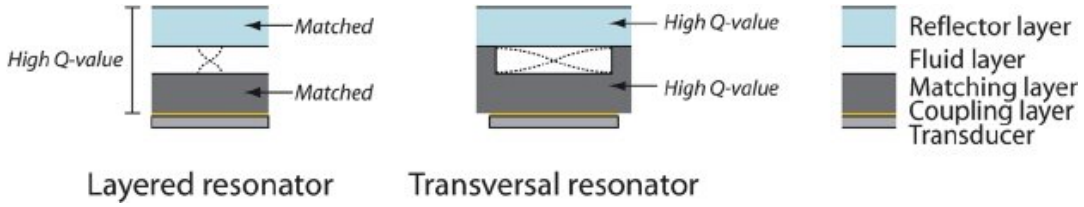

Figure 4.1: Layered and Transversal Resonator Structures from [87].

In layered BAW resonators, the resonance is created by the reflection between the air-backed reflector and transducer, and thus is not greatly impacted by the materials used for the channel. However, in transversal mode, the channel walls create the resonance, which makes it essential that the channel is made from high acoustic impedance materials such as silicon, glass, or metals, and has precisely fabricated parallel walls. This is possible by employing microfabrication for creating the channels in Silicon, however, this limits the optical access. Glass-based fabrication by laser micromachining is an alternative to this, however, this poses challenges such as trenches, and angled walls resulting from laser ablation which affect the acoustic performance. In terms of the target functionality, the transversal mode alone might be insufficient to create a trap that enables levitated clustering of cells. This is another limitation which would need added components and design considerations to reach the targeted application. On the other hand, layered BAW resonators create a trap in the z-direction, which enables trapping the cells in a contact-free manner. It also enables greater optical access, and allows for the use of cell-friendly materials for microfluidics such as polymers, without affecting the resonance greatly.

Taking into account the limitations posed by the transversal mode, a layered BAW device design was chosen as the base design, which was then optimized to reach the final design. The layered structure of the device is depicted in Figure 4.2.

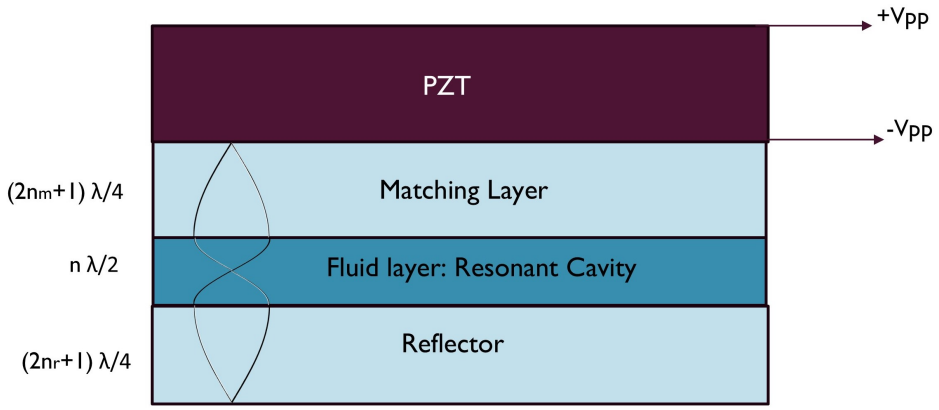

Figure 4.2: Representative sketch of the base design of a Layered BAW Resonator.

4.3. Material and Dimensional Considerations

Layered BAW resonators, though simple in construction, are faced with the challenge of dimensional accuracy in the thickness direction. Fine-tuning the thicknesses of the stack layers is crucial for an ideal performance. Furthermore, it is also essential to choose materials that create the correct match in terms of acoustic impedance to ensure strong reflections at crucial boundaries, and to minimize unwanted reflections elsewhere. Lastly, considering the working lengthscale regime for this project, it is also essential to allow for flowcells that can accommodate cell clusters (typically up to a few hundred μm in size), for scalability to organoid cultures. Similarly, the experiments were carried out

on microparticles that act as suitable mimics for the target cell properties. Taking into consideration all of these intricacies, the following materials and dimensions were chosen:

- **Glass**: Glass was chosen as the material for the matching and reflector layers. The large impedance mismatch between glass and the water (loading medium) ensures a strong reflection at the glass-water reflector interface, which is desirable. To ensure minimal processing time and high precision, laboratory soda lime glass slides with mean thickness 1000 $\pm$ 5 μm were used. The slides were cut to the required size (planar) by laser cutting, details of which would be outlined in the next section.

- **PDMS**: PDMS was chosen as a material for the fluidic channel. Due to a close match in acoustic impedance between PDMS and water, PDMS channel walls ensure minimal in-plane reflections which is desirable to obtain a strong standing wave in z-direction. PDMS also has been a prominent choice in bio-microfluidics due to its biocompatibility. PDMS is easy to manufacture, and can be cast into required shapes and dimensions by soft lithography. Thirdly, PDMS is compliant, and this makes it suitable to set up microfluidic connections with ease. Lastly, PDMS forms strong, leak-tight bonds with glass, and can also be spun into very thin layers by spin coating. Each of these characteristics supports a specific fabrication or functional requirement which leads to this choice, details of which are outlined in subsequent parts of the thesis.

- **Microsphere Solution**: Polystyrene ($\rho = 1.07 \quad gm/cm^3$) microspheres suspended in distilled water were used as the experimental solution to test the device. The initial solution was created by adding 10 μg of the microsphere powder by Cospheric to a 1 mL vial of distilled water. This solution was diluted 250 times to create the base concentration for the experiments.
  Polystyrene possesses acoustic properties in comparison to water that are tested standards for characterizing the acoustic manipulation of cells [7], and has been a widely used material therein. Particles 10 μm in diameter were used as cell mimics in this study, as this resembles the typical sizes of the target cells, namely neuronal progenitors (soma/cell body 10 μm in diameter). Tween-20 was added to the solution (0.05% vol/vol) to act as a surfactant and minimize the adhesion of the beads to each other.

- **Transducer**: The acoustic wave is generated by a harmonic excitation of a piezoelectric transducer. The transducers employed are PZT-based piezoelectric discs (coated with silver electrodes and with wrapped-around contact pads) by PI (Physik Instrumente GmbH). The material of the transducers is a modified piezoceramic PIC 181, particularly chosen for its suitability for close-to-resonance operation, thermal stability (low dependability of mechanical properties on temperature), low dielectric losses and high piezoelectric coupling factors [88, 89]. The transducer was fixed to the fluidic chip by cyanoacrylate glue.

4.4. Device Characteristics

Based on the material choices outlined in the previous section, the base design of the resonator was created. This consisted of a fluid resonant cavity 520 μm thick, with glass matching and reflector layers 1 mm thick as described above. The device materials were chosen based on suitability for the target application as well as availability for a fabrication workflow that fits the project timeline. Thus, glass slides were selected for the matching and reflector layers, and the fluid channel depth was chosen accordingly. In order to match the acoustic impedance of the glass layer with the fluid loading layer, a thin spin-coated layer of PDMS was added to the stack. This ensures that the transducer-glass-PDMS stack creates an effective transmission of acoustic energy to the fluid cavity (loading medium). However, the high-frequency attenuation and the compliant nature of the acoustic field by the PDMS layer is also an important consideration, which led to an optimal thickness range of

60-100 μm, as a tradeoff between attenuation, fabrication suitability, and impedance matching, while keeping the resonance characteristics desirable and predictable. It also is notable that the PDMS layer, having similar acoustic impedance as water, does not alter the field in the fluid layer abruptly, and thus in turn allows for minor deviations in the fluid layer thickness. The final outcome of the design process is depicted in the Figure 4.3.

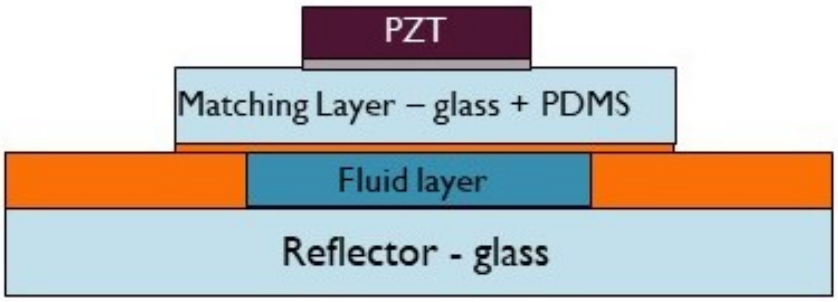

Figure 4.3: Cross-sectional View of the Device Design.

Based on Figure 4.2, the layer thickness ratios for the layered stack comply with the optimal values as follows:

- Matching and reflector layer thicknesses of 1000 μm result in an acoustic wavelength of 4000 μm or 4 mm.
- This results in an acoustic wavelength of approximately 1040 μm in water based on the ratios of the speed of sound between glass (5647 m/s) and water (1480 m/s) for a given frequency.
- This yields the optimal fluid layer thickness for a half wave resonance mode in the fluid cavity to be close to 520 μm, which is the targeted fluid cavity thickness.
- The lateral/in-plane geometry was chosen as follows:
  - The diameter of the well is chosen to be large enough to avoid plane wave attenuation due to the PDMS spacer layer in its path, and enable an effective transfer of energy from the PZT to the fluid well.
  - The diameter of the well is chosen to be 10.4 mm, which corresponds to the dimension of a 48-well plate. This is chosen based on the size of the transducer and the overall size limit of the chip (governed by the standard size of the glass slide).
  - The walls of the fluid well are curved, aimed to ensure minimization of stray in-plane reflections from the chamber walls that can disturb the 1D standing wave field (straight side walls can create weak reflections in-plane, thereby affecting the standing wave in z-direction).

4.5. Device Fabrication

The fabrication process of the device was carried out in two steps. Firstly, each of the layers of the stack was processed individually, and in the second step, the layers were assembled by a series of

processes to complete the device fabrication. The two steps and the assembly process flow will be described in detail in the next subsections.

4.5.1. Layers in the Stack

Aptly described by the term 'layered resonator', the device fabrication consists of a stack of layers that were made to size individually, followed by their assembly. The fabrication of the individual layers was carried out as follows:

- **PDMS Channel**: The crucial component of the resonator is the fluidic chamber. The flow cell was designed in PDMS based on soft-lithography. This process consists of multiple sub-steps as below:

  - *Making of the Mold*: The final mold for casting of PDMS was designed with a tolerance of 1% percent in thickness dimension for shrinkage and 5% for casting dimensional compensation [90], and was 3D-printed by an ASIGA DLP 3D-printer using a methacrylate-based MoiinTech clear commercial resin, with a slice thickness of 10 μm. The mold was post-processed in an ultrasonic bath in IPA and water to remove the residual resin and post-baked in a UV curing lamp setup. Further, to render the mold hydrophobic for effective demolding of PDMS, the mold was silanized in a vacuum desiccator in the fumehood at a pressure of -600 mbar for 4 hours to create a thin monolayer of the silane. The silanizing agent Trichloro (1-H, 1-H, 2-H, 2-H-perfluorooctyl) silane was used to create a self-assembled monolayer on the molds. The contact angle was checked by placing a drop of water on the silanized surface as shown in Figure 4.5.

  - *Making and Casting of PDMS*: PDMS was prepared using the Sylgard 184 polymer kit. The prepolymer and curing agent were measured in a ratio of 10:1 (by weight), and mixed for 5 minutes with a pipette. The mixture was then poured into the molds for casting. The PDMS was first poured in excess and the extra PDMS was scraped off with a sharp glass slide edge to level the casting. Further, the molds with poured PDMS were placed in the desiccator for 30 mins at -600 mbar for degassing.

  - *Baking and Demolding PDMS*: After degassing, the molds were placed in the oven at 75^{o}C for 1.5 hours, which resulted in complete curing, and enabled successful demolding. After the baking was completed, the PDMS was separated from the edges of the mold by a scalpel, and then gently peeled off from the mold with a flat soft-tip tweezer at an approximate rate of 3 mm/min. This completes the fabrication of the fluid spacer layer. An example of a demolded PDMS membrane spacer layer can be seen in Figure 4.6.

- **Matching Layer**: The matching layer is a stack of a glass slide cut to size (25 mm x 35 mm), and a spin-coated PDMS layer. The glass slide was cut to size using the Lasea LS-Lab femtosecond laser micromachining system, with the parameters as depicted in the workflow Figure 4.11. The process consisted of creating a thin line cut and shearing the glass manually along the created guide cut-line. The machined glass was then cleaned with acetone+ IPA+ air gun drying, and was then used as the substrate for spin-coating PDMS. PDMS was prepared using the Sylgard 184 kit as outlined in the previous point, and spin-coated at 500 rpm for 5 mins on glass, building the recipe on the spin-coating curves by Elveflow [91]. The spin-coated PDMS was then cured on the glass substrate at 75^{o}C for 1.5 hours to complete the matching layer.

- **Reflector**: The reflector consisted of a glass slide laser cut to size larger than the matching layer (25 mm x 55 mm) to enable fluid connections and was made ready for assembly by the cleaning steps that would be described later.

- **PDMS Blocks for Inlet/Outlet**: PDMS was prepared by the above-mentioned methods and poured in a petridish, cured and cut into blocks of 1.5 x 1.5 cm in size, to be used in the bonding step.

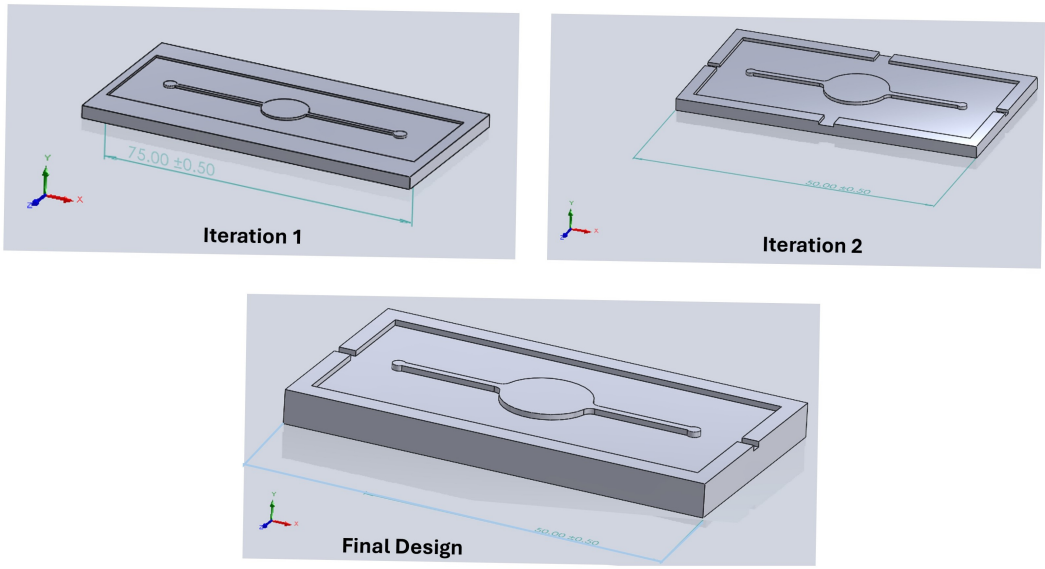

Figure 4.4: Mold Design Iterations and Final Design.

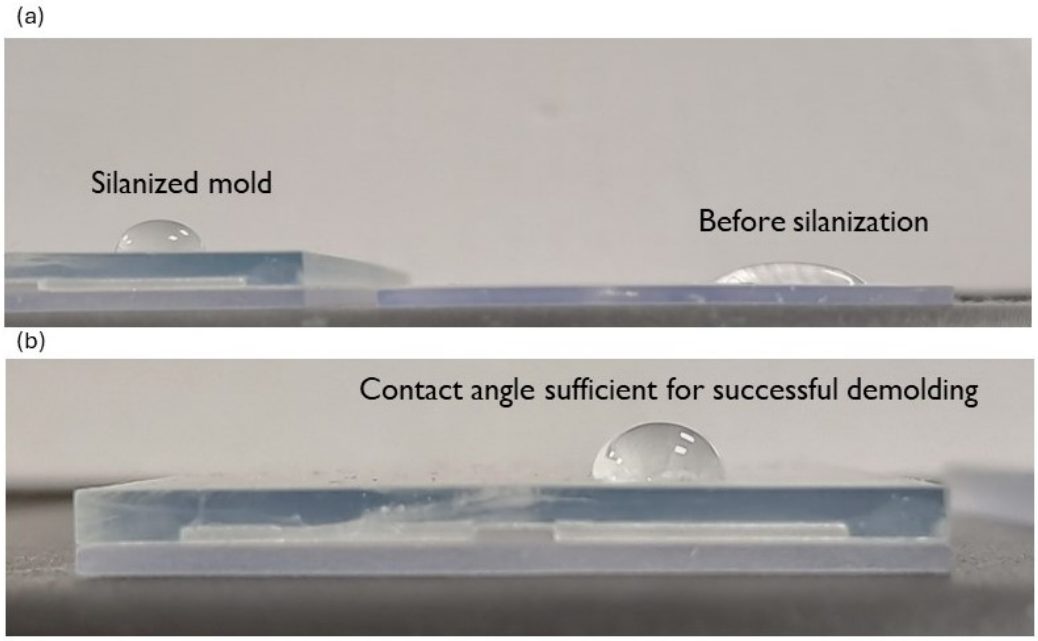

Figure 4.5: Checking the contact angle after silanization, (a) depicts a comparison between a silanized and non-silanized mold, (b) depicts a contact angle that was sufficient for effective demolding.

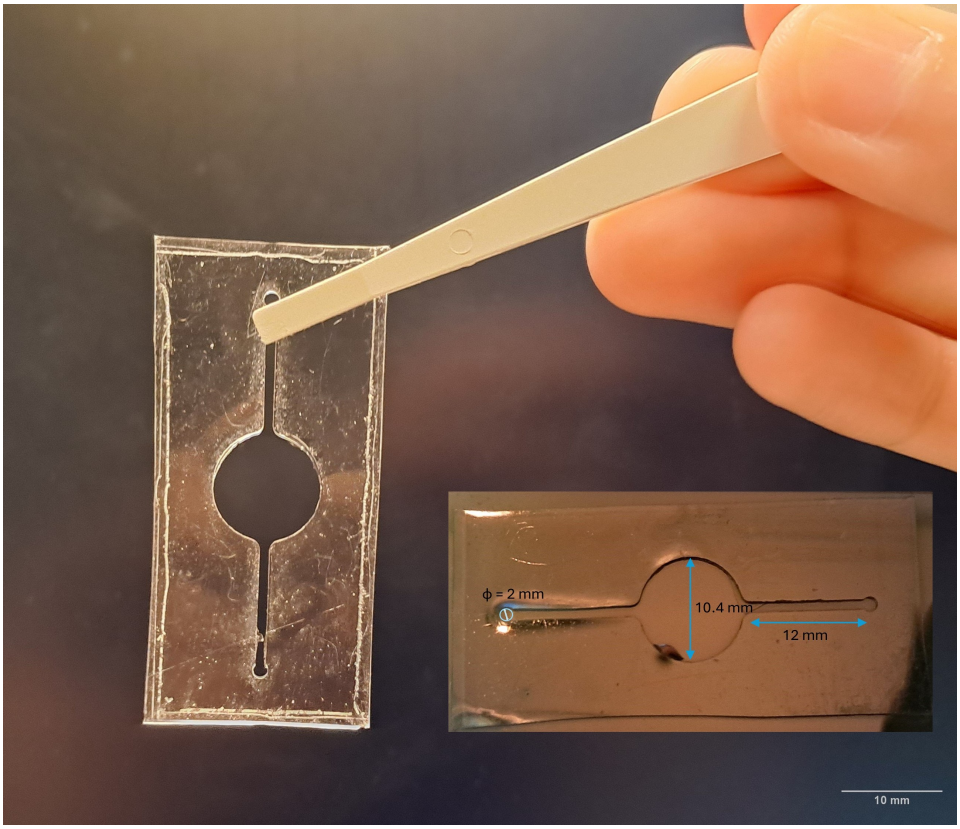

Figure 4.6: A demolded PDMS layer with the dimension sketch of the design.

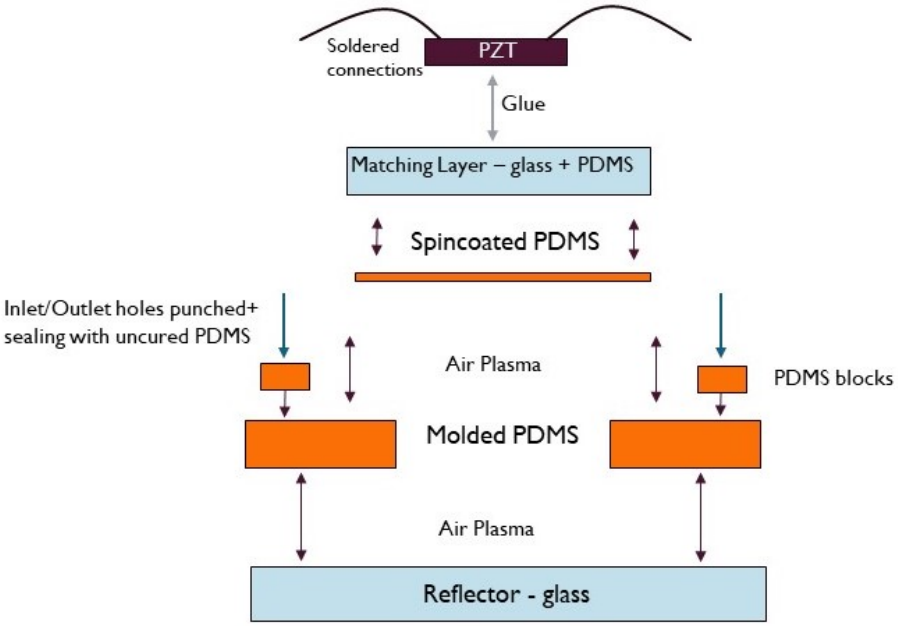

Figure 4.7: Process Diagram for Assembly of the Individual Stack Layers.

4.5.2. Assembly of the Device

After each of the individual layers were prepared, the assembly was carried out with multiple processes as depicted in Figure 4.7. The crucial step included the plasma bonding and the gluing of the transducer. Plasma exposure is a commonly used technique to activate the PDMS and glass surfaces to create permanent Si-O-Si bonds at the PDMS-glass interface when brought in contact. Before the bonding step(s), all the PDMS components were cleaned with IPA+ water+ air gun drying (acetone was not used as it was observed to cause warping and swelling), and all the glass layers with acetone+IPA+water+air gun drying. The next process steps are described below:

- **Plasma Bonding: Reflector-PDMS Spacer**: The cleaned PDMS channel layer was placed on a clean, (extra) glass slide, ensuring appropriate alignment. This channel layer was then placed in the Diener Femto plasma cleaner along with the cleaned reflector slide. The layers were exposed to air plasma at 100% power, and 3 mbar pressure for 2 minutes. The recipe was developed based on multiple trials by varying the pressure and the exposure time. A low exposure time fails to activate the PDMS surface sufficiently, whereas a very long exposure time erodes the PDMS surface resulting in inconsistent bonding. Thus, an optimum was found at the parameters described here. After the exposure, the layers were picked up with tweezers ensuring that the exposed surfaces are not touched/contaminated, and pressed against each other, gradually lowering the reflector over the channel layer to push out any air bubbles. The bonding is best completed within a minute of plasma exposure. The stack was pressed down for about 3 minutes, after which the bond is strong enough to take off the extra glass slide that was used as a holder of the PDMS layer.

- **Plasma Bonding: Matching Layer-PDMS Spacer and PDMS Blocks**: In the second round of plasma exposure, the bonded PDMS-reflector stack was placed in the cleaner (PDMS side up), along with the matching layer (PDMS side up) and the PDMS blocks. The plasma exposure was run once again with the same parameters, after which, in less than a minute, the matching layer was aligned and bonded to the reflector-spacer half, followed by bonding of the PDMS blocks to the inlet and outlet ports in the PDMS spacer layer to complete the sealing of the spacer.

- **Post-baking and Creation of Inlet/Outlets**: After the plasma bonding was complete, the stack was post-baked in the oven at 80^{o}C for 2 hours to strengthen the bond. Post baking, the inlets and outlets were made using a biopsy punch (diameter 0.5 mm). A hole was punched in the PDMS blocks using a biopsy punch, and a dispenser tip (diameter 0.6 mm, gauge 22) was inserted in the hole to create a tight press-fit. The interface of the dispenser tip and the punched hole was sealed with uncured PDMS and a quick bake at 75^{o}C for 1 hour was done to ensure the PDMS cures before it can flow in and block the fluid channel. This completes the sealing of the flow cell. The leak-tightness can be assessed by inserting a dyed fluid as shown in Figure 4.9.

- **Transducer connection**: The PZT was attached on top of the matching layer aligned with the fluid well with Bison Cyanoacrylate glue (superglue). In order to ensure good electrical contact, a drop of silver paste was placed on the matching layer surface, followed by the application of the glue with a brush to ensure a uniform layer. The piezo was placed and gently pushed down to release the excess glue at the edges. In order to achieve a quick cure of the glue, an activator spray was used to cool and rapid-cure the glue. All these processes were carried out in the fume hood. Finally, the thin copper wires (0.5 mm in diameter) were soldered to the piezo electrodes (both on the top surface). Solder flux was used to ensure a good connection.

The completed device, as a representative, looks as depicted in Figure 4.10.

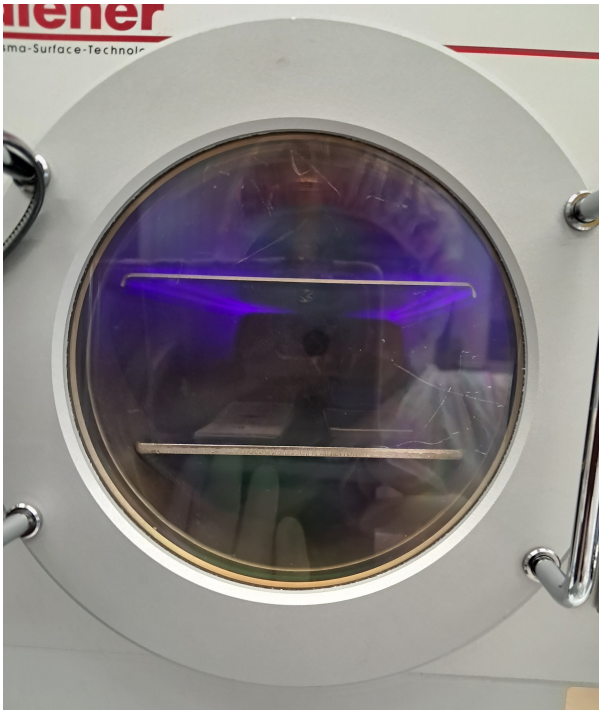

Figure 4.8: The plasma chamber showing the characteristic purple colour of air plasma.

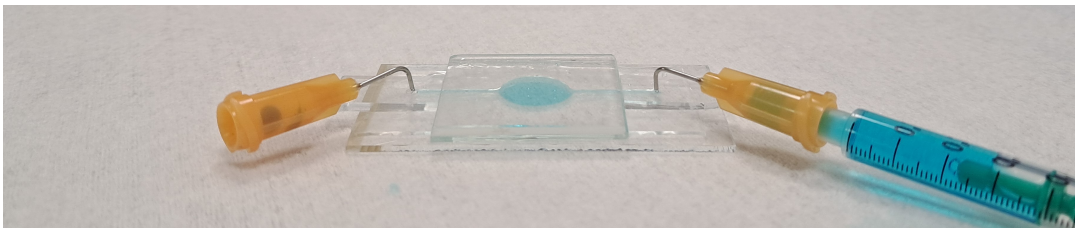

Figure 4.9: A completely assembled, leak-tight fluid channel.

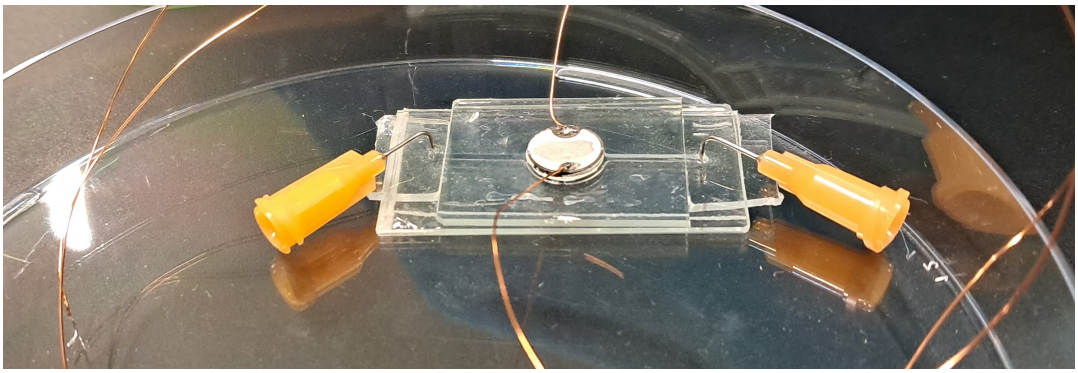

Figure 4.10: A completed device after fluidic connection, PZT attachment and Electrical Connections.

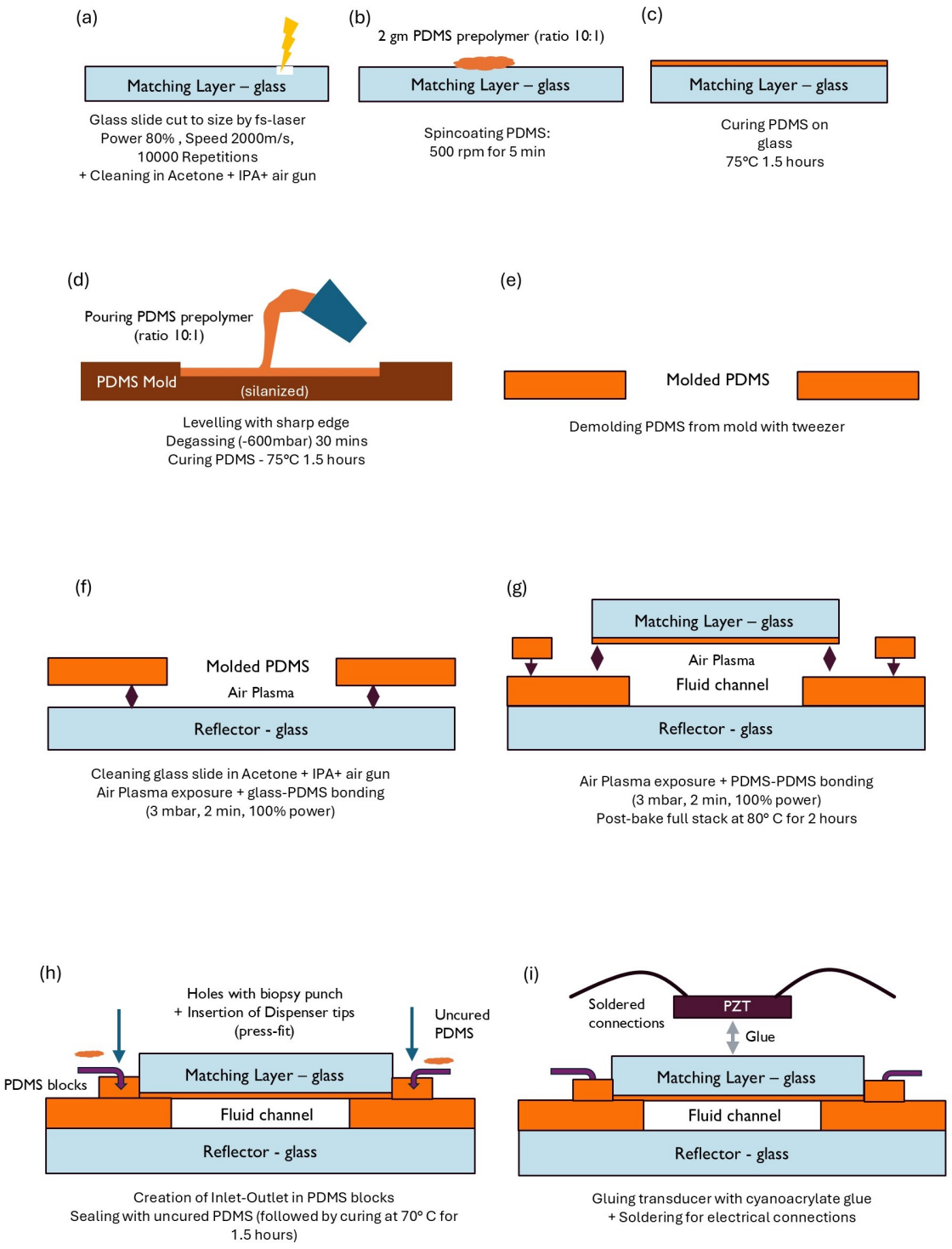

Figure 4.11: The detailed fabrication workflow.

4.5.3. Sources of Tolerances and Errors

The fabrication process outlined above consists of multiple manual steps, each of which introduces possibilities of imperfections and tolerances. These anticipated sources of errors have been described therein, and have been mapped against the observed outcomes and their impacts in Chapter 5 of this thesis.

- **PDMS molding**: The most crucial step in the fabrication workflow also brings in the most possibilities of imperfections. These sources of error are as follows:

  - *3D printing of mold*: The casting is done with the help of a 3D printed mold. The dimensional resolution of the 3D printer was sufficient for the target dimensions needed, however, the surface roughness of the resulting print was a critical player, also affecting further steps in the fabrication process. The mold design was created such that it fits the maximum print area of the printer, which minimized surface roughness as the layers were printed in the thickness direction. However, the DLP-based printing still resulted in a surface that had some amount of roughness, artifacts and imperfections. Further, a sturdy base plate had to be added to the design in order to avoid warpage of the mold during or after printing.

  - *Mold post-treatment and silanization*: Ultrasonic cleaning of the mold was carried out to minimize residual resin and post-curing was carried out, followed by silanization. The possible sources of error herein constitute mainly the non-uniform silanization which renders the surface partially hydrophobic, and thus causes cracking and breaking of the PDMS layer.

  - *PDMS casting and curing*: PDMS was cast in the molds after surface treatment. The PDMS was poured in excess first, and the extra was scraped down by a sharp edge. This process can introduce errors such as incorrect or inconsistent layer thickness across the PDMS layer. Further, during degassing and baking, the PDMS is handled while it is poured in the mold. Ensuring the flatness of the surfaces where the molds are placed is important, as, if not taken into account, the PDMS might cure into a slanted layer, which can cause functional issues in the device.

  - *PDMS spin coating*: To create the PDMS thin film, spin coating is used. It is essential that the PDMS is coated on a clean glass surface, and the amount of PDMS used is sufficient to uniformly coat the complete surface. Further, while baking the PDMS on glass, it is once again necessary that the surfaces are as flat as possible to create a uniform layer.

- **Plasma Bonding**: The layers in the stack were bonded by exposure to air plasma. Inconsistencies in plasma exposure, contamination of the surfaces or the chamber gas, deactivation of the surface due to delay in bonding after exposure, and trapping of air bubbles at the bonding interface are the sources of error that can arise from this step. These would have an impact on the desired functionality, as well as pose challenges in setting up the system, for example, fluidic leakages.

- **Transducer-chip interface**: Appropriate attachment of the transducer to the matching layer is crucial to ensure a strong coupling between the transducer and the loading layers. The important aspect herein is obtaining a uniform glue layer that is free from air pockets. Any residual air pockets can significantly affect the transmission efficiency of the acoustic energy from the transducer to the layers of interest.

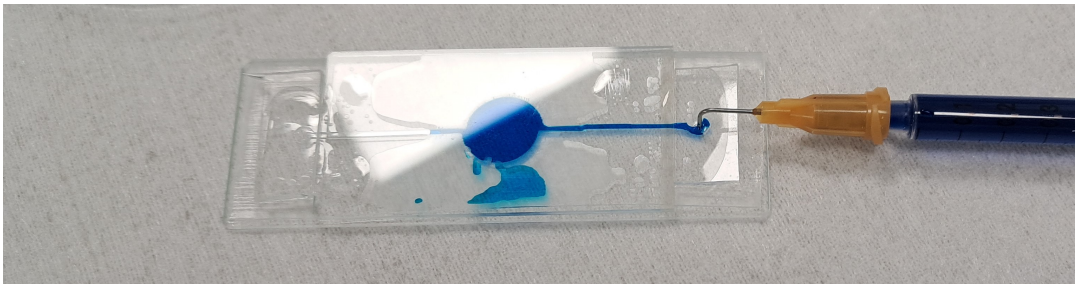

Figure 4.12: Leakage caused by imperfect plasma bonding.

The aforementioned points of consideration with regards to the sources of tolerances in the device fabrication have been referred to in Chapter 5 of this thesis to map the outcome with the anticipated possibilities.

4.6. Characterization Tools and Techniques

In order to characterize the performance of the fabricated device, a wide range of tools and techniques were used, ranging from computational methods to experimental setups. Details of these would be described in this section and forms a base for the presentation of the characterization and experimental results in the next chapter.

4.6.1. COMSOL Multiphysics

COMSOL Multiphysics was used as the primary tool for modeling and simulation of the device performance. Both 2D and 3D models of the complete device were created, and a frequency domain study was carried out as the fundamental study to visualize the acoustic field in the device. As the 3D models were computationally demanding for detailed and iterative simulations, most of the results would be discussed based on the 2D model. The model involved the Pressure Acoustics, Electrostatics, Solid Mechanics modules along with multiphysics couplings for the Piezoelectric Effect and the Acoustic-Structure boundary. The boundary conditions employed were as follows:

- *Pressure Acoustics*: Coupling with solid mechanics interface via the 'Acoustic Structure Interaction' multiphysics.
- *Solid Mechanics*: Linear elastic material model for all the solid layers, piezoelectric coupling for the PZT layer, and free condition for the outer edges of the resonator structures.
- *Electrostatics*: Piezoelectric coupling for the PZT layer. Terminal boundary conditions at the bottom and top edge of PZT, applied voltages -V_{pp} and V_{pp}.
- *Acoustic Structure Boundary* at the interface between the fluid cavity and adjoining layers/domains.
- *Piezoelectric Material* multiphysics interface for the PZT layer.

The analysis involved studying the pressure distribution in the fluid cavity at half-wave resonance, and the optimization of the geometry to conceptualize the final design. The maximum mesh element size was set to $\lambda/12$ to ensure it is sufficient to resolve the acoustic wave [92]. The details of the meshing analysis and material properties used are provided in Appendix B. The pressure field was calculated firstly without introducing suspended microspheres to find the working ranges for the resonance condition, and secondly, particles were introduced to calculate the Acoustic Radiation Force experienced by them at resonance using post-processing. The details of this step have been covered in the Results (Chapter 5). Figure 4.13 shows the layers used in the model.

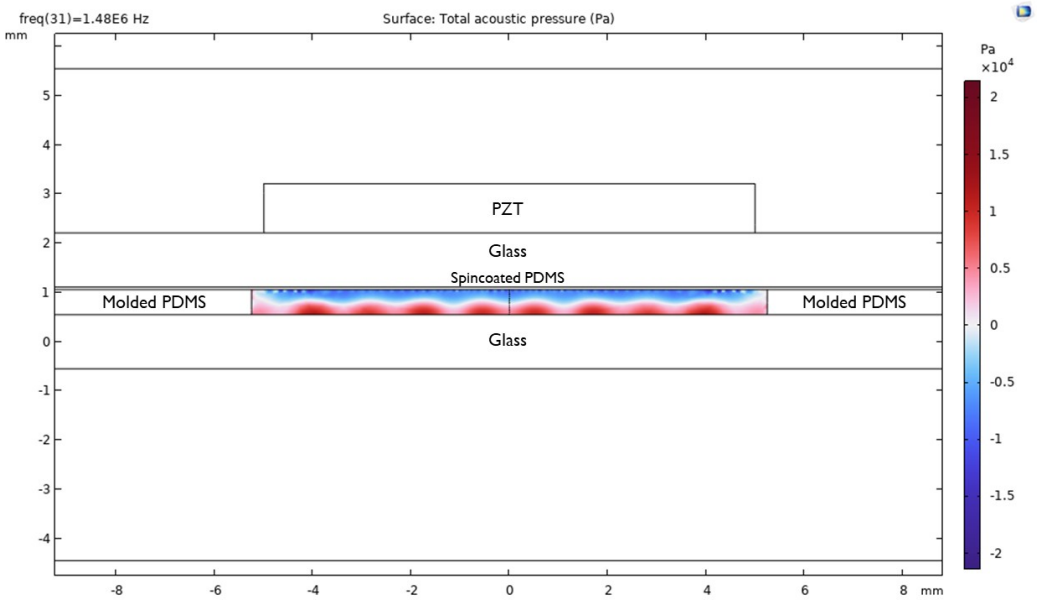

Figure 4.13: The COMSOL model at resonance depicting the material layers of the device

At half-wave resonance, the acoustic field in the fluid cavity and the adjoining layers, as simulated in COMSOL is depicted in Figure 4.14.

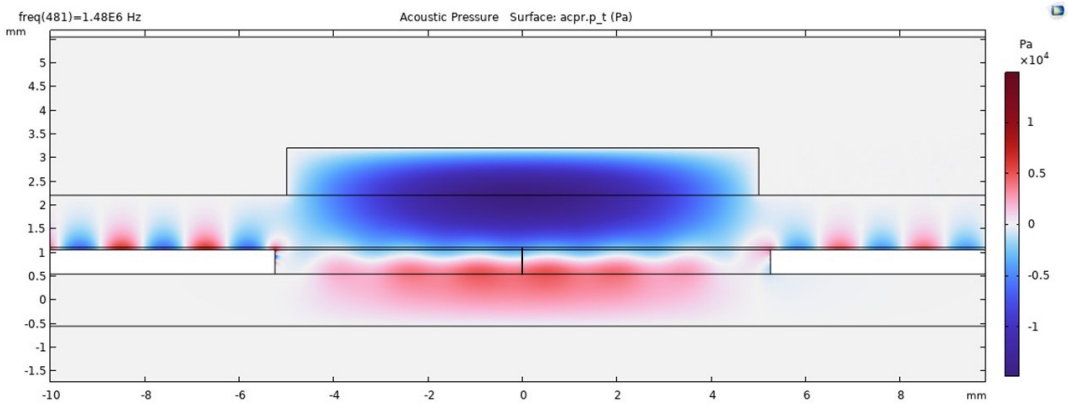

Figure 4.14: The acoustic pressure field in the resonator at the theoretical resonance of 1.48 MHz.

The estimated resonance frequency for half-wavelength mode was observed to be slightly lower than the corresponding analytical estimations. This can be attributed to the multiphysics couplings between the stack layers.

The (absolute) pressure profile in the fluid cavity is extracted by a cut line in the center of the fluid domain and obtaining the absolute pressure values along the cut line. The resulting plot is depicted

in Figure 4.15. The plot shows that the pressure reaches a minimum close to the center of the fluid chamber. The pressure minimum is shifted towards the right (towards the thin PDMS interface) due to the inclusion of the PDMS matching layer adjoining the fluid cavity.

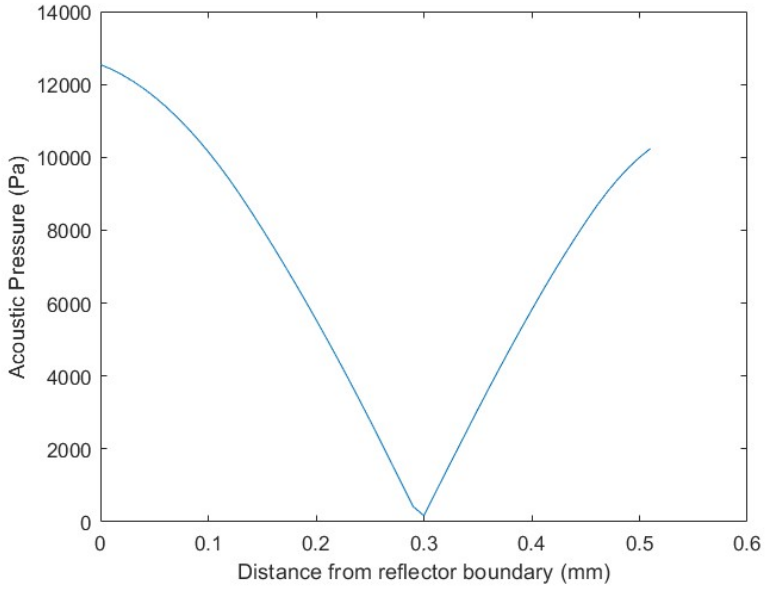

Figure 4.15: The Acoustic Pressure variation along the cut line in the fluid cavity.

4.6.2. Laser Doppler Vibrometry

Interferometry is a set of optical methods that are a common choice in motion analysis in microsystems. In this project, Laser Doppler Vibrometry (LDV) was used as a tool for mechanical characterization of the acoustofluidic chip. The Polytec MSA 400 Laser Doppler Vibrometer was used with the 2x objective. The Laser Doppler Vibrometer works on the basis of the Doppler effect by detecting the frequency shift between an incident and reflected beam of light, from which the velocity of the reflecting object can then be calculated based on the relation:

$$f_D = \frac{2v}{\lambda}, \tag{4.1}$$

which then yields,

$$v = \frac{f_D \lambda}{2} \tag{4.2}$$

where,
f_D is the Doppler frequency shift
λ is the wavelength of the incident light beam
v is the velocity of the reflecting object in motion

The coherent incident light beam of a known wavelength is generated by a laser and the Doppler shift is detected by a laser interferometer. The interferometer creates a laser beam which is split into a reference beam and a measurement beam by a beam splitter. The measurement beam is directed on the moving object and the backscattered beam is then captured, which contains the motion information. The superposition of the backscattered and the reference beam is a modulated signal which contains information of the doppler frequency shift, which is then processed and decoded by the vibrometer controller to obtain the velocity of the object. Figure 4.16 depicts the above described arrangement as presented by Polytec.

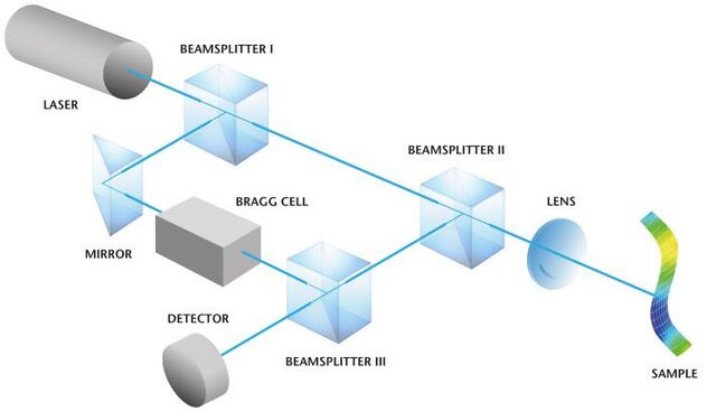

Figure 4.16: Working of a Polytec Laser Doppler Vibrometer [93].

The LDV system was used in the project to characterize the mechanical motion of the transducer when attached to the acoustofluidic chip. The LDV was operated in FFT (Fast Fourier Transform) mode, wherein the system generates a harmonic waveform and scans over a frequency range, records the corresponding velocities of a predefined grid on the sample surface, and displays the result as a frequency response. Thus, it is possible to derive information about the resonance frequencies of the system. In the context of the device under consideration, the LDV-derived frequency response provides information on the shift in the design resonance of the piezoceramic disc on loading with the fluidic chip. This points to an optimal working range for operating the transducer in order to maximize the conversion of electrical energy to mechanical motion which can be seen as velocity peak(s) in the frequency spectrum. A necessary condition to obtain a low-noise, realistic measurement from the LDV is that the object surface needs to be reflective. For this purpose, a thin film of Aluminium foil is glued to the surface of the transducer to obtain a highly reflective signal. The Polytec MSA 400 system is able to measure the system frequency response up to a value of 2 MHz, hence the device response only up to 2 MHz could be visualized. The detailed results have been explained in Chapter 5.

(a)

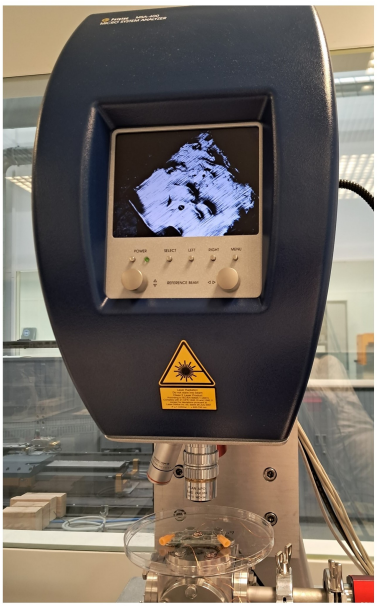

(b)

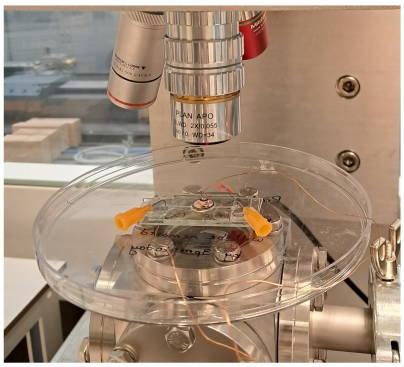

Figure 4.17: The LDV system: (a) depicts the laser head unit, (b) shows the device mounted on the LDV system for measurements.

4.6.3. Inverted Brightfield Microscopy

The recording of the motion of the microspheres was carried out by digital inverted brightfield microscopy using the *Nikon ECLIPSE Ti2* system with a 10x objective (working distance of 4 mm) and an automated stage. The microscope camera has a field-of-view array of 2048 x 2048 pixels and has a maximum frame rate of 50 fps. The microscope was operated in brightfield mode with a white light source, and an exposure time of 20 μs was used for image acquisition. The images, videos and image stacks were acquired with the NIS elements software interface. The device was setup such that the electrical and fluidic connections can be accessed from the topside and the optical access can be achieved from the bottom through the glass reflector layer (being transparent). Thus, the chip is compatible with live microscopy, which is a huge advantage when it comes to application in organoid cultures. Figure 4.18 shows the acoustofluidic chip mounted on the inverted microscope.

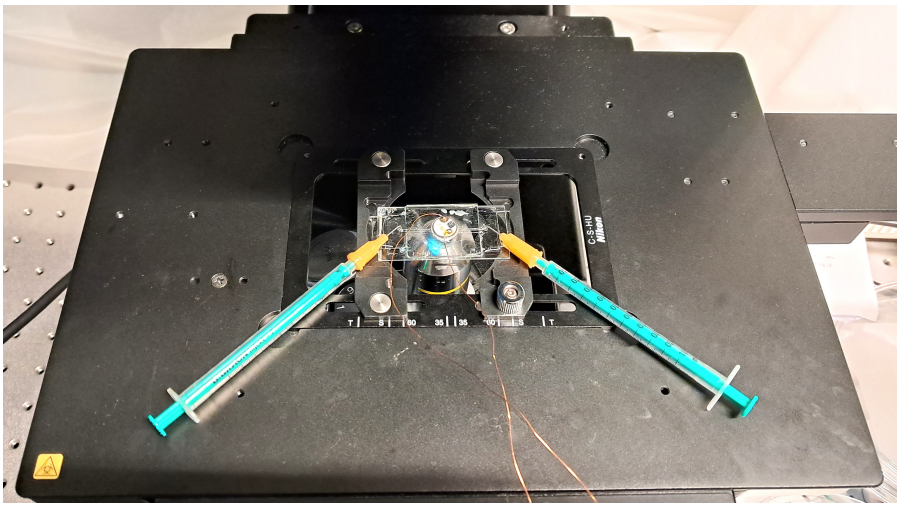

Figure 4.18: Acoustofluidic chip mounted on the inverted microscope for imaging.

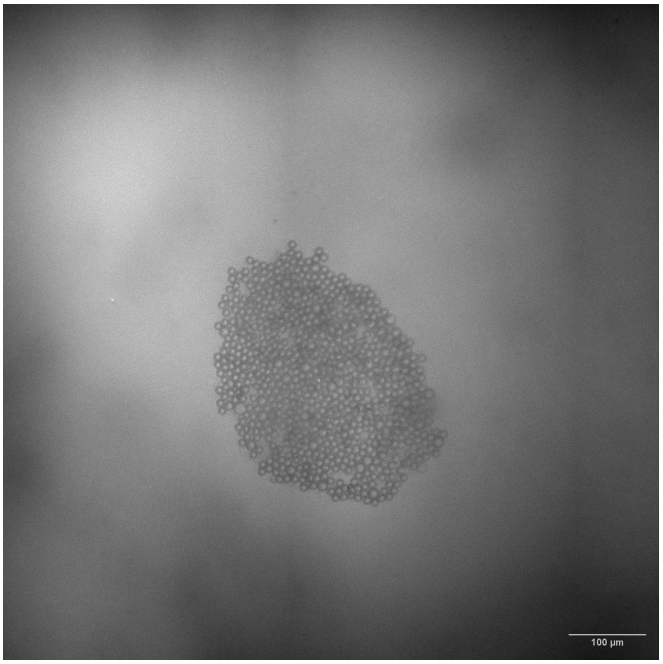

Figure 4.19: A trapped cluster of microspheres as viewed in brightfield microscopy.

4.6.4. Actuation Circuitry

The piezo transducer was actuated by a harmonic signal with a predefined frequency and amplitude with an electrical circuit as shown in Figure 4.20. The Keysight 33600A Waveform Generator was used to generate the harmonic waveform, which was then amplified with the Analog Devices AD8476 (non-inverting gain 4). The amplifier was powered by a Rigol DP832A dual mode power supply . The output waveform of the amplifier was then fed to the piezo transducer electrodes as shown in Figure 4.20.

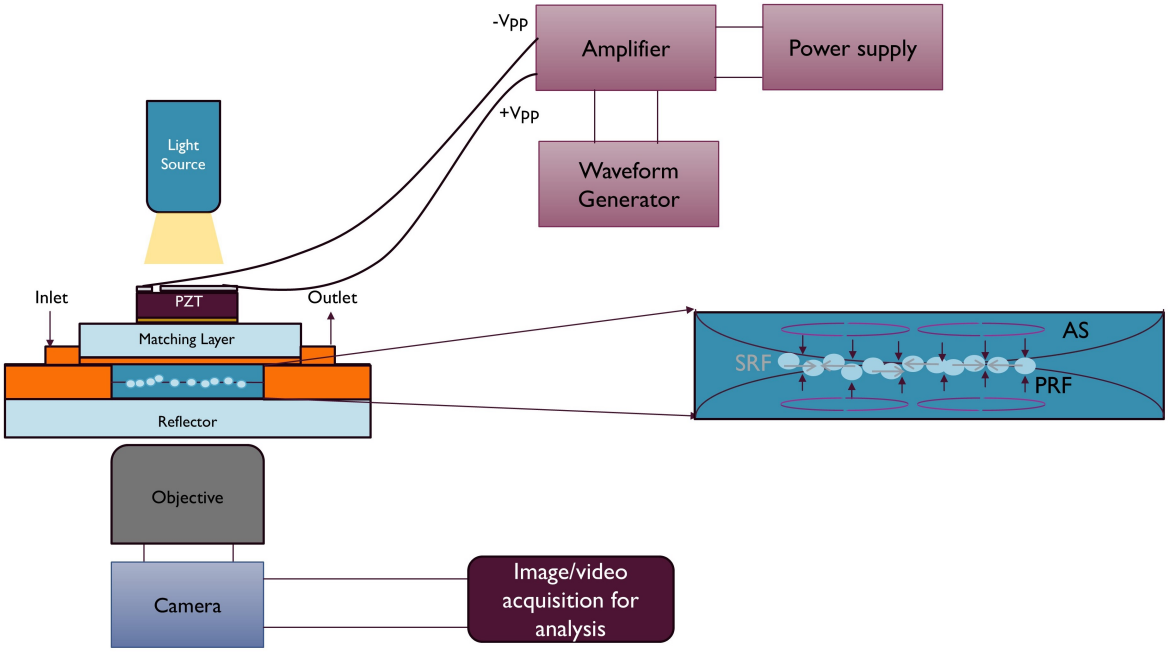

Figure 4.20: The experimental setup including acoustic actuation circuitry and imaging setups.

4.6.5. Image Analysis: ImageJ2 + MATLAB

Image analysis played an important part in the project, which was partly performed using FIJI/ImageJ2, and partly using MATLAB. ImageJ was used to visualize the images due to its compatibility with 16-bit images. The plugins *3D particle viewer* and *particle analyzer* were used for analysis and tracking purposes, to track particles over video frames and quantify particle density-dependent effects based on particle counts. In MATLAB, the image processing toolbox was used for template matching using *normalized cross-correlation* to estimate the trap stiffness. Details of the image analysis have been provided in Chapter 5.

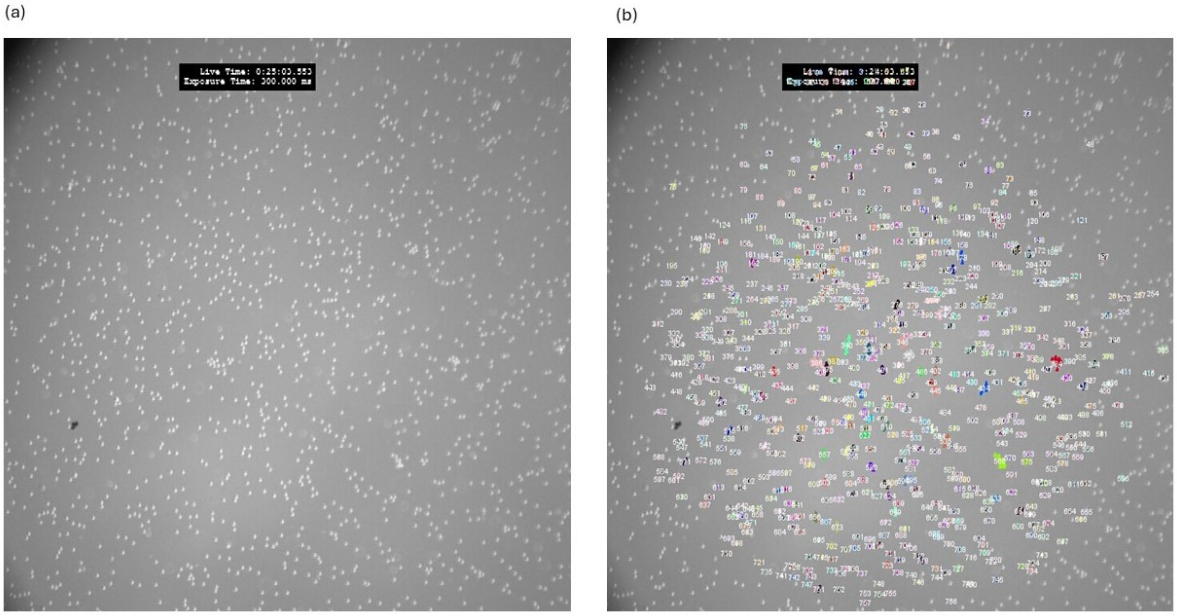

Figure 4.21: Example of Particle Detection Map extracted in ImageJ using the particle analyzer.

4.6.6. White Light Interferometry

Topography analysis was carried out for estimating the PDMS thickness, and for characterizing the 3D printed microscope calibration sample (a supplementary step illustrated in Appendix A). This was carried out using the Bruker White Light Interferometry setup. White light interferometry works by splitting a light beam into a reference and measurement arm, and superposing them to obtain a fringed pattern (interference) which then contains information about the surface topography. This principle is illustrated in Figure 4.22.

In order to ensure a good reflection and resulting strong interference, the surfaces were sputtered with a few nanometers thick layer of gold. Gold sputtering was carried out using the JEOL JFC-1300 Auto Sputter Coater, with a current of 20 mA for 30 seconds. Figure 4.25 shows an example measurement of the topography of the 3D printed sample by White Light Interferometry.

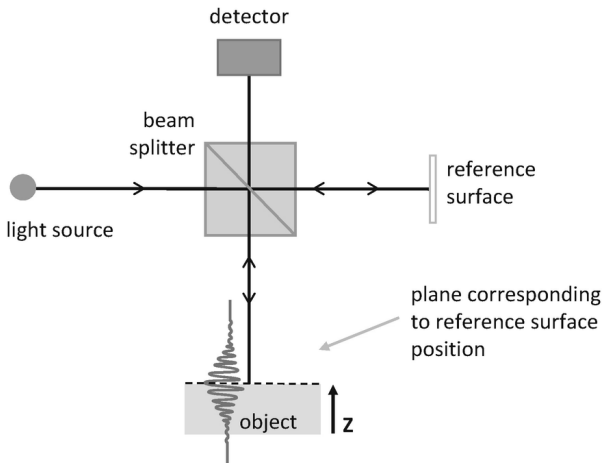

Figure 4.22: The White Light Interferometry principle.

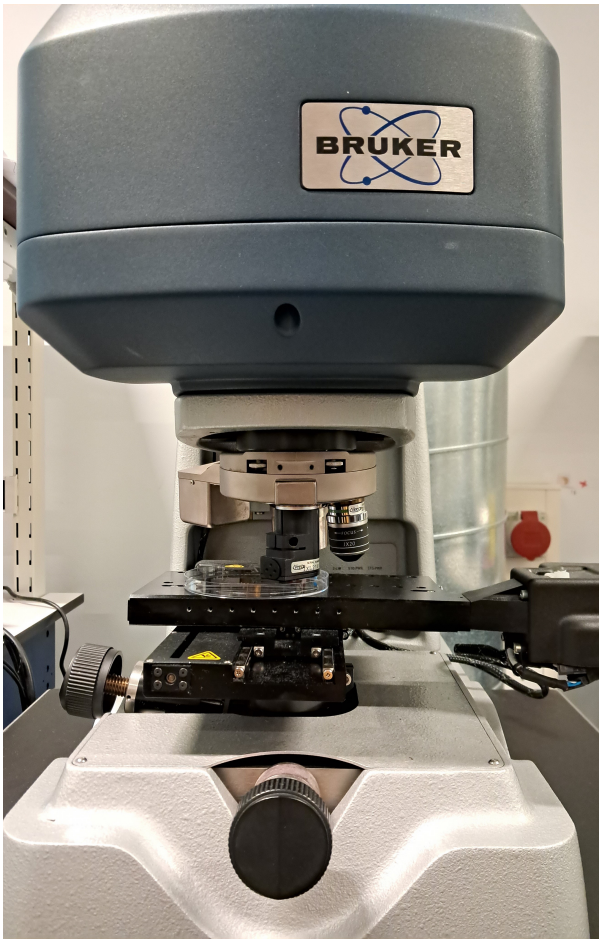

Figure 4.23: The Bruker setup to carry out WLI.

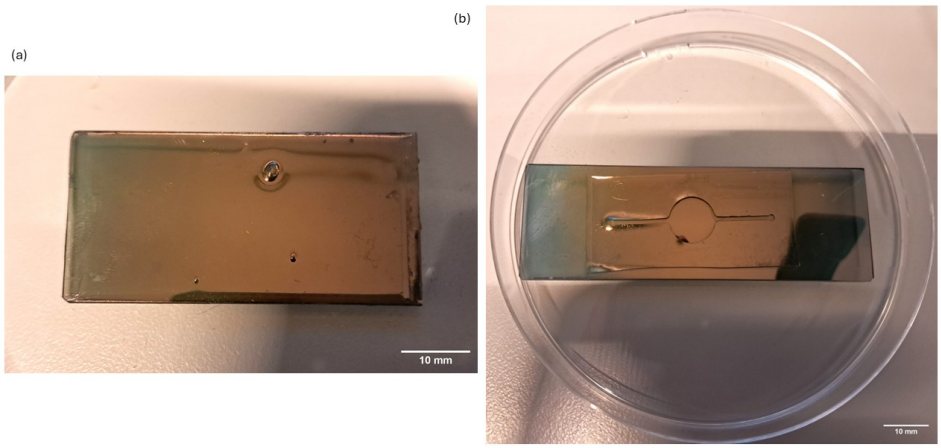

Figure 4.24: Gold sputtered spin-coated PDMS layer (a) and PDMS channel layer (b) for WLI.

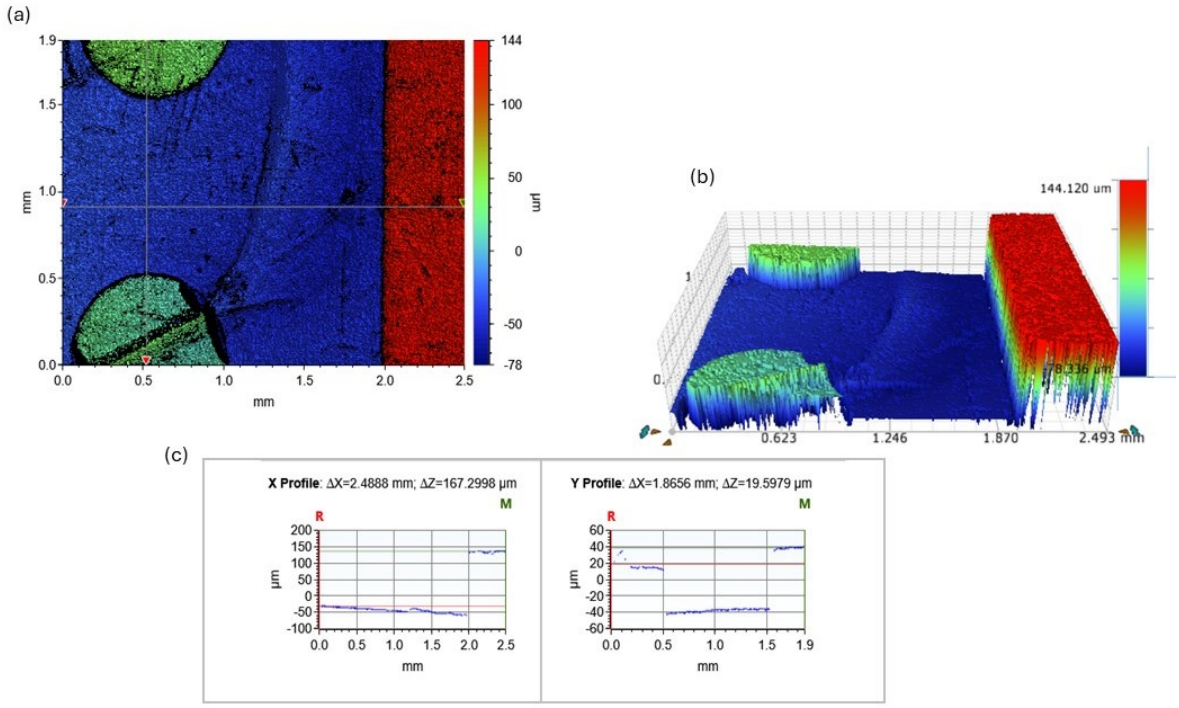

Figure 4.25: Characterizing a 3D printed test sample on the Bruker White Light Interferometer; (a) depicts the top-view and the cut-lines at which the profiles in (c) are plotted, (b) depicts the 3D topography view.

4.6.7. Electrical Resonance by Frequency Response Analyzer

A Frequency response analyzer (FRA) in the Moku-Go setup was used to estimate the electrical resonance of the piezo transducer. The circuit diagram of the same is shown below in Figure 4.26. The measurement was carried out as a single port measurement and the frequency response analyzer displayed the power in dBm. The frequency at which the line power measured experiences a dip can be interpreted to be the electrical resonance of the transducer, meaning that the transducer maximally absorbs energy at this frequency and converts electrical energy into mechanical energy (vibrations) most effectively at this frequency.

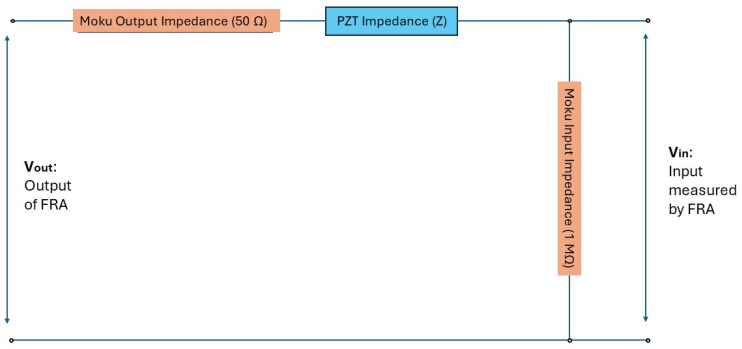

Figure 4.26: Single Port Measurement for Piezo Transducer electrical characteristics : Representative Circuit.

4.7. Summary

This chapter covered the materials, design principles, analysis tools, and fabrication methods involved that have been a crucial part of the thesis. It provided an overview of both the experimental and fabrication methods employed, as well as the computational tools used to complement the research, an overview of which is presented in Figure 4.27. With this background and set of tools at hand, the next chapter discusses the outcome of each of the methods discussed herein.

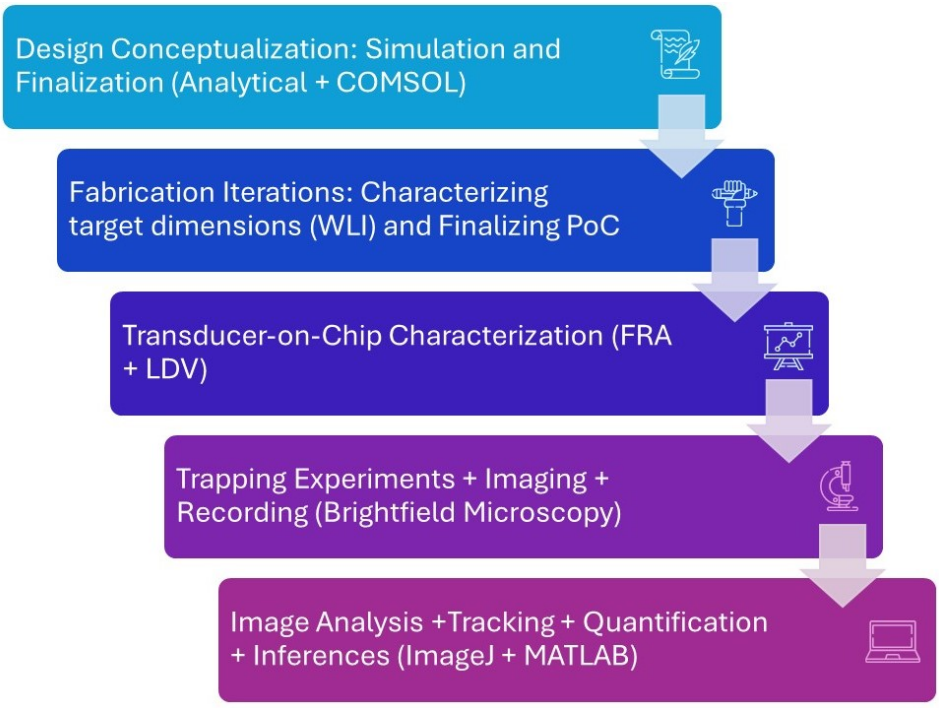

Figure 4.27: Summary of the methodological steps and associated tools+techniques in the project.

5

Results and Discussion

This chapter links the fabrication processes, methods, and characterization tools described previously to the outcomes of each of the processes and presents the experimental and computational results. The results have been discussed with their technical aspects alongside the presentation of the same, however, the application-oriented discussion and relevance study has been carried out in Chapter 6.

5.1. Fabrication Results

The device fabrication process consists of a series of manual steps, which brings in multiple junctures where the device needs to be tested to assess the quality of the fabrication step. Herein, the important step in the process is the generation of the PDMS spacer layer which comprises the fluid cavity to set up the acoustic resonance. The recipe to obtain the optimal PDMS thickness from spin-coating was tested. The PDMS thickness from both these processes was determined by White-Light Interferometry. In order to estimate the thicknesses, a gold layer was sputtered on the PDMS and glass surfaces, rendering them reflective. Figure 4.24 shows a PDMS spacer layer bonded to glass and sputtered with gold for the interferometry measurement. Figure 5.1 shows the outcome of the measurement in the form of a surface topography plot, which reads the thickness of the layer as $\sim$ 500 μm. The fabrication process resulted in a range of PDMS spacer layer thicknesses as depicted in Figure 5.2. The layers with measured thicknesses between 400 μm and 550 μm were taken to the next fabrication step whereas the others were discarded. Thus, the part of the fabrication workflow consisting of getting the acceptable thicknesses followed by consistent plasma bonding to yield a completely functional device required several fabrication iterations and constituted a significant amount of the project time.

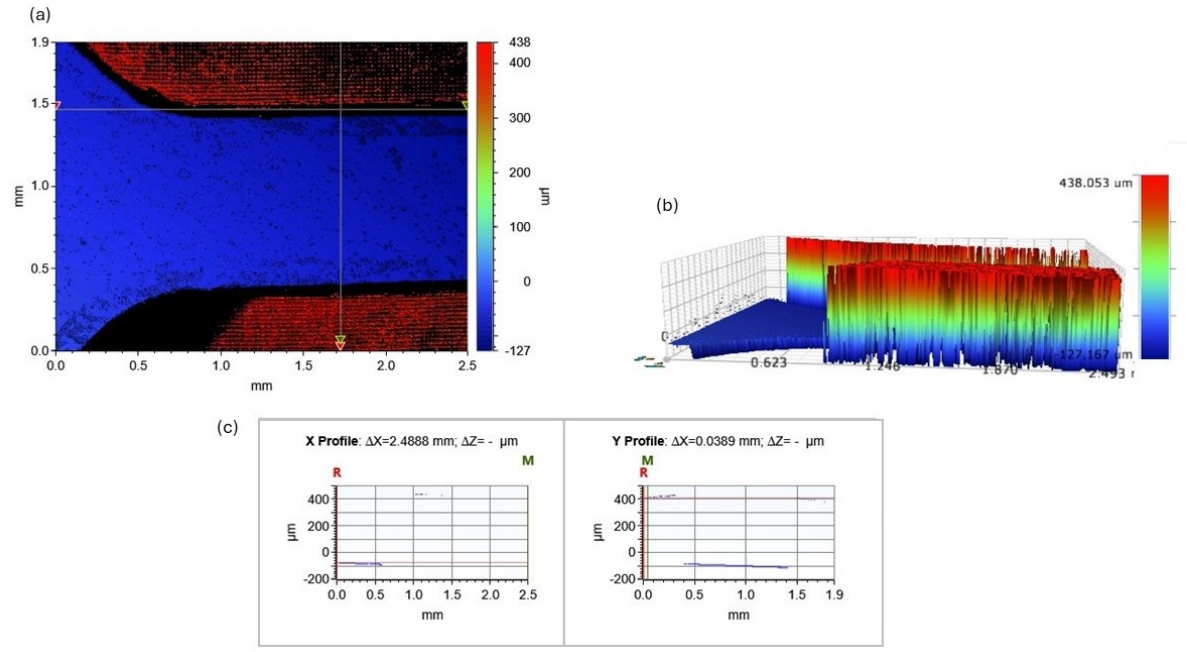

Figure 5.1: Molded PDMS thickness measurement by WLI; (a) depicts the top-view and the cut-lines at which the profiles in (c) are plotted, (b) depicts the 3D topography view.

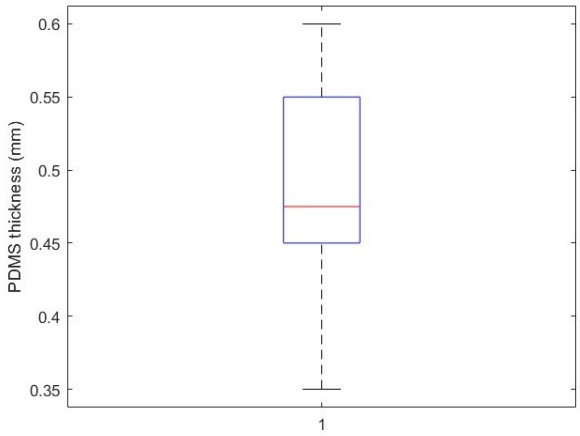

Figure 5.2: PDMS thickness variation across demolded membranes.

A similar process was adopted to estimate the thickness of the spin-coated PDMS. Figure 4.24 depicts a spin-coated, sputtered sample ready for interferometry measurements. Figure 5.3 shows the estimate of the PDMS thickness ($\sim 80\mu$m) obtained by a spin-coating cycle of 5 min at 500 rpm. This value lies in the target range specified in Chapter 4.

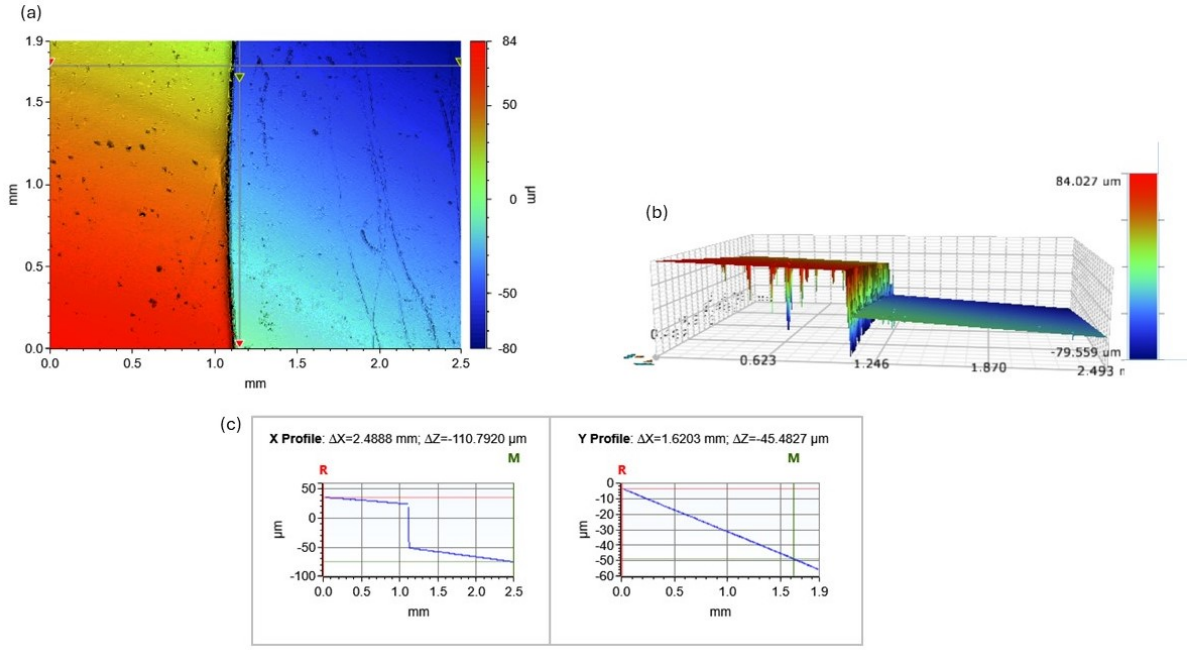

Figure 5.3: Spincoated PDMS thickness measurement by WLI; (a) depicts the top-view and the cut-lines at which the profiles in (c) are plotted, (b) depicts the 3D topography view.

The fluid channel height (and thus, in turn, the resulting PDMS spacer layer thickness after completion of the stack assembly) was also estimated by brightfield microscopy. This was calculated based on the focal plane of the beads stuck to the surface of glass (bottom of fluid chamber) and the beads stuck to the PDMS layer (top of fluid chamber) as shown in Figure 5.4. The final functional resonator prototype after completion of the fabrication resulted in a fluid layer thickness of 450 $\pm$ 10 μm as compared to 520 μm (from design).

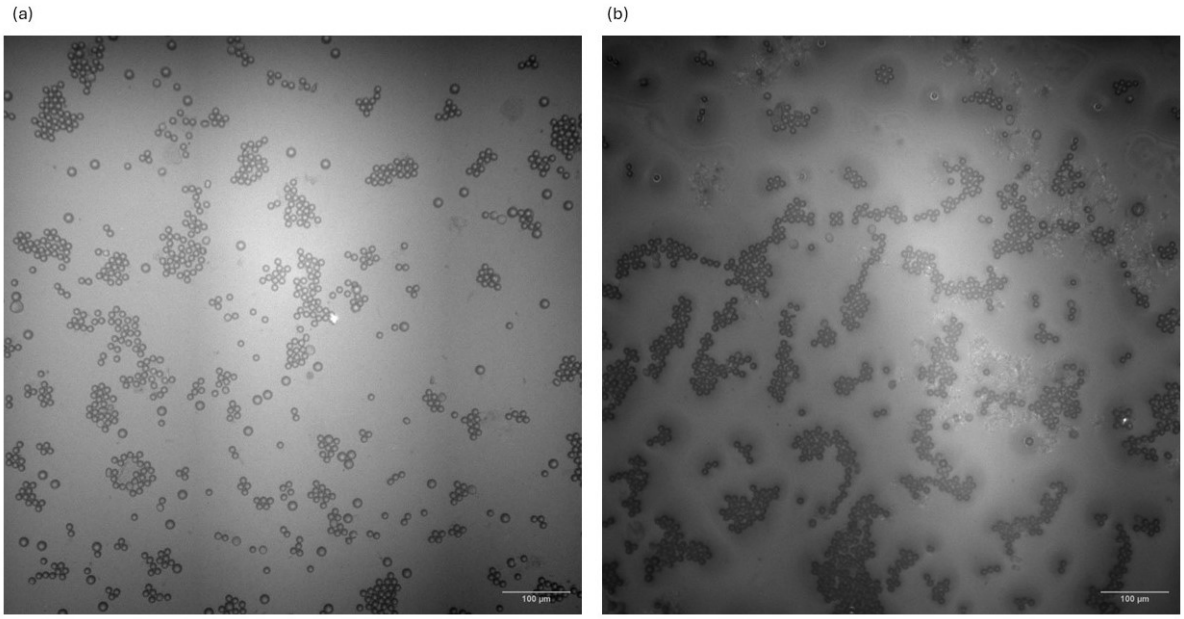

Figure 5.4: Determining Focal Plane of beads, (a) Beads on the base of the fluid channel, (b) Beads on PDMS layer at top of the fluid channel.

5.2. Transducer-on-Chip Characterization

The acoustic actuation in the device is carried out by a piezoelectric transducer attached to the completed stack. The piezoelectric transducers are manufactured by Physik Instrumente as standard catalog products with design parameters pre-defined.

The PZT used herein has a thickness resonance frequency spectrum centered at 2.1 MHz. In order to estimate the impact of the attachment of the transducer to the acoustofluidic chip on the resonance behavior of the transducer, the system was characterized electrically and mechanically in a transducer-on-chip configuration.

The electrical response analysis of the transducer-on-chip was carried out by the Moku-Go Frequency Response Analyzer (representative circuit diagram in Figure 4.26) by observing the signal strength (in dBm) at the PZT terminals over a range of harmonic actuation frequencies. The mechanical response of the transducer-on-chip was estimated by a Laser Doppler Vibrometer by recording the vibration velocity spectrum over 12 locations on the transducer surface, and calculating the average spectrum from these measurements. 12 different sample locations were chosen as the reflection from the surface was not uniformly strong enough to obtain reliable data, which led to the use of this method of calculating the average spectrum over multiple locations. These two methods are depicted schematically in Figure 5.5.

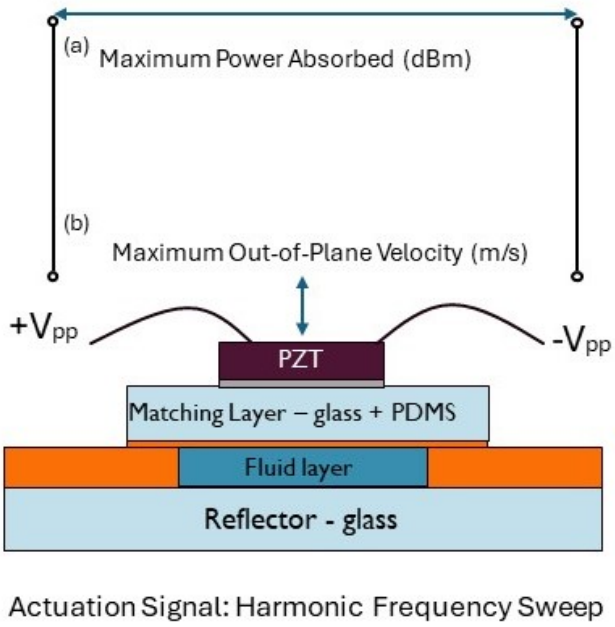

Figure 5.5: Characterization methods for Transducer-on-Chip Resonance: (a) Electrical Resonance estimation by power absorbed, (b) Mechanical Resonance estimation by out-of-plane vibration measurements.

The electrical frequency response spectrum is depicted in Figure 5.6. It can be observed that the signal strength (power) dips sharply close to 2.1 MHz, which indicates the frequency at which maximum absorption of power by the transducer takes place, and in turn, a maximal conversion from electrical to mechanical energy occurs. The frequency corresponding to this power minimum closely resembles the design resonance frequency in thickness expansion mode. There are secondary dips observed at frequencies lower than the design resonance as well, however, those are not as prominent as the global resonance at 2.1 MHz. The interesting finding herein is that the mechanical loading of the chip, thus, does not heavily impact the electrical resonance characteristics. This can be attributed to a low electromechanical coupling between the transducer and the chip [94].

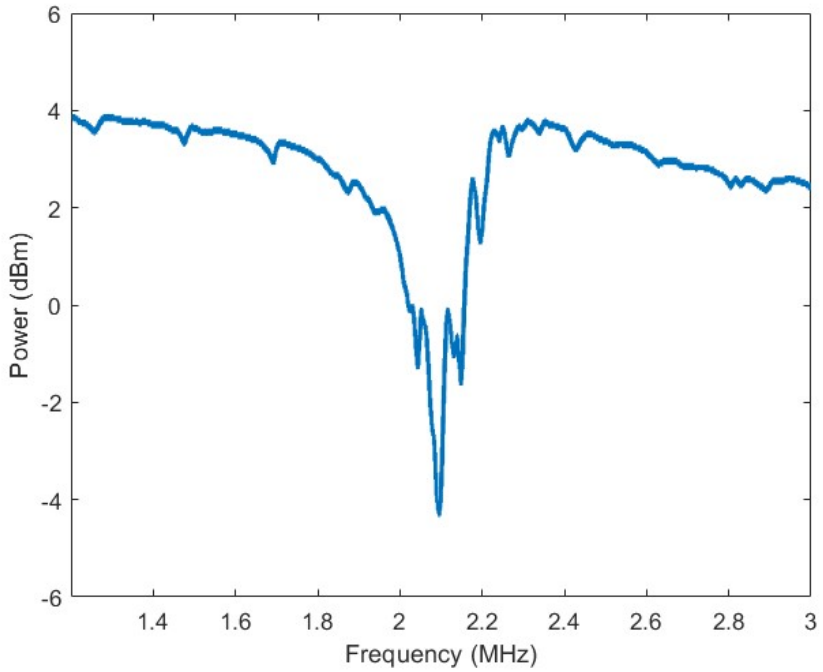

Figure 5.6: Electrical Resonance Estimation by Frequency Response Analyzer.

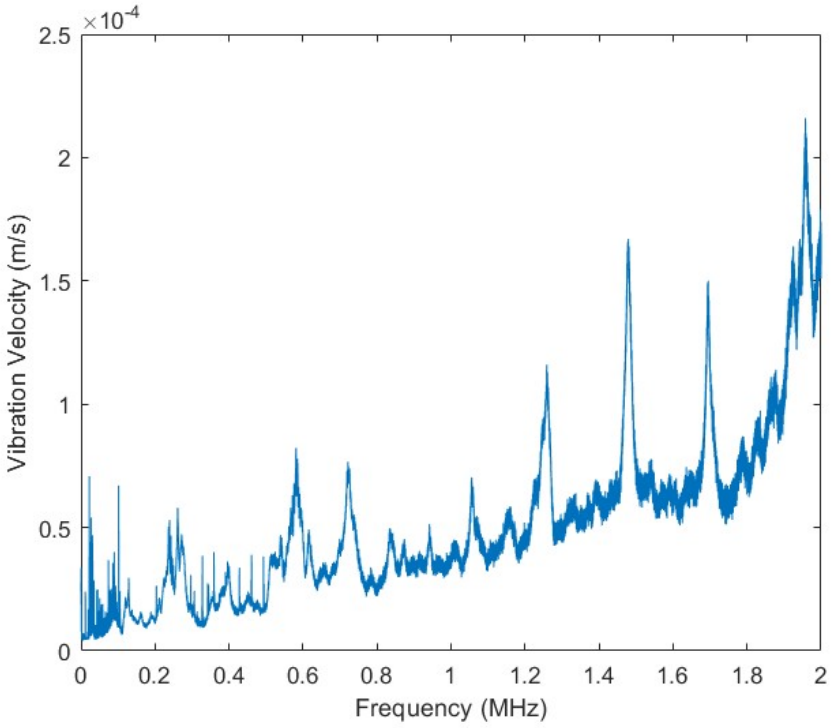

Figure 5.7: Mechanical Response Frequency Spectrum by Laser Doppler Vibrometry.

The mechanical frequency response spectrum is depicted in Figure 5.7. The Polytec MSA-400 Laser Doppler Vibrometer system has a limited recording bandwidth of up to 2 MHz, hence only the

spectrum up to 2 MHz was recorded. It can be observed that there is an expected spectrum peak around 2 MHz, close to the electrical resonance. However, secondary peaks are observed at lower frequencies, this can be attributed to the mechanical loading of the transducer when attached to the chip, the mechanical coupling of the transducer and the glass chip, and the damping in the transducer and the chip, which is not completely replicable in simulations. The mechanical loading and damping result in secondary resonances that are challenging to match with the functional operating frequencies of the device by design [94]. The secondary peaks, however, occur around the same frequencies as the minor secondaries that were observed in the electrical response (Figure 5.6). The point of interest, however, is that the operating range of the chip is an acceptable operating frequency for the transducer as the pressure amplitude obtained is sufficient to trap particles in experiments.

5.3. Trapping Characterization

5.3.1. Height of the Trap

The preliminary study in this work begins with the characterization of the 1-D particle trap that is created by setting up a standing wave in the z-direction in the layered resonator. The fabrication results indicate a possibility of tolerances leading to varied/imperfect thicknesses of the fluid layer. Hence, the first step in characterizing a newly fabricated device was to experimentally determine the bandwidth and optimal performance frequencies. Building over the basics of a layered resonator structure and the materials that have been employed in the device, it was anticipated that the resonator could have a wider bandwidth [87]. This was determined experimentally. Levitation was observed (particles were confined in a single plane trap) starting at a frequency of 1.4 MHz up to a frequency of 1.7 MHz (bandwidth of 300 kHz). The particles did not levitate consistently into single planes outside of this frequency range. Figure 5.8 schematically depicts the determination of the trapping plane height, measured from the base of the fluid channel (or the reflector boundary).

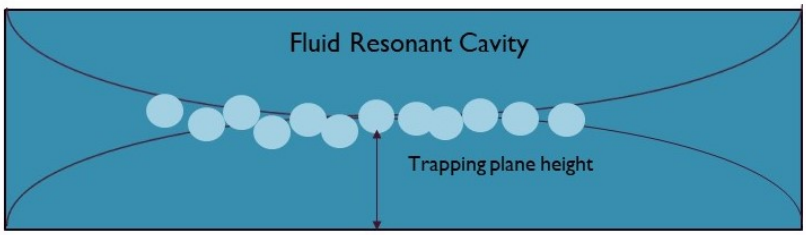

Figure 5.8: Schematic of Trapping Plane Height Measurement.

The trap height was estimated by finding the focal plane of the trapped particles after acoustic actuation. The observed trapping plane heights derived from microscopy were as shown in Figure 5.9.

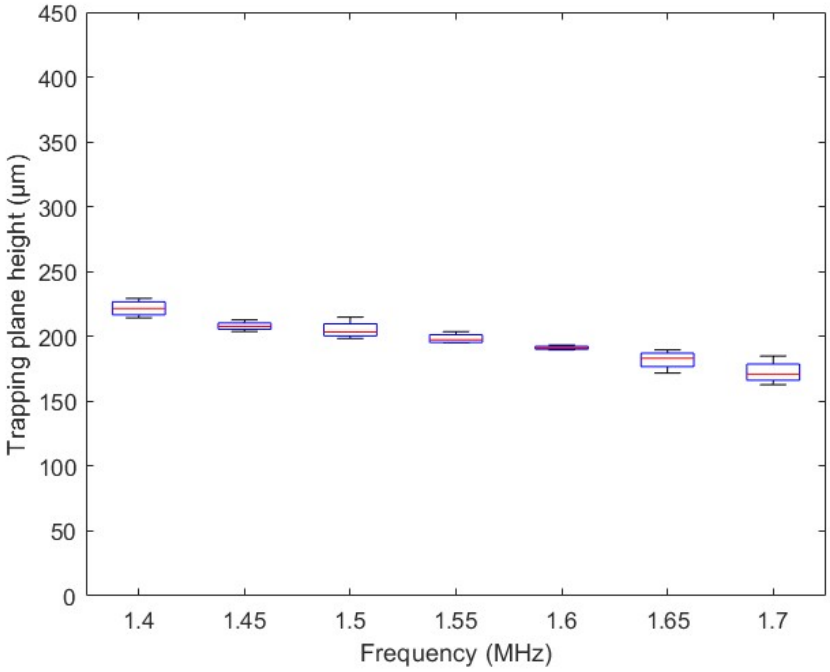

Figure 5.9: Experimentally Determining Bandwidth and Resonance.

Figure 5.9 depicts a shift in the trap towards the reflector boundary as the frequency is increased within the bandwidth. This can be explained by the near-perfect reflection at the water-glass interface. The reflection interface between water ($Z_{acoustic}$ = $1.48MRayl$) and glass ($Z_{acoustic}$ = $14.12MRayl$) acts similar to the fixed end, which means that the interface behaves like a pressure-antinode. This creates a trap that is pushed *towards* the reflector for frequencies higher than the fundamental resonance, and a trap that is used *away* from the reflector for frequencies lower than the fundamental resonance. This effect is depicted diagrammatically in Figure 5.10. The phenomenon can also be simulated in COMSOL and yields a similar trend as shown in Figure 5.11. This also brings in the conclusion that the trap location can be controlled to some extent in a specific bandwidth.

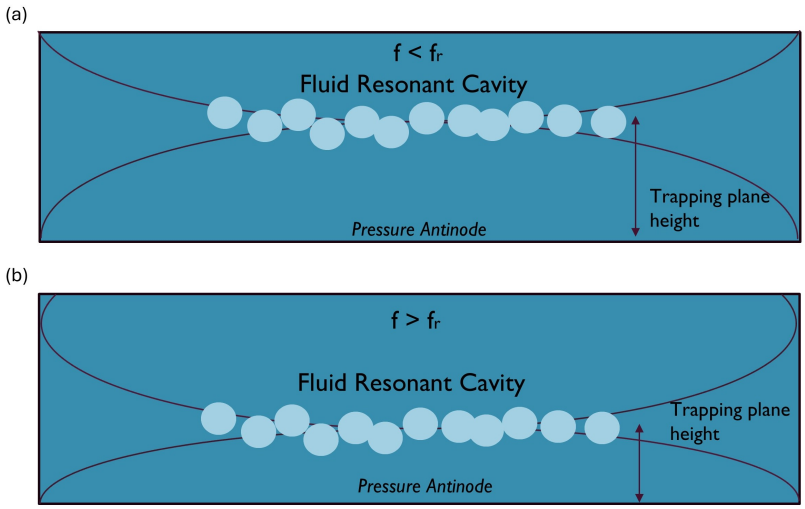

Figure 5.10: Impact of frequency on trap location: (a) Shifting of trap away from reflector layer below resonance, (b) Shifting of trap towards reflector layer above resonance.

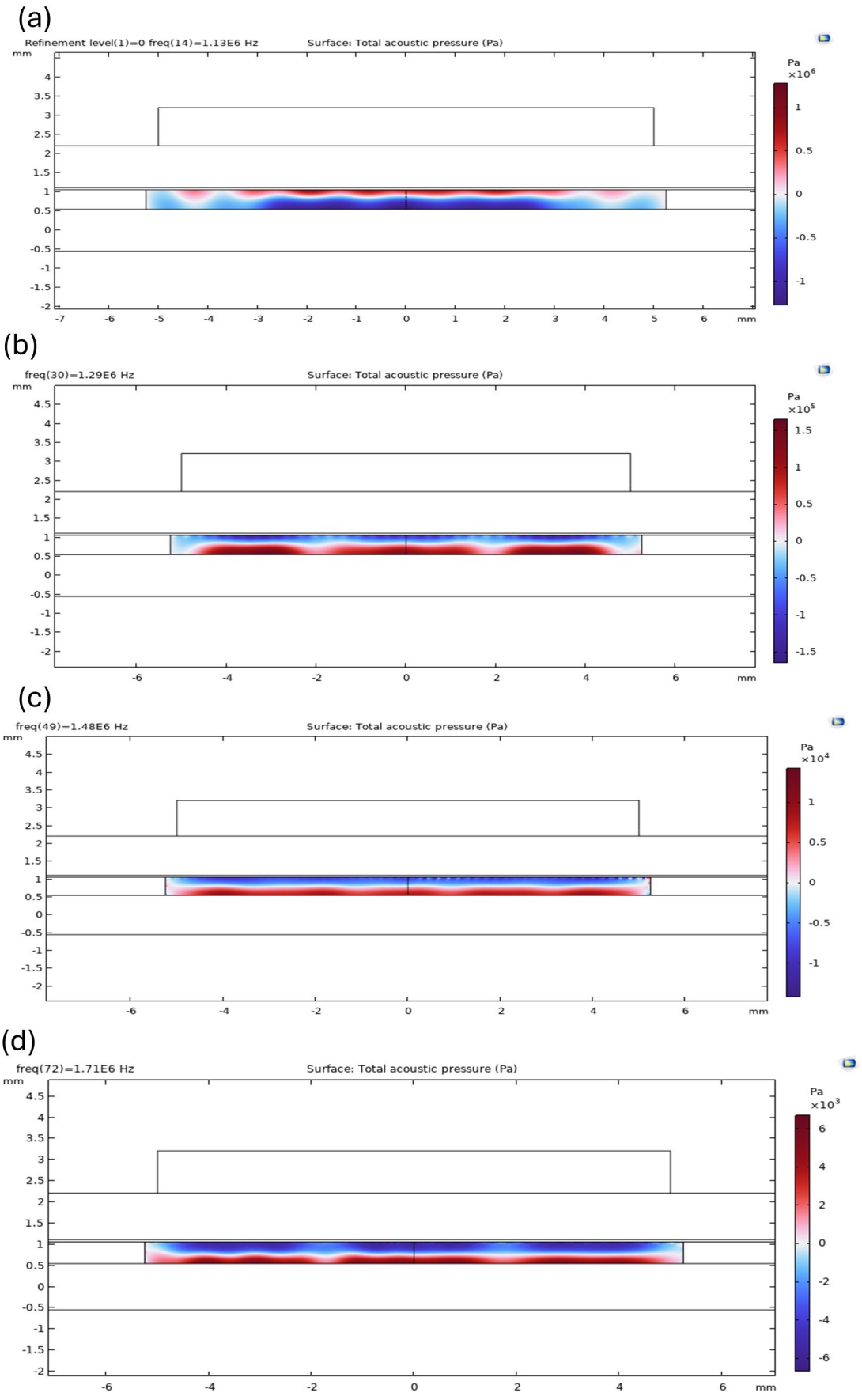

Figure 5.11: Simulating plane shift in COMSOL. At 1.48 MHz, the trapping plane lies close to the middle of the fluid channel height. It is pushed towards the reflector beyond 1.48 MHz, and away from the reflector below 1.48 MHz.

5.3.2. Trapping Response Time

In order to estimate the impact of the input energy (transducer driving voltage) and its association with the trapping response time, videos were acquired at 20 fps with different input voltages, and multiple runs of experiments were carried out for the same. Further processing was carried out by the Manual Tracking plugin in ImageJ2. The response time, ideally, is the time taken for a particle to travel from the base of the fluid channel (where it is settled) to the plane of the trap. This, however, is not compatible with image analysis, as the particle is not detectable by the software throughout its travel of $\sim$ 200-250 μm due to the limited working distance of the microscope objective. Hence, two alternative strategies for recording the trapping time were devised, as depicted in Figure 5.12. In strategy (a), the microscope is focused on the base of the fluid channel, tracks are created, and the timestamp at which the track disappears is recorded. In strategy (b), the microscope is focused at the approximately known nodal plane, and the timestamp at which the particle is detected by the tracker is recorded. To put forth the final results, strategy (b) was selected over (a) as it more accurately depicted the time from actuation to trapping, and also minimized noise from extra particles at the channel base.

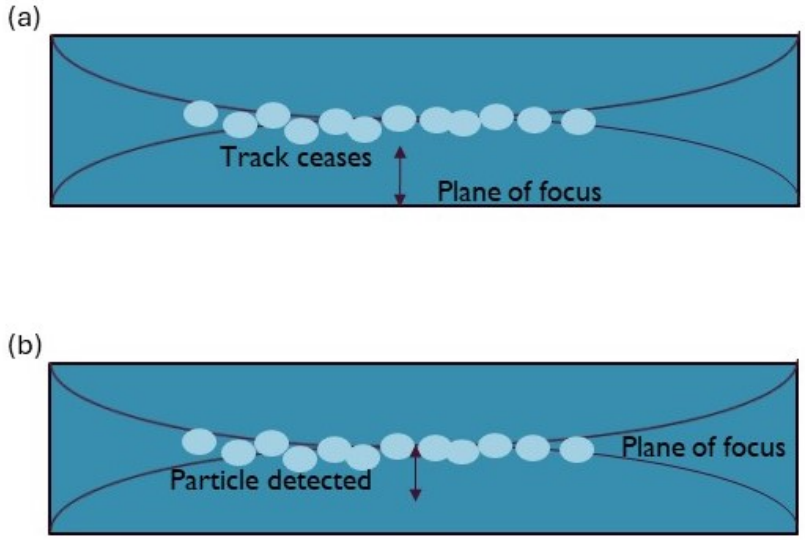

Figure 5.12: Methods of determining response time by particle tracking: (a) Microscope focused at channel base, (b) Microscope focused at the trapping plane.

In addition to the experiments, an analytical viewpoint was taken into consideration to qualitatively depict this trapping time. Herein, the force balance on a particle travelling in z-direction in a standing wave pressure field is looked at. Neglecting inertial effects leaves a force balance between the Acoustic Radiation Force (F_{rad}) and the Drag Force (F_{drag}) as follows, similar to the analysis presented by [95]:

$$F_{drag} = F_{rad} \tag{5.1}$$

which yields,

$$6\pi\eta a v_p = 4\pi\phi k a^3 E_{ac} sin(2kz) \tag{5.2}$$

This results in the below expression:

$$v_p = \frac{2}{3}\phi\frac{ka^2}{\eta}E_{ac}sin(2kz) \tag{5.3}$$

Substituting $v_p = \frac{dz}{dt}$ yields:

$$\frac{dz}{sin(2kz)} = \frac{2}{3}\phi\frac{ka^2}{\eta}E_{ac}dt \tag{5.4}$$

Integrating between limits $z = z_0$ to z_f and $t = 0$ to t_f yields,

$$tan(kz_f) = tan(kz_0)e^{\frac{4}{3}\phi\frac{k^2a^2}{\eta}E_{ac}t_f} \tag{5.5}$$

Rearranging the terms yields the following relation:

$$t_f = \frac{3\eta}{4\phi k^2 a^2 E_{ac}} ln(\frac{tan(kz_f)}{tan(kz_i)}) \tag{5.6}$$

Further, the Energy Density E_{ac} in the fluid cavity is related to the pressure amplitude (P_a) and input voltage (V_i) as [96]:

$$E_{ac} \quad \alpha \quad {P_a}^2 \quad \alpha \quad {V_i}^2 \tag{5.7}$$

Which, based on Eq. 5.6 and 5.7, finally results in a relation of form,

$$t_f \quad \alpha \quad \frac{1}{V_i^2} \tag{5.8}$$

Within experimental limits, the obtained trapping response data can be fitted to the expected analytical relation as shown in Figure 5.13.

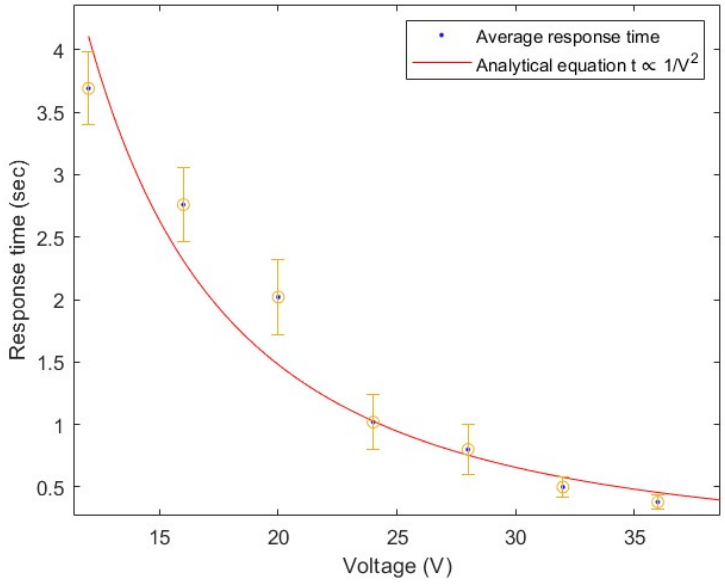

Figure 5.13: Fitting the analytical model to response time data obtained from image processing.

5.3.3. Force Interplay and Trapping Efficiency

An acoustic wave propagating in a fluid gives rise to primarily two prominent effects, namely, the second-order time averaged *Acoustic Radiation Force* on the particles in the path of the wave, and *Streaming*, the flow of the fluid resulting from attenuation of the acoustic wave. Broadly, the Acoustic

Radiation Force scales with the particle volume, and thus dominates for larger particle sizes, whereas the Streaming-induced Drag Force scales with the particle radius and thus dominates for smaller particle sizes. The system of a standing wave in an acoustofluidic cavity comprises of both these effects together, and there exists an interplay between them [97]. A similar situation was observed in the chip fabricated in this work. Figure 5.14 depicts the prominent effects observed in this system.

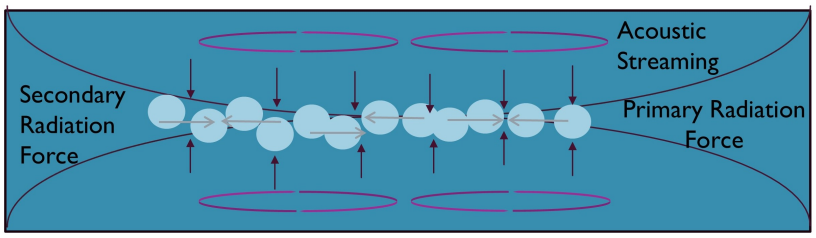

Figure 5.14: Force interplay in the system depicting the competing effects, namely the PRF, SRF, and Streaming.

For the device dimensions and working frequencies under consideration, it was evident that the boundary layer thickness was of the order of 1 μm, which indicates that the streaming observed in the device can be attributed to Rayleigh (outer bulk) Streaming. Thus, the key interplay in the device is between the bulk streaming and the acoustic radiation force. The particle sizes under consideration ($\sim$ 10 μm), though large enough for levitation by the Primary Radiation force, also show vortex motions under streaming drag. Similar effects in particle sizes under consideration have been observed in previous works too [83].

Building on this, it can be said that, theoretically, the forces acting on the particles in the acoustic field are the Primary Radiation Force (PRF) acting parallel to the wave propagation direction, the Secondary Radiation Force (SRF) acting perpendicular to the wave propagation direction, and the Streaming-based Drag Force responsible for the bulk motion of the particles. However, when it comes to a practical device, there is an additional transversal component of the PRF that comes into play owing to the fabrication imperfections. This is a result of the fact that the reflector and matching layer boundaries could be slightly non-parallel, resulting in a transversal component of the PRF (perpendicular to the wave propagation direction). As the standing wave is created only in the axial (Z-direction), the axial component of the PRF is zero at the nodal plane, however, the resulting transversal components could remain slightly non-zero. This adds to the in-plane effects resulting from Rayleigh streaming and the SRF. Figure 5.15 and 5.16 depict the forces in a practical acoustic resonator like the one in this work.

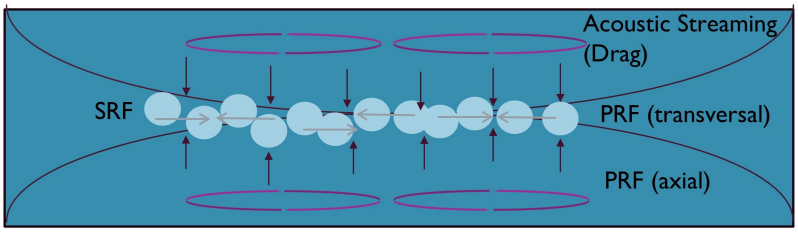

Figure 5.15: The force interplay scenario in a practical acoustic resonator.

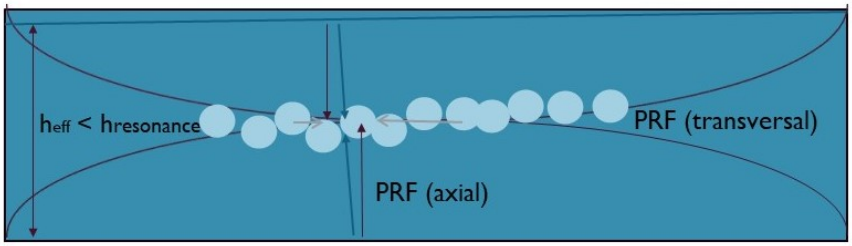

Figure 5.16: The transversal component (unbalanced) of the PRF resulting from geometrical imperfections.

The origin of these imperfections can be illustrated from the PDMS thickness measurements by White Light Interferometry in Figures 5.1 and 5.17. The figures show the height maps of two different sections of the same PDMS layer, which show a slight variation in measured PDMS thicknesses. This depicts how the fabrication imperfection can cause the transversal PRF components in a real device. Second to this, the height imperfection also has an impact on the optimal operating frequency of the device. It can be seen from Figure 5.16 that the effective cavity heights can be different from the optimal design height, which implies that a uniform resonance cannot be achieved at a single frequency. The scheme to overcome this limitation and its impact has been described in the next section.

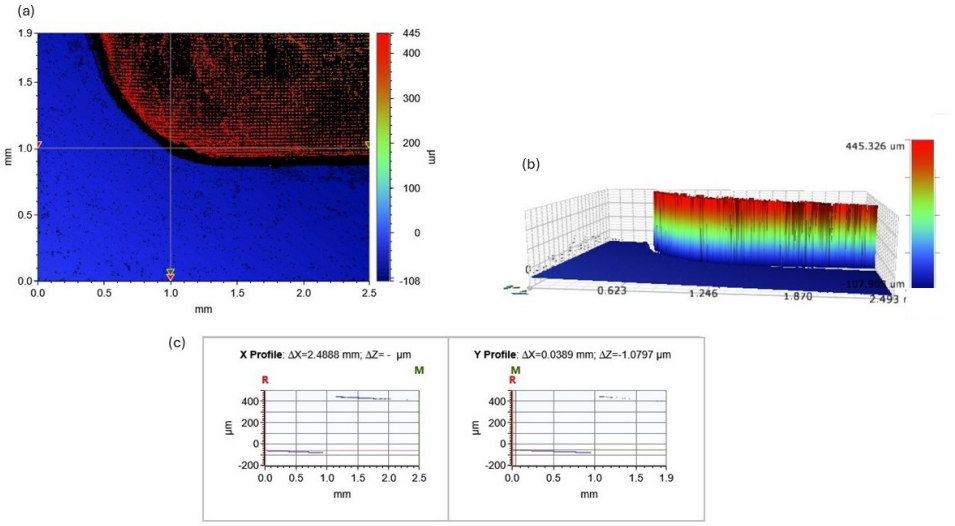

Figure 5.17: The deviation in PDMS layer thickness as compared to 5.1.

When the acoustic field is turned on in the device, the particles respond within seconds to the acoustic wavefield. Herein, it was observed that the PRF traps the particles in the nodal plane, which can be observed by the particles in the microscopic view going out-of-focus and gradually disappearing from the view of the base of the fluid chamber (video links to demonstrate this in the Appendix C). However, some of the particles in the base field of view follow the fluid vortices induced by streaming, while a few do not move (owing to inconsistencies in the standing field, or adhesion to the reflector surface). Thus, it was anticipated that this occurs partly due to streaming and partly due to field inconsistencies. Considering the focal plane set at the base of the fluid well, the trapping efficiency is defined as:

$$\eta_{trapping} = \frac{N(0) - N(60)}{N(0)} \tag{5.9}$$

where, N(t) is the number of particles in frame at time t.

This was carried out by the particle analyzer plugin in ImageJ2. The images were first converted to 8-bit format followed by thresholding. Further, the particle counter was set to count particles in a video time-stack with pixel radii of 5 to 15 pixels. The particle number was recorded before and after levitation, and the efficiency was calculated by the above mentioned formula. However, to eliminate bias due to the number of particles stuck to the base of the channel, this number was estimated by imaging the base after flushing the channel and was subtracted from the particle count after levitation.

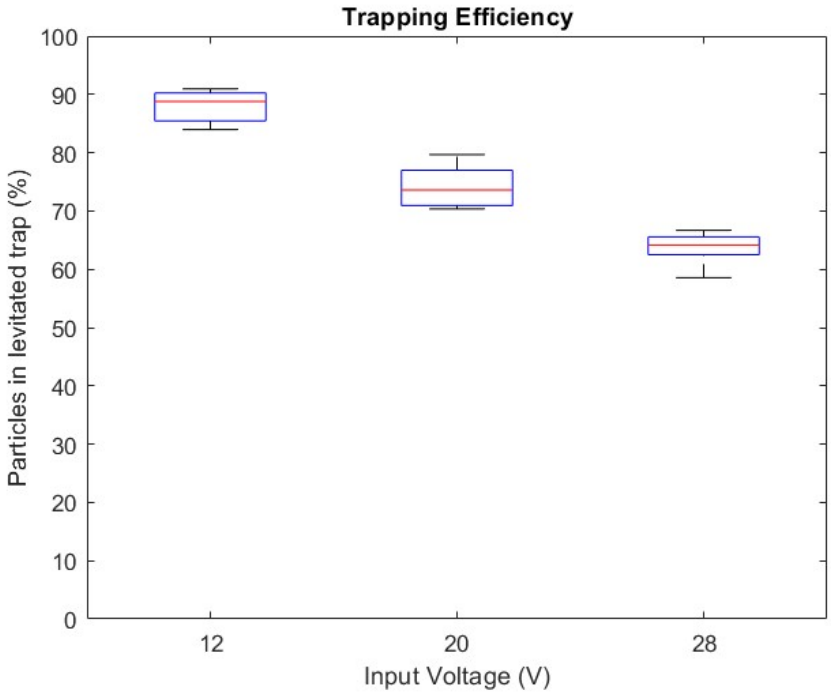

Figure 5.18: Extent of Levitation (Trapping efficiency) variation with Input Energy.

Figure 5.18 indicates that the extent of streaming is significantly reduced when the input energy is lower, and thus the attenuation is lower as well. Thus the trapping efficiency increases with a decrease in input voltage. However, the challenge arising from the inconsistency in the standing wave field still remains, which is solved as below.

In order to overcome the inconsistency in the standing wave field due to imperfections in the PDMS layer thickness leading to a low trap efficiency, a frequency sweep across the experimentally determined bandwidth was applied as an input waveform to the transducer instead of a single frequency. The applied frequency sweep was a linear sweep according to the relation:

$$f(t) = f_0 + st \tag{5.10}$$

where,
$f(t)$ is the frequency at time t
f_0 = 1.4 MHz, the start frequency
s = 0.002 s^{-1}, such that the frequency is swept from 1.4 MHz to 1.6 MHz in a sweep time of $100s$

The frequency sweep yields a higher trap efficiency as evident from Figure 5.19. This can be attributed to two effects:

- Firstly, the impact of inconsistencies in fluid layer thicknesses is reduced by creating a uniform resonance when the frequency is swept, rather than kept constant.

- Secondly, the frequency sweep creates a variable acoustic force field that varies as:
  $F_{rad}(z,t) = 4\pi\phi k(t)a^3 E_{ac} sin(2k(t)z)$

  Thus, the varying force field is able to dominate the drag force through the sweep and pull the particles out of the streaming vortex into the trap.

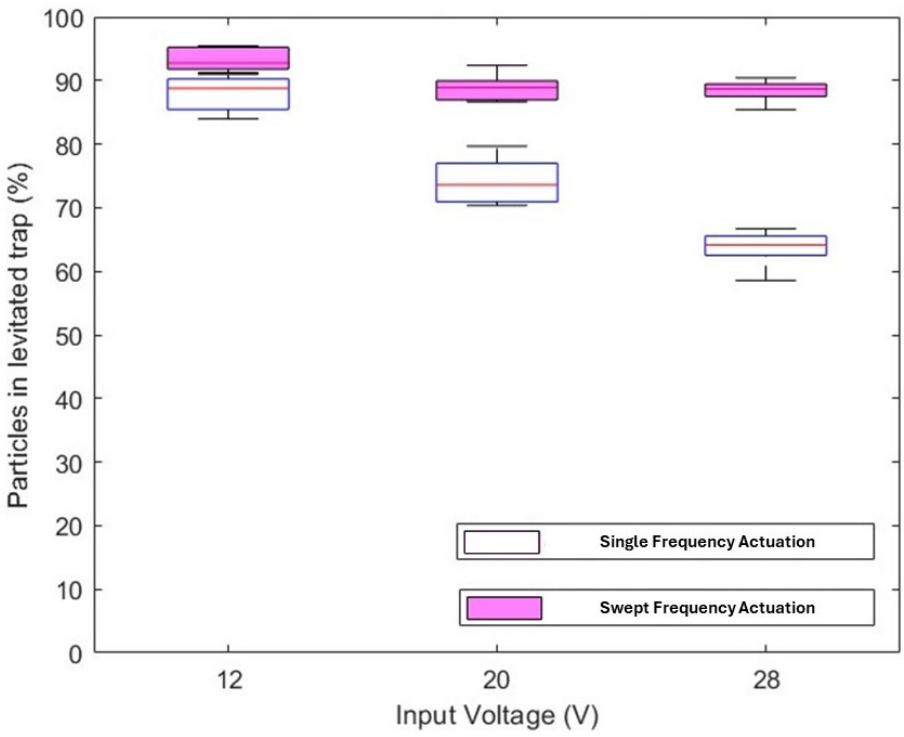

Figure 5.19: Improved Trapping Efficiency with a Multi-Frequency Actuation.

Thus, with an appropriate actuation scheme for the chip, it is concluded that the imperfections can be overcome and the trapping efficiency can be maximized.

5.3.4. Trap Stiffness Estimation

For a quantification of the acoustic radiation force on the particles trapped in the nodal plane, the term *Trap Stiffness* is often quoted [98]. The acoustic radiation force has a sinusoidal variation across the height of the fluid chamber and thus is approximated to be linear in the close vicinity of a pressure node. With this background, the trap can be interpreted similarly to a linear spring with spring constant k_a.

Trap stiffnesses in acoustic traps have been estimated by researchers in multiple ways such as the drag force method [99], or by a force balance against a pre-defined reference force entity [100]. Another well-suited method that has been used to quantify the performance of Optical as well as Acoustic traps is based on Equipartition Theory.

Equipartition Theory or the Law of Equipartition relates the temperature (and in turn, the thermodynamic energy) of an entity in thermal equilibrium to the average energies of each DoF (Degree of Freedom) of the entity. Thus, for translational motion, the sum of the energies in all 3 DoFs equals $\frac{3}{2}k_BT$, whereas the energy of each DoF equals $\frac{1}{2}k_BT$. Now, if the trap is approximated as a linear spring and the center of the trap as the equilibrium position, it yields the following:

$$\frac{1}{2}k_a{\sigma_z}^2 = \frac{1}{2}k_BT \tag{5.11}$$

where,
k_a is the acoustic trap stiffness
σ_z is the variance in the z-position of the particles as measured from the trap center (depicted in Figure 5.20)
k_B is the Boltzmann Constant
T is the absolute temperature in Kelvin

This method of estimation holds under the conditions that the z-position of the particles can be estimated accurately, and the particles are in thermal equilibrium. The accuracy in z-position was ensured by capturing microscopic image z-stacks with a z resolution of 0.1 μm with the automated stage of the microscope, whereas the thermal equilibrium was taken into consideration by conducting the experiments in a controlled room-temperature environment (298 K) and minimizing the actuation time to avoid heating of the chip.

Once the variance in z-position has been estimated, the trap stiffness can be calculated as below:

$$k_a = \frac{k_BT}{{\sigma_z}^2} \tag{5.12}$$

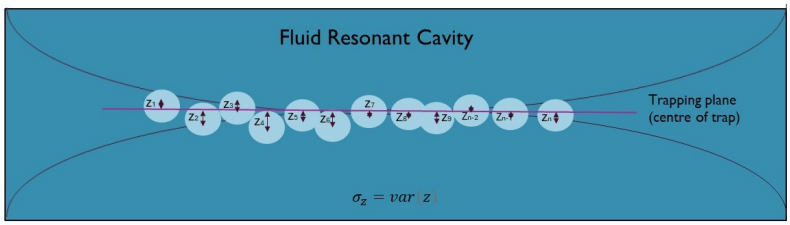

Figure 5.20: Stiffness estimation technique, depiction of measurement of z-positions from center of acoustic trap.

The estimation of z-position variance was carried out by template matching using MATLAB's Image Processing Toolbox. The code for the analysis has been attached in the Appendix B. The process consisted of the following steps:

- A z-stack of images of the nodal plane was recorded with a z-step of 0.1 μm.
- 50 reference images for sharply focused beads were obtained using the same microscopic settings to act as templates for template matching.
- Cross-correlation coefficients were calculated based on the formula described in the subsequent section among the permutations of the reference beads. Based on the average value of these coefficients, a threshold value was obtained.
- The reference templates were averaged to obtain a robust 'average' template.

- Template matching was carried out between each image of the z-stack and the reference bead templates. The number of instances wherein the correlation coefficient exceeded the set reference threshold was recorded.

- This resulted in a plot depicting the spread of the particles from their mean position (i.e. the nodal plane and the center of the trap). The variance of this position was calculated from the data obtained.

The template matching method employs the fast cross-correlation formula as outlined by [101] and is implemented in MATLAB. Herein, the intensity values are compared pixel-by-pixel by sweeping the template over the entire image (similar to a kernel) and summing up the product of the overlapping pixel intensities, followed by normalizing the result by the template sum. This is depicted in the below formula:

$$\gamma(u,v) = \frac{\Sigma_{x,y}[f(x,y) - \overline{f}(x,y)][(t(x-u,y-v) - \overline{t}]}{(\Sigma_{x,y}[f(x,y) - \overline{f}(x,y)]\Sigma_{x,y}[(t(x-u,y-v) - \overline{t}])^{0.5}} \tag{5.13}$$

where,
f is the image,
t is the mean of the template
$f(u,v)$ is the mean of $f(x,y)$ in the region under the template.

Figure 5.21 depicts an example of the implementation of this technique in MATLAB. It can be seen that the correlation surface plot accurately determines the match locations and shows the corresponding peaks in the correlation plot.

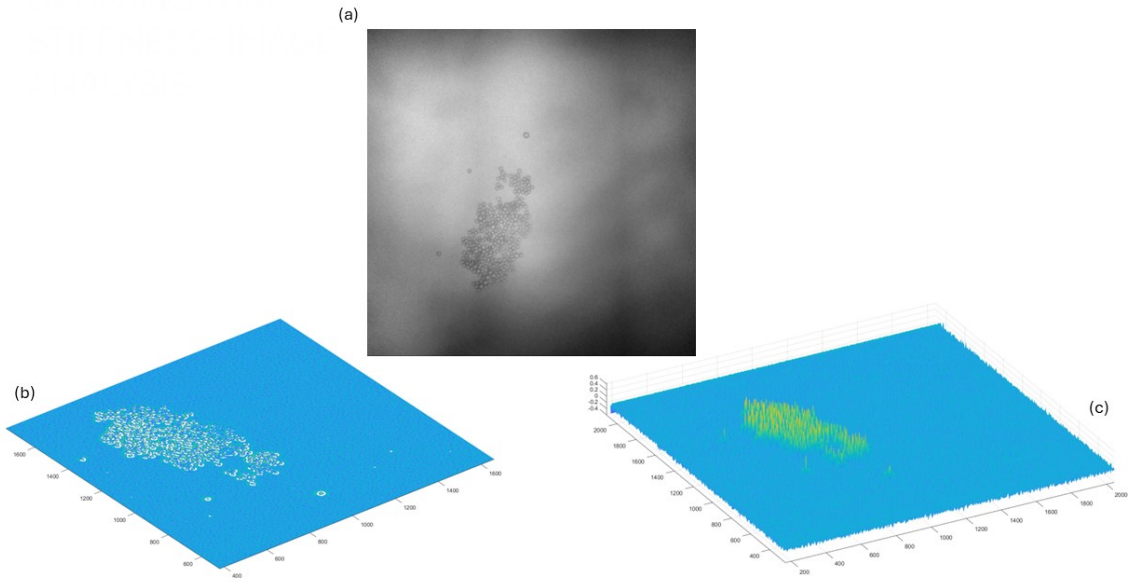

Figure 5.21: Detection of the correlation peaks in MATLAB based on the cross-correlation-based template matching. It can be observed that the MATLAB code precisely detects the bead positions in (a) and displays them in plot (b). The correlation coefficient peaks at the corresponding locations can be observed in (c).

Figure 5.22 depicts the particle spread plots as obtained from the described template matching technique. It can be seen that the spread (and in turn, the variance σ_z) is higher (2.521 μm) for a lower actuation voltage, yielding a lower value of trap stiffness (0.3 fN/μm).

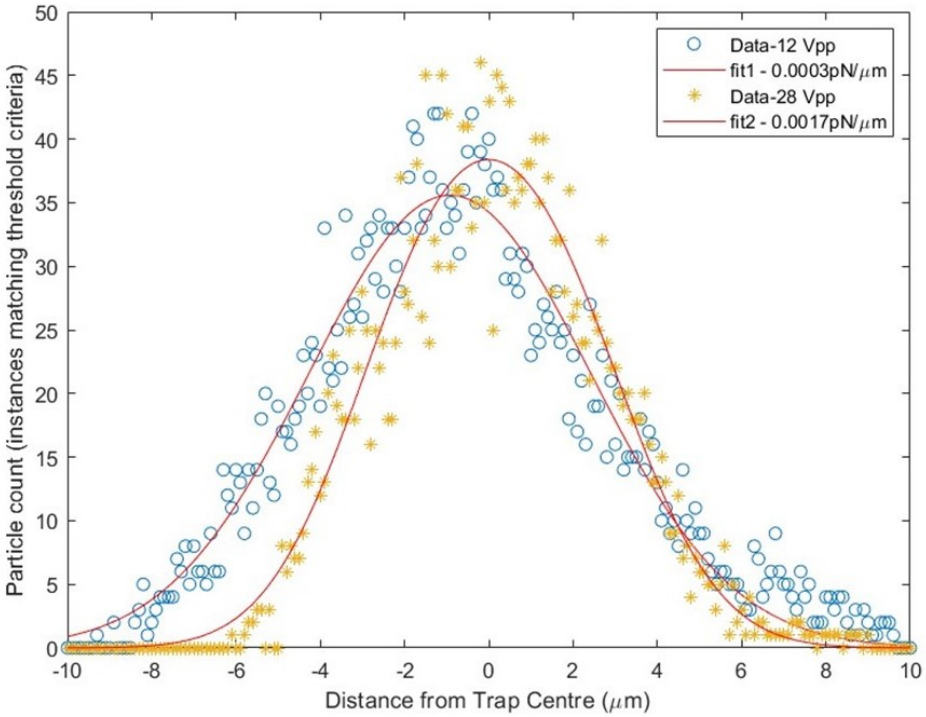

Figure 5.22: Comparing the z-spread of the particles and the resulting trap stiffness for high and low input energies.

Further, to compare the experimental estimates of trap stiffnesses with FEM COMSOL model, the acoustic radiation force was extracted from the COMSOL model by post-processing. For this, a line of particles was added as a geometric entity to the COMSOL model and was placed at the center of the fluid chamber to extract the simulated acoustic radiation force that would be experienced by a particle located at the corresponding position. The simulation setup for this is depicted in Figures 5.23 and 5.24.

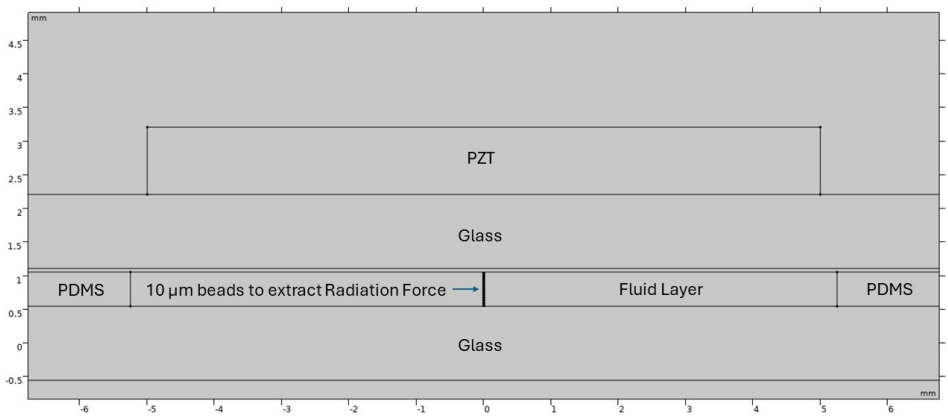

Figure 5.23: Sampling beads in COMSOL to extract the ARF profile from the pressure acoustics domain.

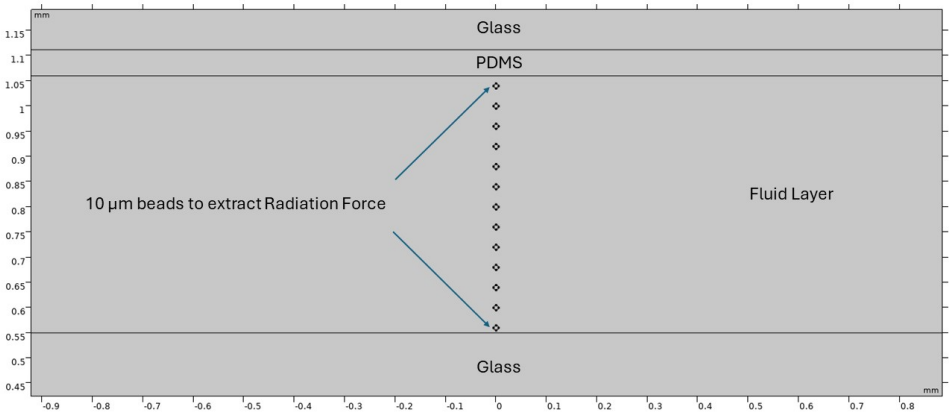

Figure 5.24: Sampling beads in COMSOL - closeup.

After computation of the first-order Acoustic Pressure p_1 and Velocity v_1 fields in the frequency domain in COMSOL, the acoustic radiation force, being a second-order effect, is estimated by integrating the second-order pressure over the surface of the particle. This integral is ideally calculated in time-varying sense, over a moving particle. However, in order to simplify computation and utilize the previously calculated fields, a convective momentum-flux correction term is added to the integral, and the integral is calculated over the equilibrium surface enclosing the particle [102, 103]. The second-order pressure $< p_2 >$ and the surface integral to yield F_{rad} are mentioned below:

$$< p_2 >= \frac{1}{2\rho_0 {c_0}^2} < {p_1}^2 > -\frac{1}{2}\rho_0 < {v_1}^2 > \tag{5.14}$$

$$F_{rad} = \oint_S [< p_2 > I - \rho_0 < v_1 v_1 >].n\, ds \tag{5.15}$$

The time-average operator is implemented in COMSOL as follows:

$$< {p_1}^2 >= \frac{1}{2} p_1 {p_1}^* = realdot(acpr.p_t, acpr.p_t) \tag{5.16}$$

As the model is 2D in nature, the integral was calculated over a curve (line integral) instead of a surface in COMSOL. However, an estimate of the corresponding surface integral can be made by finding the equivalent cylinder height of a sphere of the given radius and multiplying the obtained line integral value by this equivalent factor as below:

$$\frac{4}{3}\pi a^3 = \pi a^2 h_{eq} \tag{5.17}$$

which yields, $h_{eq} = \frac{4a}{3}$

The variation of the Acoustic Radiation Force across the depth of the fluid channel as obtained from COMSOL is shown in Figure 5.25. This compares well in order of magnitude (peak force of order 10^{-2} pN) with the analytical estimation based on the Gorkov formulation (peak force $\sim$ 40 fN) from Chapter 3.

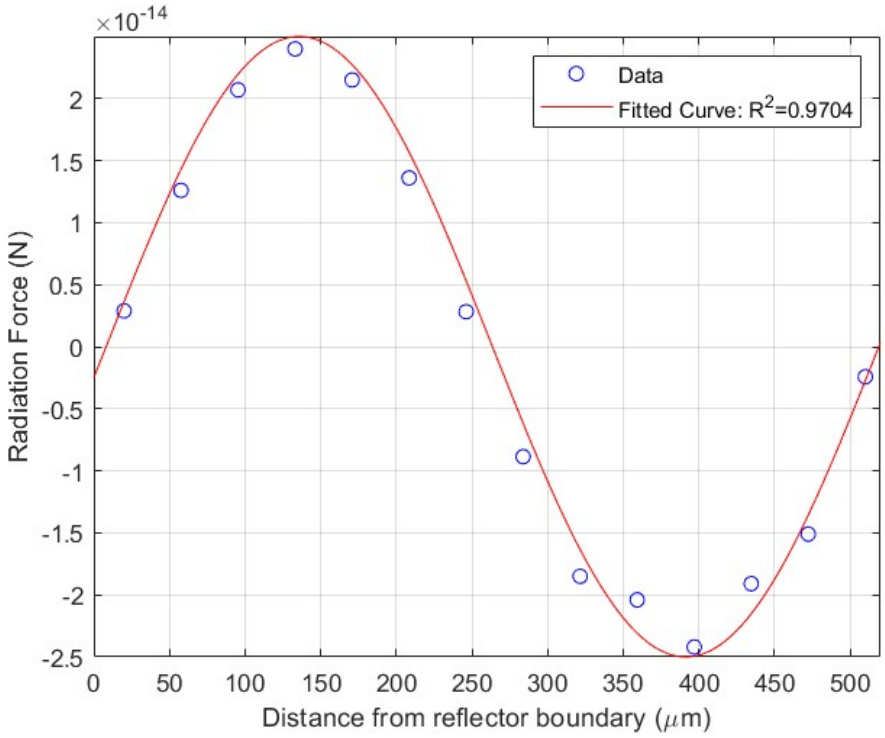

Figure 5.25: Acoustic Force Profile extracted from COMSOL by line integration at 1.48 MHz.

The magnitudes of the Acoustic Radiation Force, within experimental limits, agree with the maximum obtained trap stiffness values of the order of 1 $fN/\mu m$, thus quantitatively validating the suitability and correctness of the analysis techniques used.

5.3.5. Secondary Effects and Clustering

As outlined in the previous sections, on levitation, the particles experience multiple effects in the nodal plane which result in interesting phenomena such as the formation of clusters. This sub-section aims to qualitatively and quantitatively analyze the impact of the controllable experimental parameters on the extent of clustering.
The observations that form the base for the results, and the subsequent arguments are as follows:

- After a steady trap is created by efficiently trapping the particles through a *frequency sweep actuation*, the particles can be maintained in the trap even at a *single frequency* for several minutes. Further maintaining them in the trap could require additional systems such as on-chip temperature control to combat overheating and ensure cell viability.

- The in-plane motion of the particles also included a component from Rayleigh streaming (a unidirectional in-plane flow of particles). However, on the *onset of cluster formation*, this effect no longer impacted the particle agglomerates as they were larger enough for the RF to dominate the drag force.

- The nodal plane trap, on sufficient exposure time repeatably consisted of a single central cluster (mean length of long-axis $\sim$ 350 μm), and multiple smaller secondary clusters formed around the central cluster at multiple locations. The onset of the formation of an early-stage cluster

promotes quicker aggregation of the surrounding particles in the cluster, which can be explained by the scaling of the in-plane SRF with the entity size; hence a growing cluster further promotes particle aggregation into it.

- The small secondary clusters occasionally merged with each other, but there was no predictable pattern observed for this.

- The impact of a transversal PRF component is evident from the fact that a higher voltage causes a sharp increase in the extent of in-plane motion and clustering as depicted in Figure 5.27.

- An interesting observation is also that with a higher particle concentration, the extent of clustering also increases greatly. This is possibly an impact of the SRF, *after* the particles get close enough driven by the transversal PRF. This is because the SRF scales with the reciprocal of the 4th power of the interparticle distance, and thus, only becomes significant when the particles are sufficiently close, and in a sufficiently high concentration (as the SRF emerges from the scattered field which would be stronger with the presence of more particles) as:

$$SRF\alpha\frac{1}{d^4} \tag{5.18}$$

- Thus, in summary, the extent of clustering shows a *positive correlation* with both the *input energy* as well as the *particle concentration*. This presents scope for finding an operating optimal while balancing the required PRF/trap stiffness, the device heating, and the cell seeding density to create a favorable clustering situation. This can also be observed from Figure 5.29.

- A working range for the formation of localized clusters in the nodal plane has been found through experiments in this work. However, the experiments on live cells would better testify the findings and would point to a different optimum.

- Interparticle effects can be included in simulation studies as a further step towards reaching a computational optimum. A strategy for extending the results herein to create a single cluster per well would be the ideal step to achieving the end goal of contact-free Organoid Culturing.

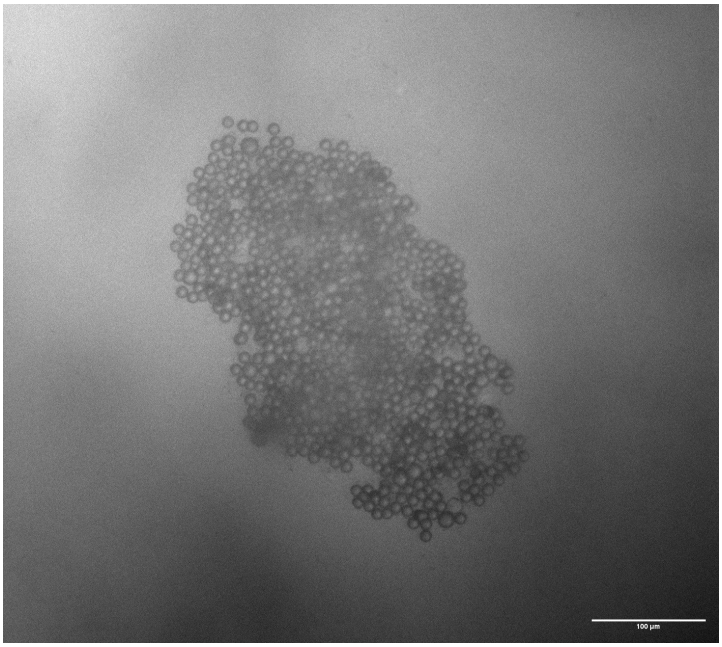

Figure 5.26: A 3D cluster formed in the nodal plane of the fabricated BAW device

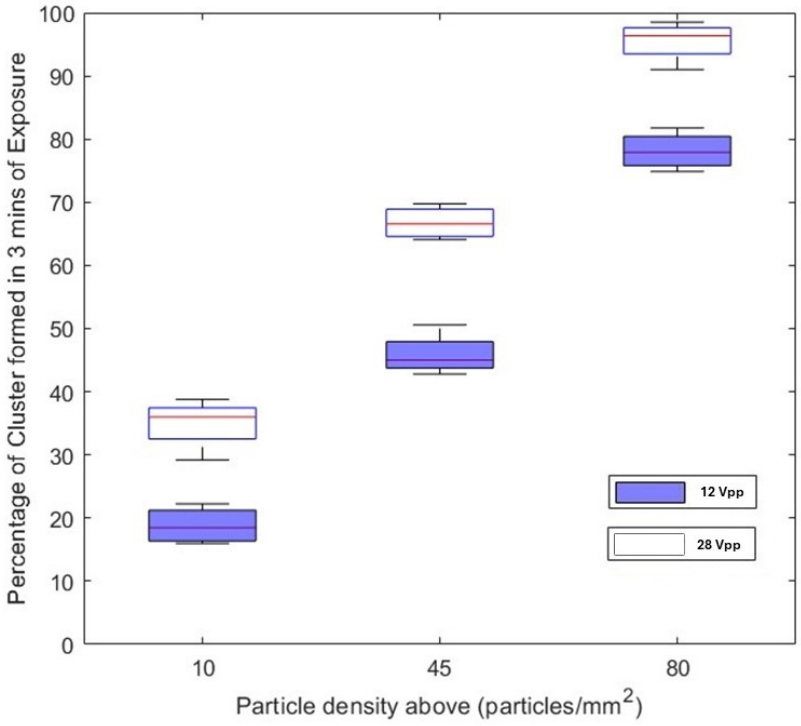

Figure 5.27: Extent of Clustering: Dependence on Particle Concentration.

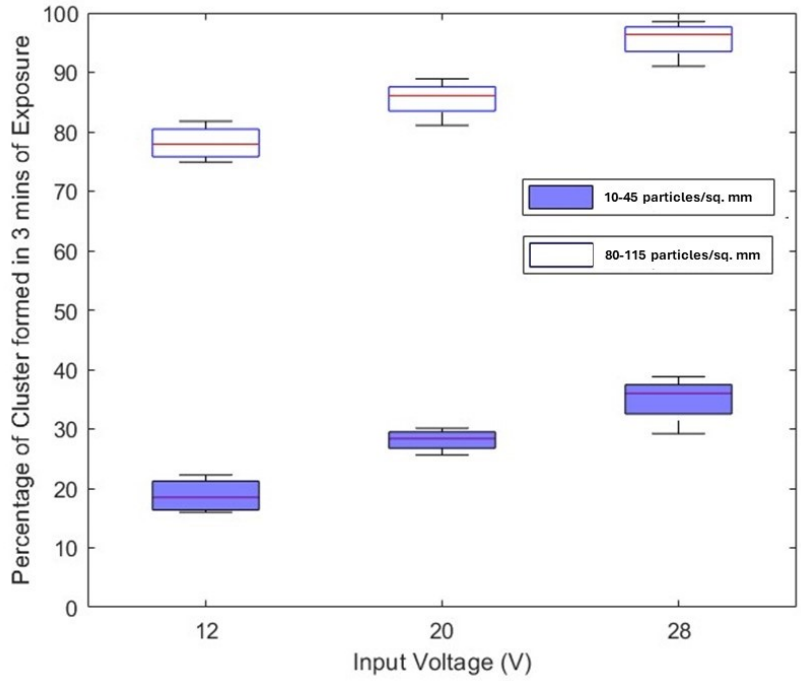

Figure 5.28: Extent of Clustering: Dependence on Input Voltage.

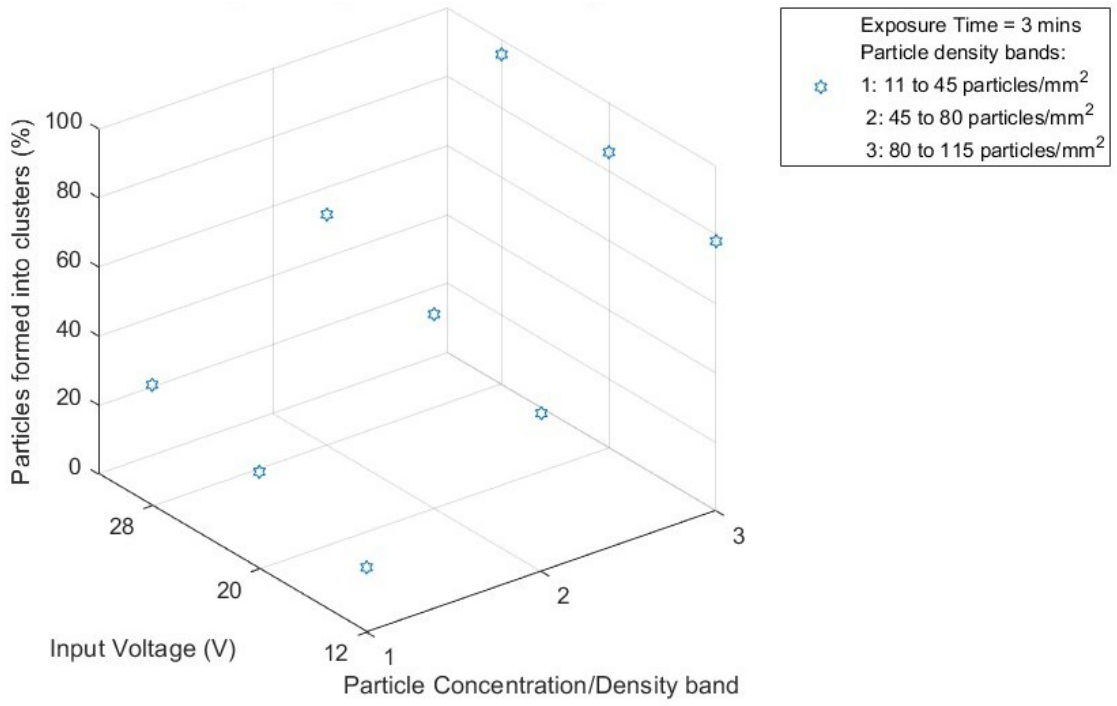

Figure 5.29: Extent of Cluster Formation: A combined 3D plot based on Figures 5.27 and 5.28.

5.4. Conclusion

This chapter discussed the results of the work in detail beginning from the fabrication intricacies, to the characterization of the transducer-on-chip both electrically and mechanically. Finally, the trapping experiments were described in detail, wherein the interplay of various acoustofluidic effects was outlined. The key findings herein are:

- The device characterization showed repeatable trapping over a bandwidth of 300 kHz and the possibility to control the trap height within this range as depicted in Figure 5.9.
- The streaming-based drag that reduces the trapping efficiency can be overcome by *controlling the input energy*, as well as *adopting a frequency sweep actuation scheme*.
- The fabrication imperfections that lead to a non-uniform thickness and in turn an inconsistent standing field can be overcome by, once again, *a frequency sweep*, leading to resulting *trap efficiencies of up to 95%*.
- The trap stiffness can be estimated effectively by image processing techniques complementing the equipartition theory.
- The maximum trap stiffness calculated by imaging of clusters was 1.7 $fN/\mu m$ which agrees in order of magnitude with the COMSOL estimation of the acoustic radiation force (peak force 25 fN) and the Gorkov formula for a peak pressure amplitude of the order of 10 kPa (peak force 40 fN). The experiments depict that this value of k_a is adequate to maintain levitation, yet low enough to form a 3D cluster of particles in the nodal plane, which points towards the end goal envisioned.

- The analysis of the extent of clustering shows that there is a surface (as shown in Figure 5.29) of possible combinations of the experimental variables that *can yield stable clustering*. This range is, however, expected to be different for live cells, which can be determined by further experiments.

- *This work creates the foundation (a PoC complete with a straightforward fabrication method and dimensions/lengthscales that suit organoid culturing) for the repeatable, controllable, and contact-free formation of stable clusters in the nodal plane of an SBAW device, with dimensions and materials suited to the end application. This paves the way for adopting a strategy, firstly for promoting the nodal plane clusters to form a single 3D cluster (per well), which would be an ideal outcome towards the end goal; and secondly, for integration of such a device structure with standard biological formats such as well-plate arrays as a promising future outlook towards assessing acoustic stimuli as a driving cue for cell agglomeration and organoid development*.

6

Outcomes: Relevance and Suitability

The preceding chapter discussed the key findings and results from the fabrication, characterization, and trapping experiments performed under the scope of this work. It also presented an overview of the experimental parameters that can be controlled and tuned to optimize the trapping performance and efficiency. This discussion note qualitatively and quantitatively summarizes and highlights the results and corollaries of the findings in the context of their relevance to the target application of organoid cultures. The highlights are revisited in Figure 6.1.

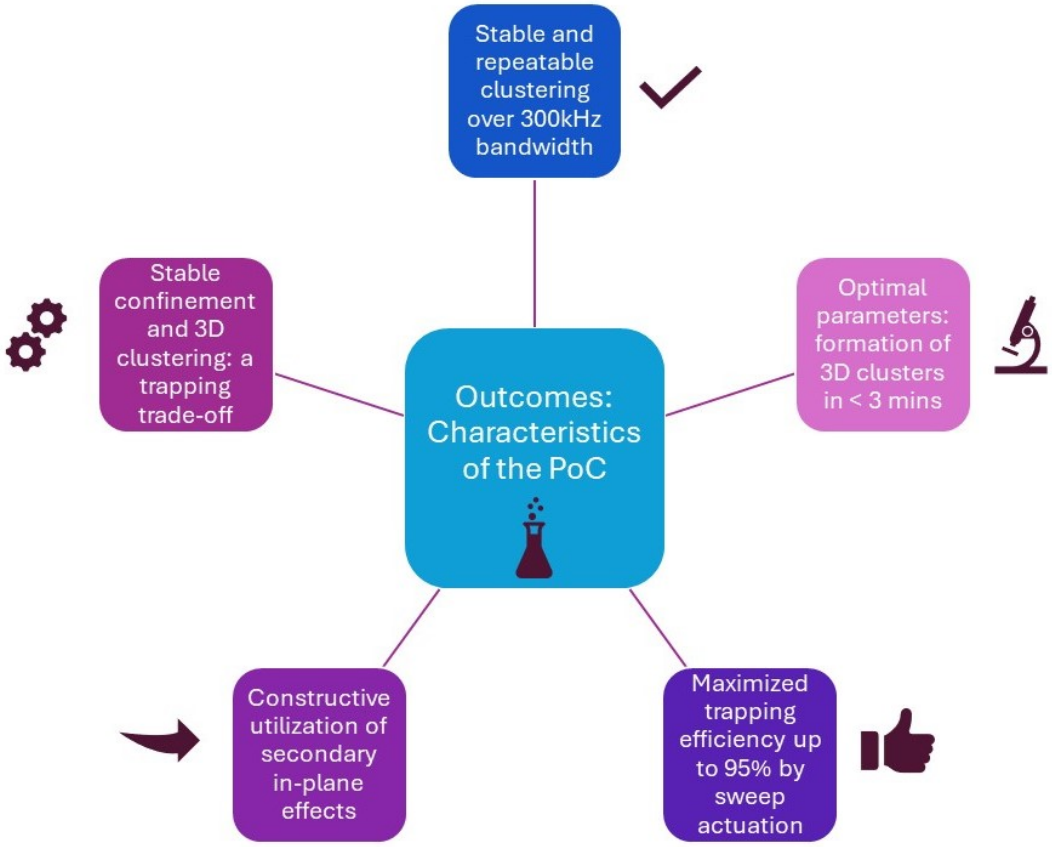

Figure 6.1: Key Characteristics of the PoC.

- This work successfully demonstrated the *contact-free manipulation* of cell-like particles (acoustically similar to cells) in fluidic structures suitable in planar dimension and materials for culturing of live cells. This was done while retaining optical access for live microscopy and ensuring minimal setup complexity, with fluidic and electrical connections from a single side of the device. This is an improvement over Silicon-based resonators that limit flexibility in optical access and microscopic compatibility [104], or multi-transducer systems [48].

  This is a crucial step in the contact-free *levitated culturing* of cell clusters in organoid culture applications. This approach is potentially promising and closer to creating an in-vivo condition-mimicking environment for certain cell types such as neuronal progenitors and embryonic cells.

- The work demonstrated the realization of a BAW resonator with a *wide bandwidth* of 300kHz, making it robust and tolerant to frequency fluctuations and variations, which is an advantage with polymer-based systems [86]. This is an improvement over similar works where the levitation was observed only in a narrow band around a very sharp resonance frequency [46, 104].

- After creating a half-wavelength acoustic trap for maintaining the microspheres in stable levitation, it was shown that the in-plane force effects can be utilized *constructively* to promote cluster/agglomerate formation in the nodal plane.

  The *secondary in-plane and interparticle effects* which are otherwise seen as an unsolicited (and at times, not useful) phenomenon in relevant literature in the field [105], can actually be put to use for the application envisioned, which has been demonstrated through this work. For instance, the Rayleigh streaming contributes to the in-plane motion of particles until the onset of clustering. The transversal PRF resulting from imperfections also promotes the in-plane motion of particles, and the clustering is promoted even further by the SRF.

  The next step in the process is to gain higher predictability in the secondary effects by higher modeling complexity such as the inclusion of hydrodynamic and inter-particle phenomena in COMSOL and analytical approaches (such as in [106]), which comes at the cost of higher computation, yet, likely to point to interesting findings as well.

- The work shows that a suitable working range can be established in order to achieve *stable, controllable nodal plane clustering* of the particles. A tradeoff between the applied input energy V_i, (and in turn, the trap stiffness k_a), and the particle concentration in the solution (which affects the extent of the inter-particle effects produced) can be worked out in order to achieve effective 3D cluster formation. This working range, however, has been estimated for polystyrene microspheres and is expected to be different for live cells, which is why biological experiments are recommended as the immediate next step. The establishment of the parameters that shall give rise to this working range has been successfully presented in the work, and agrees with the observations from corresponding biological point-of-use research as well [107].

  The estimated trap stiffness also depicts a healthy tradeoff between the *stable particle confinement ability* and the *3D nature of clustering* observed in the system.

  Previous works have depicted acoustic trap stiffnesses of up to a few pN/μm [46], which is higher than the estimated stiffness here, however, the stiffness estimations have been limited to low particle interaction systems, and thus do not account for the 3D clustering effect. These accounts of the trap stiffness, thus, do not translate into the multi-particle trapping that is of interest herein. On the contrary, this work estimates the trap stiffness based on the particle clusters and hence is more closely indicative of the experimental scenario for the target application. Further, there has been limited scope for 3D structure formation in such systems [108], in contrast to the 3D agglomerates formed in this work.

Further, The PZT could be actuated for extended durations of time (up to 10 hours) in long-run experiments without significant impact on the PZT characteristics and no observable impact on the associated chip components such as the fluidic connections (details in Appendix C), and the particles formed ellipsoid geometries similar to those observed in acoustically levitated spheroid cultures [109]. This is indicative of the potential of the technique to be adapted to long-term cultures with suitable add-on elements (details in Chapter 8).

- Techniques for maximizing the trapping efficiency of the fabricated proof-of-concept were explored and it was effectively demonstrated that a *multi-frequency actuation* scheme was successful in suppressing unwanted streaming effects while also overcoming the limitations posed by fabrication inconsistencies. It was also shown that the multi-frequency actuation yields a trapping efficiency of up to *95%* for an exposure time of $\sim$ 1 min. This indicates that, thereafter, a single frequency drive is sufficient to maintain the clusters in suspension for longer periods. Previous works have demonstrated streaming suppression by using pulsed ultrasound [110, 111], or by control of input voltage alone [81], however, a frequency sweep was shown to work effectively in this thesis and is a promising solution.

- Time spans as short as 3 minutes were observed for initial clustering of the nodal trapped particles in the fabricated Proof-of-Concept. This indicates a sharp decrease in the time required for the formation of initial clusters when driven acoustically (typically a drop from several hours and days [112] to a few minutes). With add-on components (discussed in Chapter 8) to mitigate the anticipated/possible undesirable effects of long-actuation times and ensure live-cell viability, these clusters can potentially be sustained for up to several days. It is thus a very promising direction to observe the impact of this accelerated agglomeration on the development of the organoids. This aspect has been discussed as being of interest to potential collaborators in this project as well, similar to the next biological aspect presented below.

- The acoustic manipulation technique demonstrated in this work employs acoustic forces (mechanical forces) as *stimulative cues* for the trapping and clustering of particles, and eventually, cells, in the envisioned application. The impact of short acoustic exposures (up to a few minutes) have been reported to have no adverse impacts on cell viability and gene expression capability/pluripotency of cells [107, 113], which is a promising foundational headway. However, the impact of the acoustic forces as mechanical cues on the developmental aspects of organoids that are cultured by this technique has not been looked into in literature. Thus, a promising direction of research lies in the investigation of the impact of such a *contact-free* and *acoustically stimulated* culturing system on organoid maturation. This work, thus, presents an *in-house fabricated and characterized PoC* as an *enabler* to investigate this novel research direction.

The Figure 6.2 summarizes key aspects of the outcomes in view of the point-of-application.

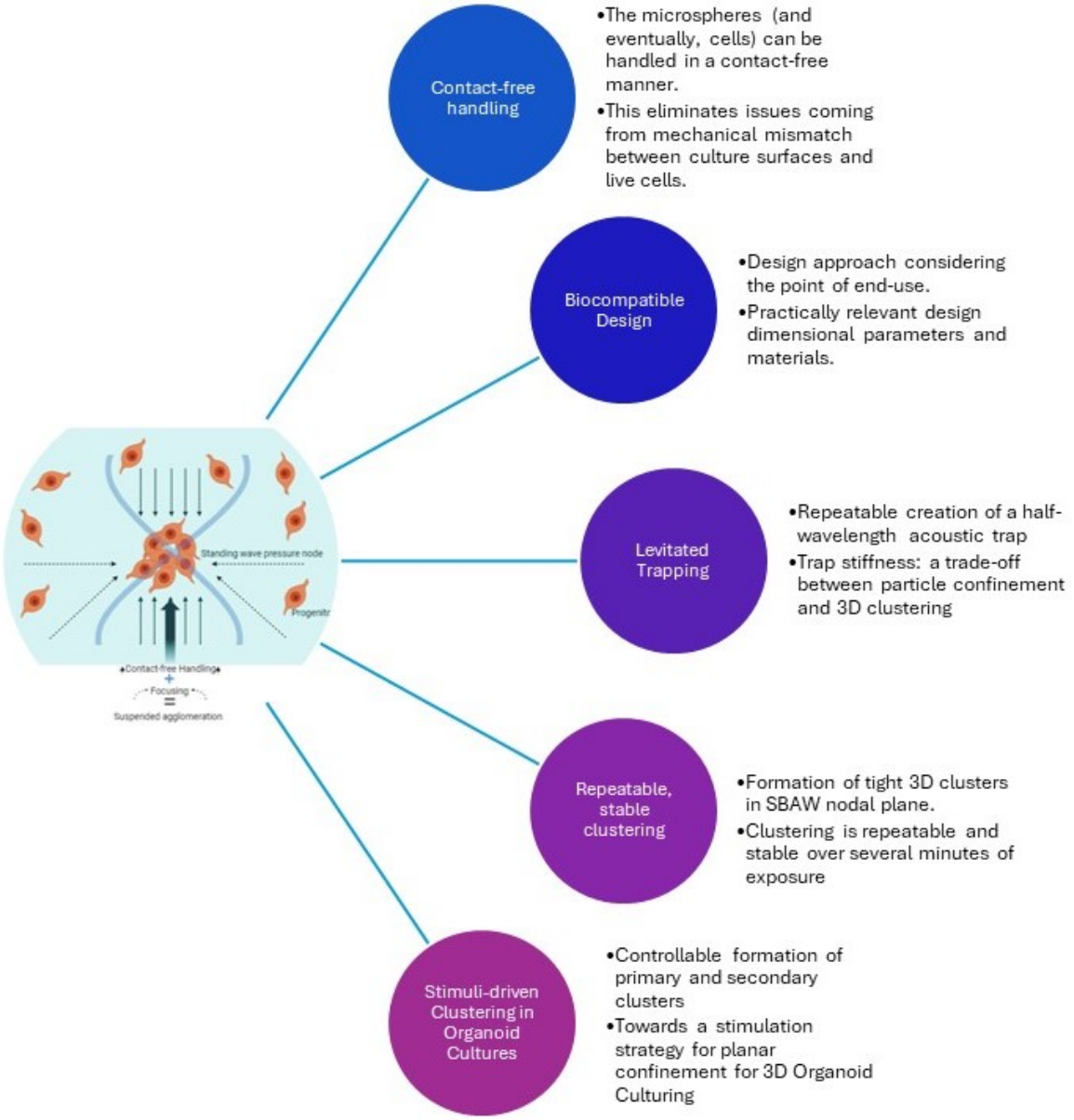

Figure 6.2: Applicability and significance of the study in the point-of-application

7

Conclusion

The key suitability and extrapolation pointers in regard of the application of the research envisioned have been discussed up to this point. Figure 7.1 depicts a bigger picture of the work presented in this thesis. The concentric circles depict the viewpoint from which the work can be looked at, and the associated prominent aspects that relate the biological objective to the viewpoint. The repeatable formation of 3D clusters in the SBAW nodal plane is central to this bird's eye view. This paves the way to enable contact-free clustering of cells. When complemented with a strategy for focusing to create a single cluster per well, or employing a multi-well chamber structure, this leads to the formation of discrete early-stage agglomerates, which can be maintained in suspension to mature into organoids. Lastly, the broadest viewpoint stems from the biological research outlook of realizing mechanical stimuli-driven high throughput organoid culturing through acoustofluidic manipulation.

This work exemplifies a baseline step in realizing acoustically-stimulated organoid culture systems compatible with existing culture platforms, dimensionally and material-wise, which can enable scientists to achieve higher throughput in organoid cultures in a cell-friendly manner to address the ever-growing need for in-vitro organ models.

Figure 7.1: Envisioned bigger-picture of the work, depicting the core aspects outlined in this thesis, as well as the application roadmap.

8

Future Outlook

The work carried out under the umbrella of acoustofluidic levitation for organoid cultures in this thesis forms the base for conceptualizing a system capable of culturing primitive cell agglomerates, and eventually organoids in a biocompatible, optically accessible manner, enabled with a mechanical stimulus for accelerating organoid development. In view of the intended point-of-use, this chapter outlines the envisioned downstream pathways and add-on functionalities that would enable more versatile applications, and robust operation, and overcome some challenges that were faced in this work. These aspects have been discussed in the coming sections.

8.1. Add-on Components

In order to enhance the acoustic or biological functionality of the device structure, several avenues have been proposed in this section along with a pictorial depiction of an envisioned implementation and the rationale for the same.

8.1.1. Acoustic Functional Components

To improve the device functionality in acoustic terms, or add an additional mode of functionality to the device, add-on acoustical elements/strategies are described herein. The first functionality-enhancing strategy could be adopting transversal trapping mode(s) with tuned stiffness of each mode. In such a device setup, PZT(s) are attached to the high-impedance channel material, and actuated at appropriate frequencies, to create $\lambda/4$ matching conditions of the channel walls, and a half wavelength mode for the channel as depicted in Figure 8.1. The high-impedance channel structure resonates as a single unit, and trapping is achieved by creating a standing wave by reflections between the channel walls [114].

Adding this mode to the layered resonator structure as described in this thesis yields a trapping strategy as shown in Figure 8.2, wherein the layered and transversal modes can be actuated by two different frequency PZTs to achieve both an in-plane trap, as well as levitation. The symmetrical placement of additional PZTs can also add a third trapping mode to the other two, of which the stiffnesses can be tuned to achieve a 3D control over the clustering. Similarly, tuning the resonances of the three modes to be equal, a single PZT can also excite the resonator for 3D trapping [104], provided sufficient energy density is achieved in the fluid well through appropriate choice of trapping

geometry [115].

Though a promising long-term goal, this method comes with the challenge of a more complex fabrication technique as the channel would need a high acoustic impedance material preferably with straight walls, and would add additional circuitry with multiple transducers. Precision manufacturing with Silicon is a promising alternative, which, however, blocks optical access partially, a key component in biological applications. This can be overcome by arranging the transducers on the opaque material side of the resonator to leave a glass optical window for access. However, setting up the fluidics from the glass side still remains a task to be handled for microscopic compatibility.

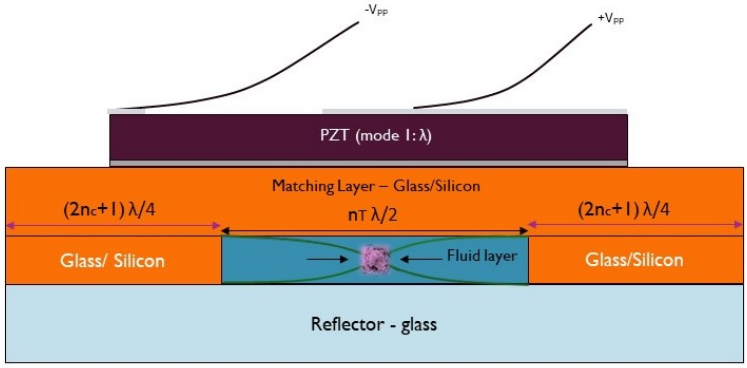

Figure 8.1: Schematic implementation of Transversal Trapping mode in Acoustic Resonators.

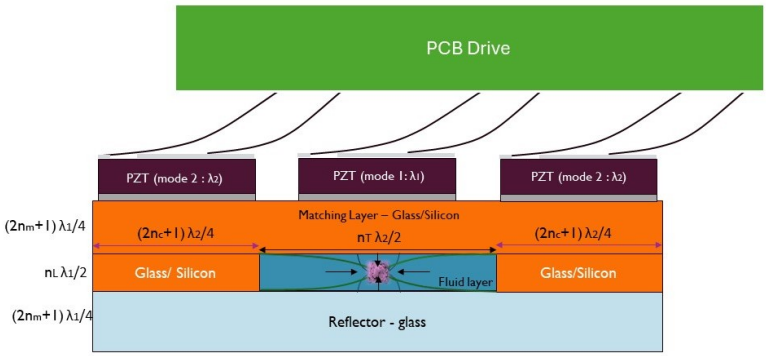

Figure 8.2: Schematic implementation of multi-modal (layered + transversal) trapping with the associated control circuitry.

A beam steering approach with phased arrays can be another alternative to localize the acoustic energy and confine the standing wave. In a transducer-reflector-based arrangement, it could be implemented to steer the beam such that a localized yet stronger standing wave is created. Further, by selective actuation of the array transducers shown in Figure 8.3, the trapped particles can be sequentially assembled and possibly transported [116], which can be aided by an active flow in the chamber. However, this too may involve complex circuitry which would need a PCB drive. Though an option worth exploring, the electronic setup complexity is often not preferred in bio-lab research and integration with live imaging.

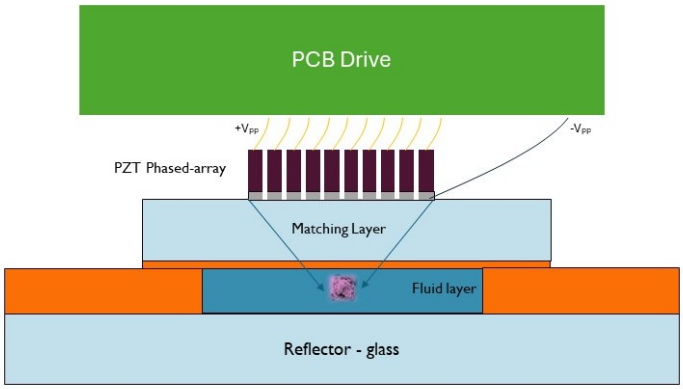

Figure 8.3: Schematic implementation of a multi-transducer phased array in a BAW resonator, with the associated control circuit.

The results of this thesis also show the formation of multiple clusters throughout the nodal plane separated in space by $\sim$ 100-200 μm, which depicts a possibility of up-scaling by employing a multi-well setup, each well having a specific diameter and cell seeding density as shown in Figure 8.4. The key consideration herein, however, is the material of the wells. It has been observed that a high attenuation material in the path of the acoustic wave propagation can cause loss of energy, and insufficient energy density in the fluid cavities (refer to troubleshooting chart A.4). Thus, such an implementation shall require a low attenuating material such as PMMA [117], and optimization of the well geometries to ensure minimal attenuating material in the wave path. To demonstrate the multi-cluster formations observed in the experiments, a supplementary figure has been provided in Appendix C.

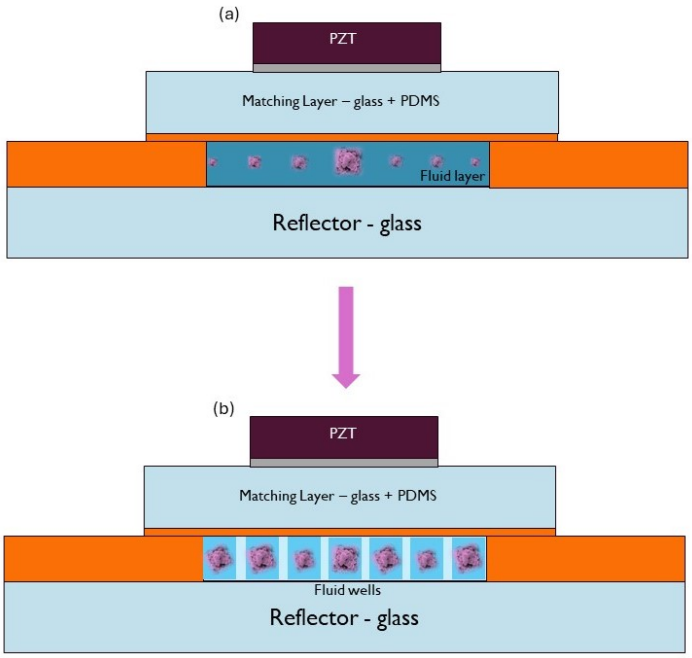

Figure 8.4: Fluidic surface division into multiple wells as an enabler to obtain multiplexed/parallel clustering for high throughput.

Lastly, maintaining the simplicity of the stack, a beam-focusing mechanism was explored as a potential solution. Focused ultrasound has been explored for acoustic trapping in some works in literature [118, 119]. However, this comes with the challenge of a new device structure altogether, as the concept of a resonator (transducer-reflector pair) cannot be applied directly unless two opposing

focused transducers are implemented. Hence, this solution would not be discussed further in the scope of this project.

8.1.2. Secondary Systems

In addition to the acoustical functionality of the system, temperature control is an important aspect when it comes to longer culturing times. In the current experiments, overheating was not a major concern up to 10 hours of actuation, however, in the longer experiments, heat extraction systems, if needed, can be added with a cooling channel and Peltier elements [120] as shown in Figure 8.5.

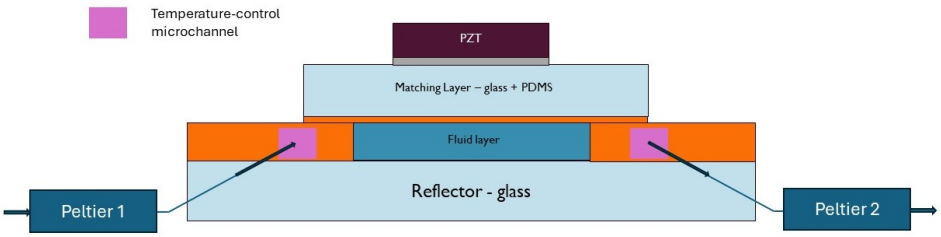

Figure 8.5: Peltier elements as on-chip temperature regulating systems, and possible integration in a BAW device structure.

8.2. Characterization Improvements

Extensive characterization techniques can be employed to improve the quantitative understanding of the device's functionality. For example, pressure measurement by conventional tank hydrophones is not viable due to the closed nature of the channels, however, a fiber optic hydrophone as depicted in Figure 8.6 can be integrated into the system [121]. Temperature estimation by conventional thermal imaging is challenging in systems of microscale due to the limit of resolution [122], however temperature estimates can be made using thermocouples, temperature sensitive-dyes and channel materials [123] as depicted in Figure 8.7.

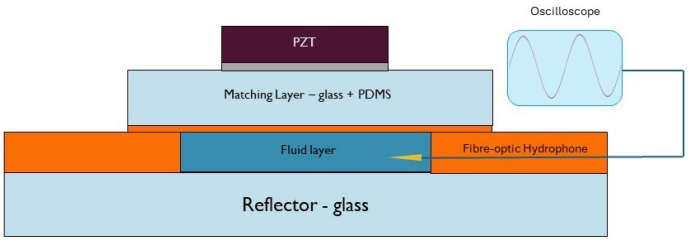

Figure 8.6: Integration of a fiber optic hydrophone for pressure field characterization on a BAW device, schematically.

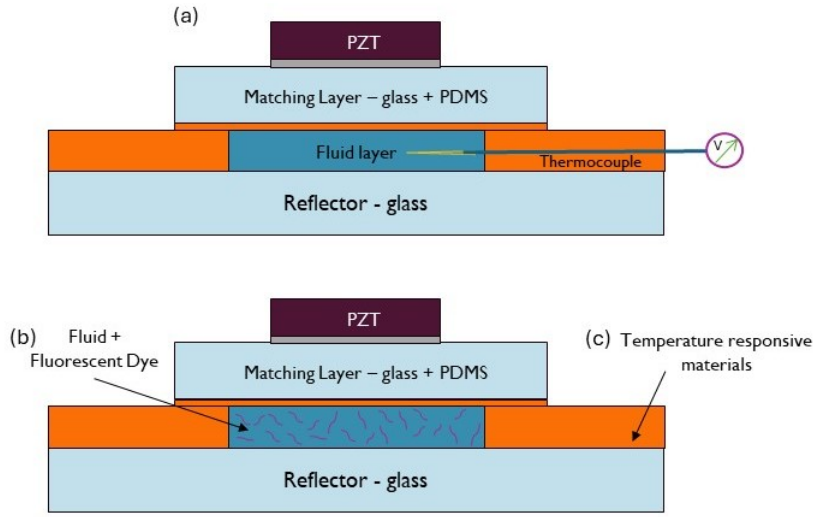

Figure 8.7: Temeprature estimation alternatives in a closed BAW fluidic system as described in this work by: (a) Integrated thermocouple probes, (b) Temperature responsive fluid additives, (c) Temperature responsive channel materials/material additives.

8.3. Fabrication Improvements

Improvements in fabrication strategies can be employed, with an evident tradeoff between complexity of processing and the accuracy of the resulting structures. Accuracy is desired particularly for the fluidic channel walls, and the thickness, depending on the type of resonator structure. This can be achieved by processes such as laser micromachining for glass (trenches and angled sidewalls can still be an issue in transversal modes), Deep Reactive Ion Etching for Silicon, and Direct Laser Writing for polymeric/biomaterials for layered resonators like the one described in this work, as depicted in Figure 8.8.

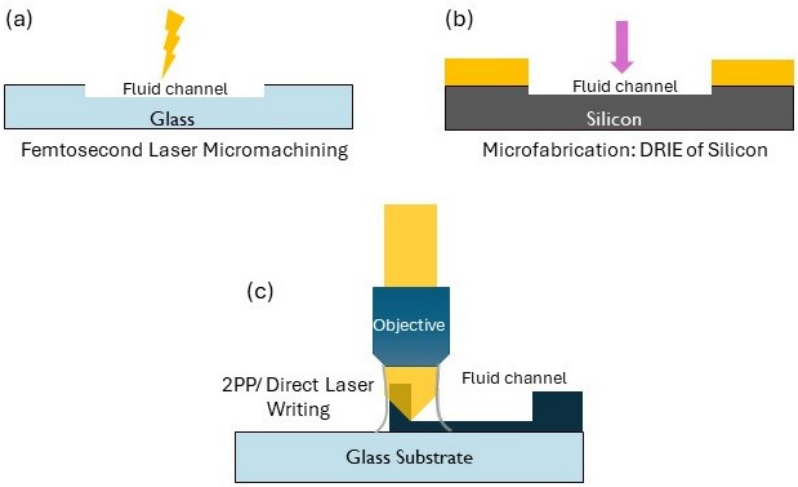

Figure 8.8: Improvements in Fabrication: (a) Femtosecond precision laser micromachining of Glass and Silicon, (b) DRIE of Silicon to obtain deep channels with straight walls, (c) Direct Laser Writing/ 2PP for precision printing of fluid channel on glass substrate.

A

Appendix A

Project Methodology

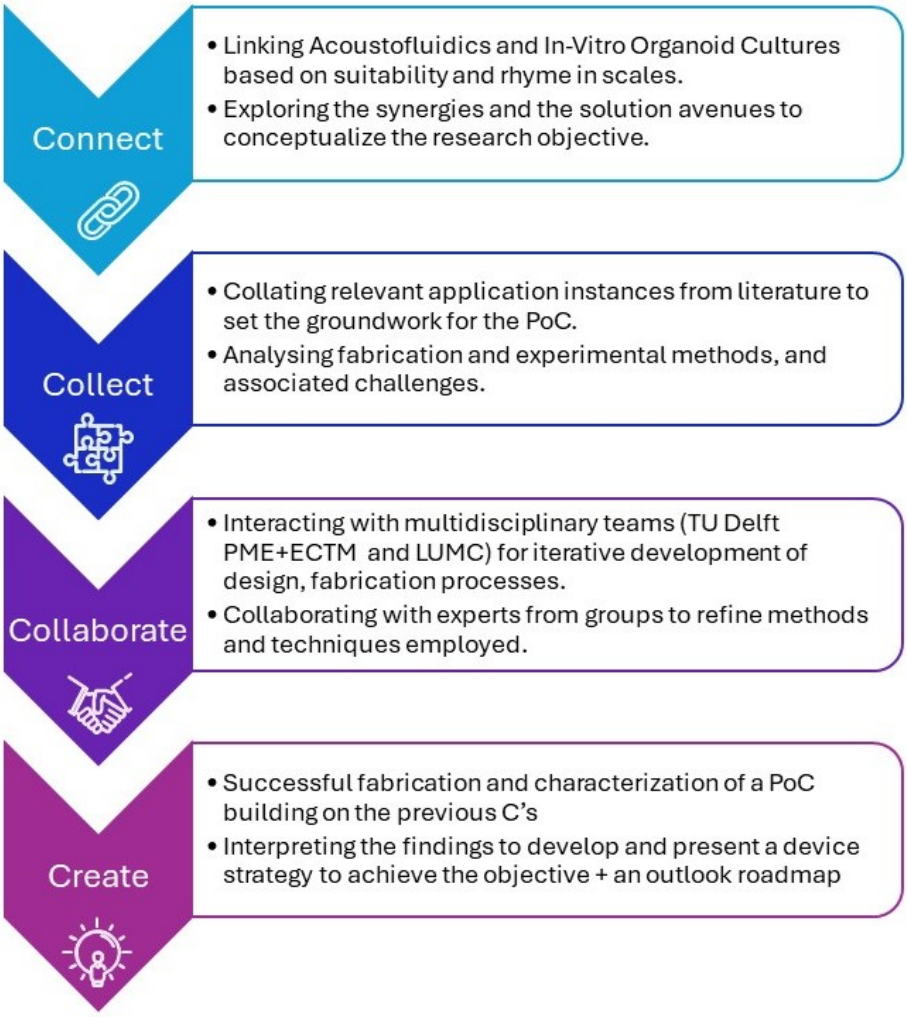

Figure A.1: A 4'C' Methodology adopted to realize the project, with the details of each 'C'.

PoC version 1

A quick-to-fabricate PoC using readily available off-the-shelf components and minimal processing involved was made as a starting point in the project. This involved a structure as shown in Figure A.2, with a fluid resonant cavity 90 μm thick and a resonance at 7.5 MHz. The acoustic pressure field and the picture of a completed fabrication of this version are shown in Figure A.3. However, this phase involved a lot of iterations and troubleshooting in the PoC v1 to achieve resonance and levitation. This enabled the creation of a detailed analysis of the possible failure modes that were considered during the troubleshooting phase. The anticipated sources of failure and the measures taken to mitigate each of those have been tabulated in Figure A.4.

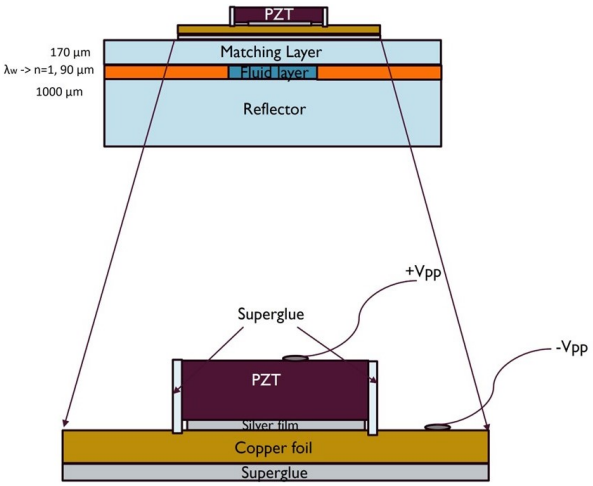

Figure A.2: Layered structure diagram of the PoC version 1.

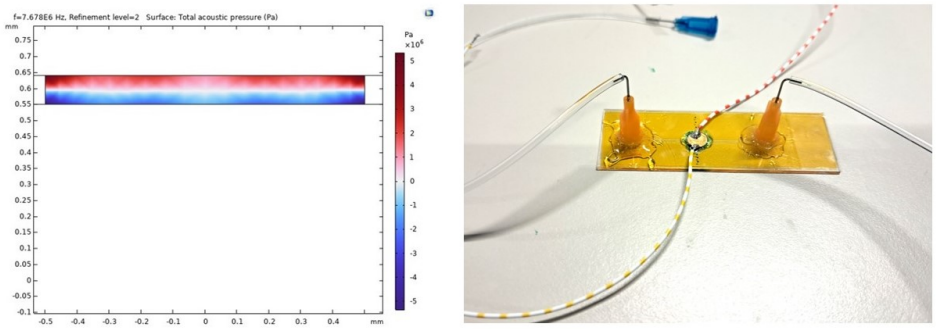

Figure A.3: The simulated fluidic resonance in PoC version 1 (a), and the fabricated device (b).

PoC Final Version: Rationale

The analysis of the failure modes paved the way for troubleshooting in further device iterations of the final PoC as well. The finalized design, however, was conceptualized based on the target dimensional range suited for the intended application (sub-mm), and biocompatible material choices. The device characteristics described from Chapter 4 onwards were taken up from this point.

	Off-design frequency and layer thickness discrepancies	Additional layers (glue, electrodes): air gaps and acoustic attenuation	Attenuation of Acoustic field due to fluid surface area mismatch	Impedance mismatch of matching layer	Off-resonance operating range (PZT)	Ineffective transmission-bonding issues/ air gaps/ metal shielding on air interface	Fabrication intricacies: glue, leakages, sticking of beads, soldering/ connections
Iteration 1							
Iteration 2	To be addressed	To be addressed	To be addressed	To be addressed	To be addressed	To be addressed	Ethanol + DeMi water flushing o channel
Iteration 3	Frequency sweep and continuous recording to determine resonance	To be addressed	To be addressed	To be addressed	To be addressed	To be addressed	+ Flushing, sharp edge reduction, epoxy glue instead of cyanoacrylate
Iteration 4: Trap achieved in PoC version 1	Frequency sweep and continuous recording to determine resonance	Wrapped around piezo electrodes (electrode + glue eliminated)	To be addressed	To be addressed	To be addressed	To be addressed	+ Flushing, epoxy glue to avoid leakage at inlet/outlet, minimizing inlet dispenser-fluid inlet size mismatch
Iteration 5	Frequency sweep and continuous recording to determine resonance	Minimal glue amounts, fast curing with activator	Increased fluidic surface area (48/24 well plate size) to match PZT dimensions	To be addressed	To be addressed	IPA + water cleaning of all glass surfaces before bonding + metal sandwich	+ Using low temperature solder paste to minimize thermal damage, Cyanoacrylate glue + activator spray for quick curing
Iteration 6: Conceptualizing PoC version 2 (final design)	Frequency sweep and continuous recording to determine resonance	+ Minimizing impedance mismatch with PDMS structure	Increased fluidic surface area (48/24 well plate size) to match PZT dimensions	PDMS as thin matching layer and fluidic channel material	Matching PZT frequency spectrum with target frequency range	+ Oxygen plasma bonding for PDMS-glass	+ Cyanoacrylate glue + activator spray for quick curing Homogeneous glue layer by brush

+ Steps taken to mitigate issue in addition to previous column

Figure A.4: Troubleshooting and Identifying Failure Modes: Anticipated sources of non-functionalities/errors in the resonators, with the steps taken to eliminate each.

Microscope Calibration

The trapping imaging and measurements were first carried out on a manual stage microscope. The microscope z-dial was calibrated to obtain the real travel vs the dial reading. This was done with the help of a 3D-printed stepped calibration sample as shown in Figure A.5. The 3D printing was carried out on the Asiga Max DLP 3D printer using the MoiinTech Clear Resin, followed by gold sputtering at 20 mA for 30 sec to render the surface reflective.

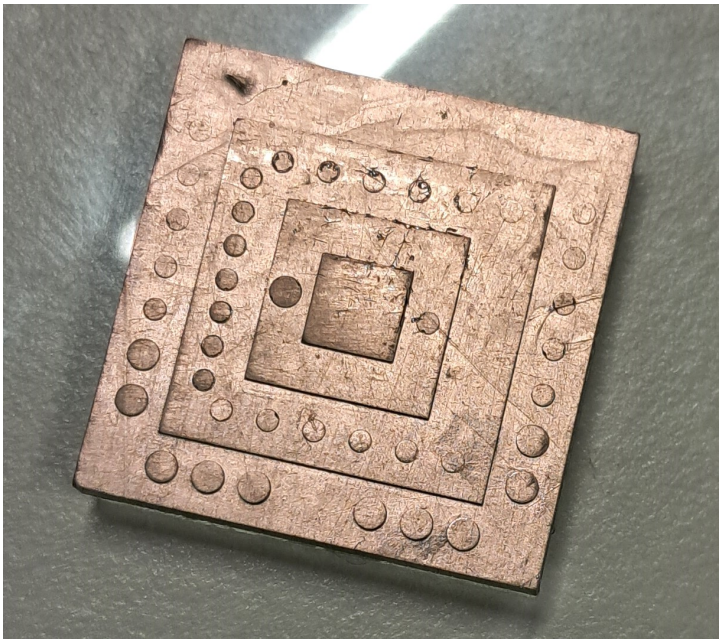

Figure A.5: 3D printed gold sputtered calibration sample.

The sample was characterized by White Light Interferometry to determine the true step heights resulting from 3D printing as shown in Chapter 4 (Figure 4.25). After the characterization of the sample steps, the true step heights were used to calibrate the manual z-dial of the microscope. The result is shown in Figure A.6. It was observed that the dial readings varied considerably in multiple trials, and hence the measurements were not reliable enough to quantify the parameters such as trap height and z-spread for image analysis. Further, only a 10x objective could be used, as the alternative 60x objective had a very short working distance of 200 μm, and thus it was not possible to image through the 1mm thick glass slide. Hence, the microscope was only used for recording trapping and particle counting videos, and further experiments were carried out on a microscope with a precision z-stage as described in Chapter 4.

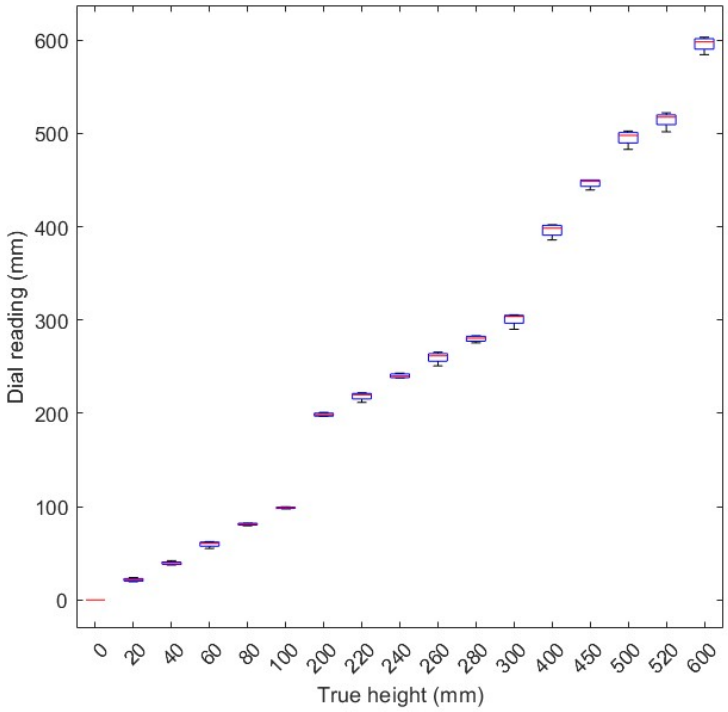

Figure A.6: Calibration plot for manual stage microscope.

B

Appendix B

MATLAB code for template matching

F: ▸ BioMedical Engineering TU Delft ▸ Master_Project_final ▸ Final_device_measurements ▸ referencebead ▸

Live Editor - F:\BioMedical Engineering TU Delft\Master_Project_final\Final_device_measurements\MATLAB_code_croscorr_withcomments.mlx

MATLAB_code_croscorr_withcomments.mlx

```
% Load directory to read images
imagefiles = dir('F:\BioMedical Engineering TU Delft\Master_Project_final\Final_device_measurements\referencebead\')
% Create cell array to store reference bead images
nfiles = length(imagefiles);
imcell = cell(1, 50);
imsum=zeros(22,22);
for i=1:nfiles
    % Extract images from imagefiles structure by the name field
    temp=extractfield(imagefiles(i,1),'name');
    % Store reference images in the cell array
    imcell{1,i}=imread(temp);
    % Calculate reference image sum
    imsum=imsum+imcell{1,i};
end

% Calculate average of reference beads
imavg=imsum/50;

for i=1:50
    % Calculate cross-correlation between imavg and each reference image
    imm=normxcorr2(imcell{1,i},imavg);
    % Store maximum cross-correlation coeff value
    % (corresponding to perfect overlap at centre)
    maxval(i)=imm(21,21);
end

% Find threshold from mean of maximum values
threshold=mean(maxval);

% Create cell array to load z-stack
C = cell(1, 201);

for i=1:201
    % Load z-stack
    im=imread('4Vpp_0.1_20.tif',i);
    C{1,i} = im;
end
```

Figure B.1: MATLAB Template Matching Code - Part 1

F: ▸ BioMedical Engineering TU Delft ▸ Master_Project_final ▸ Final_device_measurements ▸ referencebead ▸

Live Editor - F:\BioMedical Engineering TU Delft\Master_Project_final\Final_device_measurements\MATLAB_code_croscorr_withcomments.mlx

MATLAB_code_croscorr_withcomments.mlx

```
for i=1:201
    % Load z-stack
    im=imread('4Vpp_0.1_20.tif',i);
    C{1,i} = im;
end

Crr = cell(1, 201);
for i=1:201
    % Calculate normalized cross-correlation between each layer of stack and the average image
    % Based on formula stetd in chapter 6
    Crr{1,i}=normxcorr2(imavg,C{1,i});
end

% Plot the correlation map at the centre of the trap
surf(Crr{1,100})
shading flat

for i=1:201
    A = Crr{1,i} > threshold ; % Apply threshold
    Cfil{1,i} = A;
    % Extract positions where threshold is exceeded
    Cpos{1,i} = Cfil{1,i}(A);
    % Count number of instances exceeding threshold
    Cposnum(i) = nnz( Cfil{1,i} );
end

% Plot number of instances vs position in stack
plot(Cposnum(:))
xlabel('Z-index in stack')
ylabel('No. of instances matching threshold criteria')

% Create vector depicting true distance of particles from trap centre
xp=linspace(-10,10,201);
scatter(x,Cposnum)
f1=fit(xp',Cposnum','gauss1') % Fit Gaussian
plot(f1,xp,Cposnum,'o') % Plot data and fitted gaussian
xlabel('Distance from Trap Centre (\mum)')
ylabel('Particle count (instances matching threshold criteria)')
title('Distribution of Particles from Trap Centre');
```

Figure B.2: MATLAB Template Matching Code - Part 2

Simulation Details

The details of the simulation methods and parameters are presented herein. The mesh convergence was studied by varying the mesh element size and recording the obtained half-wavelength resonance frequency which converges at a maximum element size of 0.08 mm, which indicates that a mesh element size of $\lambda/12$ is adequate to resolve the acoustic wavelength.

The PZT transducer was modeled according to the piezoelectric material model (Strain-Charge form) in COMSOL by the equations:

$$S = s_E T + d^T E \tag{B.1}$$

and

$$D = dT + \epsilon_0 \epsilon_r E \tag{B.2}$$

where,
S represents the strain,
s_E is the compliance matrix (m^2/N)
E is the electric field,
d is the coupling matrix (m/V),
T is the stress (N/m^2),
D is the charge displacement (C/m^2),
ϵ_r is the relative permittivity,
ϵ_0 is the permittivity of free space.

Here, the compliance matrix s_E (m^2/N) is given by [88, 89]:

$$\begin{bmatrix} 11.75 \text{ x } 10^{-12} & -4.070 \text{ x } 10^{-12} & -4.996 \text{ x } 10^{-12} & 0 & 0 & 0 \\ -4.070 \text{ x } 10^{-12} & 14.11 \text{ x } 10^{-12} & -4.996 \text{ x } 10^{-12} & 0 & 0 & 0 \\ -4.996 \text{ x } 10^{-12} & -4.996 \text{ x } 10^{-12} & 14.11 \text{ x } 10^{-12} & 0 & 0 & 0 \\ 0 & 0 & 0 & 35.33 \text{ x } 10^{-12} & 0 & 0 \\ 0 & 0 & 0 & 0 & 35.33 \text{ x } 10^{-12} & 0 \\ 0 & 0 & 0 & 0 & 0 & 31.64 \text{ x } 10^{-12} \end{bmatrix}$$

The piezoelectric strain coefficient matrix d (m/V) is given by:

$$\begin{bmatrix} 0 & 0 & 0 & 0 & 3.89 \text{ x } 10^{-10} & 0 \\ 0 & 0 & 0 & 3.89 \text{ x } 10^{-10} & 0 & 0 \\ -1.08 \text{ x } 10^{-10} & -1.08 \text{ x } 10^{-10} & 2.53 \text{ x } 10^{-10} & 0 & 0 & 0 \end{bmatrix}$$

The relative permittivity matrix ϵ_r is given by:

$$\begin{bmatrix} 1500 & 0 & 0 \\ 0 & 1500 & 0 \\ 0 & 0 & 1200 \end{bmatrix}$$

The material properties of PIC 181 (modified PZT) are as follows:

Property (unit)	**Value**
Density ρ (kg/m^3)	7800
Speed of Sound c (m/s)	4319
Thickness (mm)	1
Diameter (mm)	10
Thickness expansion mode resonance frequency f_r (MHz)	2.1
Quality Factor Q_m	2000
Relative Permittivity in polarization direction ϵ_{33}	1200
Dielectric loss factor $tan\delta$	3
Piezoelectric Charge Coefficient d_{33} $(10^{-10}m/V)$	2.53
Elastic Compliance Coefficient S_{33}^E $(10^{-12}m^2/N)$	14.11
Electrical Capacitance (nF)	0.837
Coupling factor for thickness oscillation mode k_t	0.46

The properties of the materials used in the simulations were as follows:

Property (unit)	**Value**
Density: PDMS ρ_{PDMS} (kg/m^3)	970
Speed of sound: PDMS c_{PDMS} (m/s)	1100
Young's Modulus: PDMS E_{PDMS} (kPa)	750
Poisson's Ratio: PDMS ν_{PDMS}	0.49
Density: Glass ρ_{glass} (kg/m^3)	2210
Speed of sound: Glass c_{glass} (m/s)	5647
Young's Modulus: Glass E_{glass} (GPa)	80
Poisson's Ratio: PDMS ν_{glass}	0.2
Density: Water ρ_0 (kg/m^3)	1000
Speed of sound: Water c_0 (m/s)	1480
Compressibility: Water β_0 (GPa)	2.2
Density: Polystyrene $\rho_{polystyrene}$ (kg/m^3)	1070
Speed of sound: Polystyrene $c_{polystyrene}$ (m/s)	2340
Young's Modulus: Polystyrene $E_{polystyrene}$ (GPa)	3.7
Bulk Modulus: Polystyrene β_p (GPa)	2

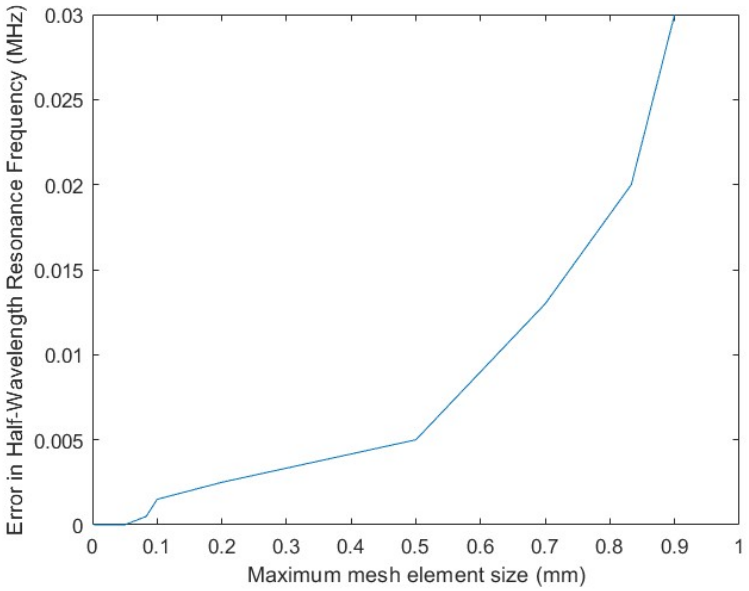

Figure B.3: Mesh Convergence Plot for Resonance Frequency

The PDMS spin coated-layer thickness was chosen on the basis of fabrication suitability (thickness adequate for bonding to glass without rupturing), and the simulations to observe the acoustic field at resonance. It can be seen from Figure B.4 that a PDMS thickness $>$ 90 μm results in an inconsistent nodal plane and a thickness below 50 μm was found to be difficult to fabricate and bond consistently. This led to a target range of approximately 60 - 100 μm which was obtained through spin-coating iterations.

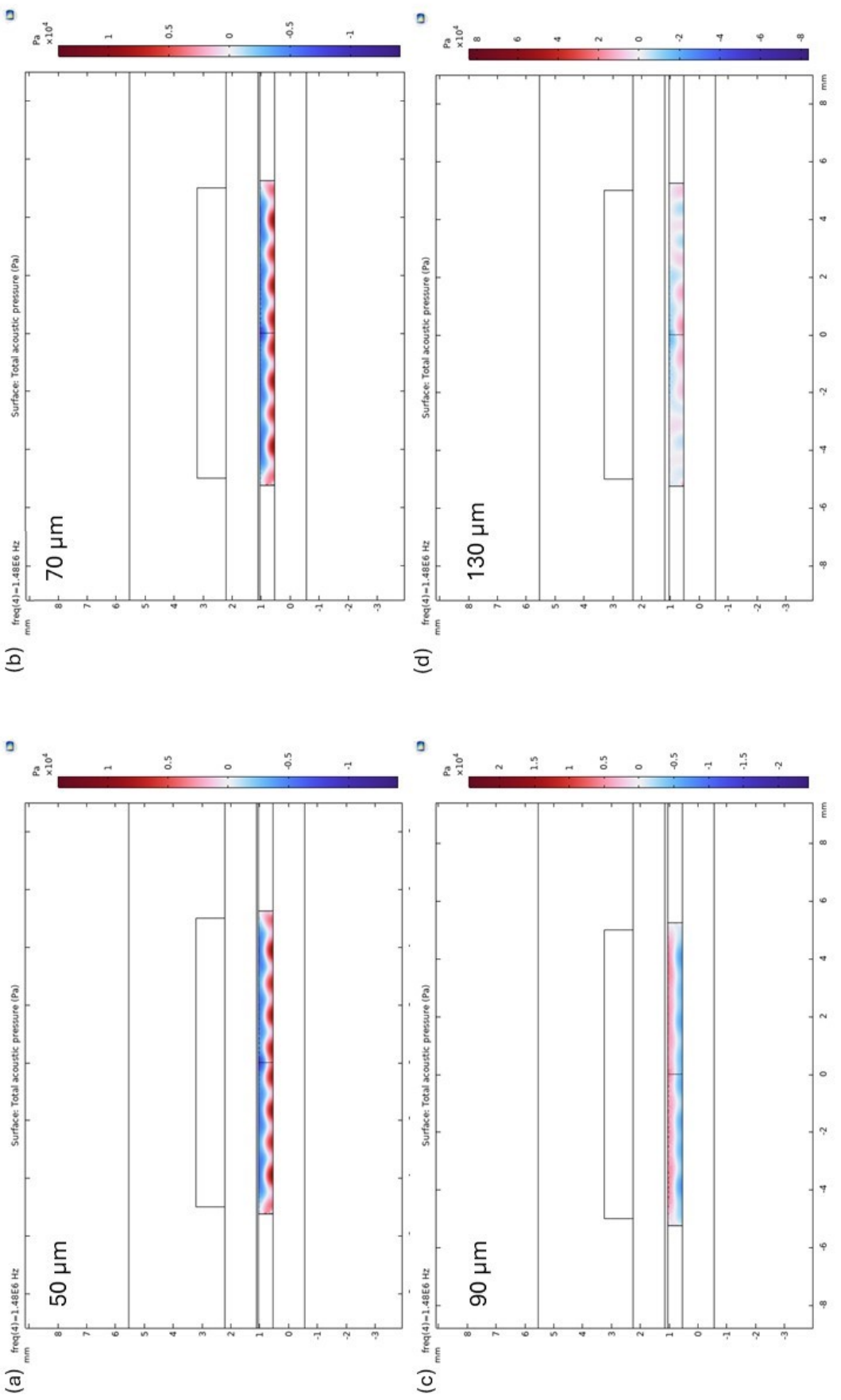

Figure B.4: The resonator acoustic field at half-wave resonance for different thicknesses of thin-PDMS.

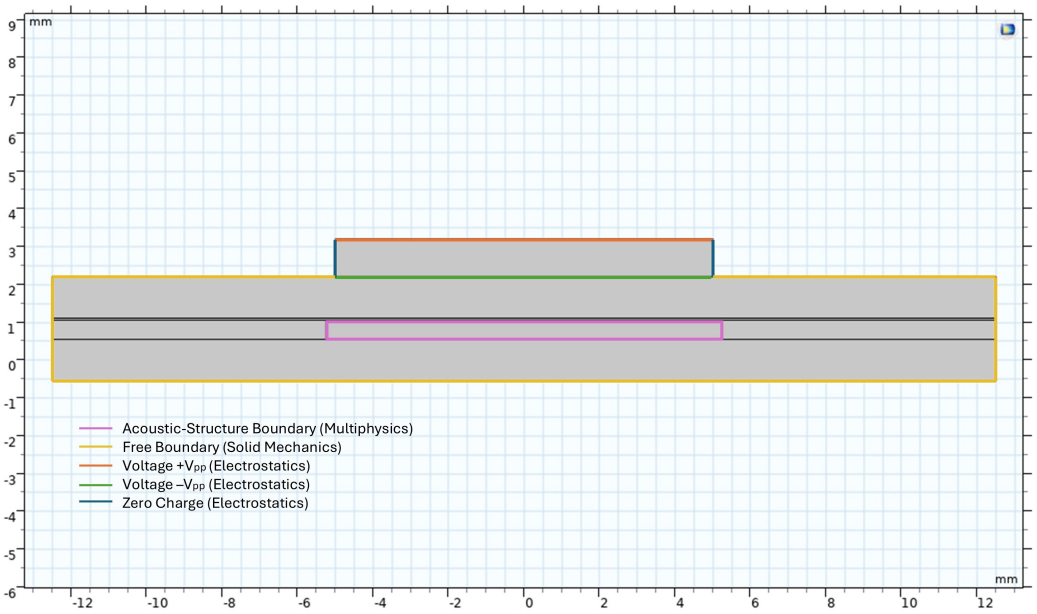

Figure B.5: Boundary Conditions used in COMSOL, pictorially.

3D Model

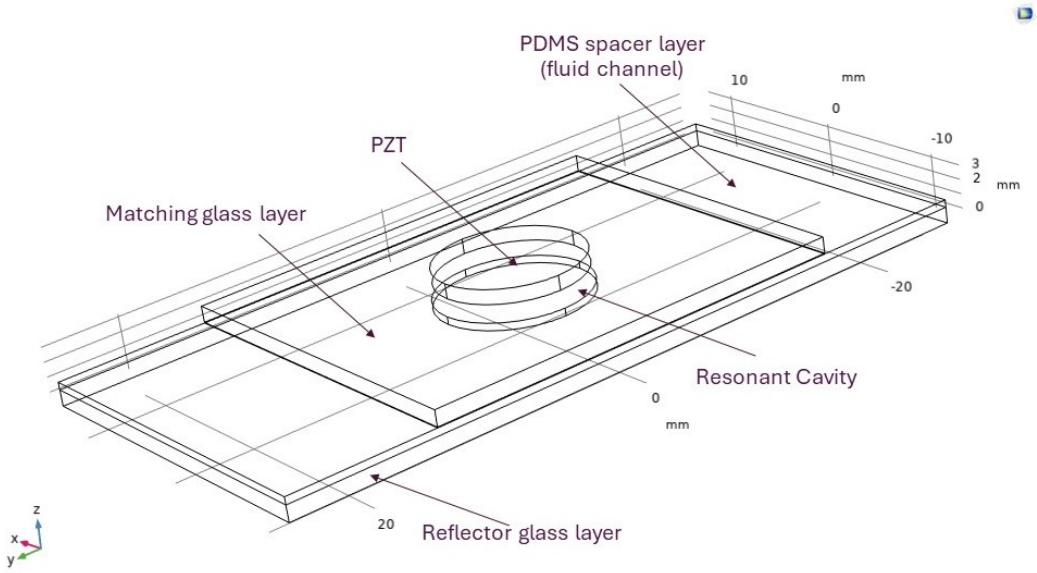

Figure B.6: 3D model of the resonator

Appendix C

Visual depiction of trapping performance: Video Links

In order to demonstrate key findings from the trapping performance visually, links to microscopic video recordings have been provided in this section.

Firstly, the impact of particle concentration and clustering onset on the extent of cluster formation can be observed. The link depicts the 'Fast agglomeration of particles on the onset of clustering.'

On the contrary, it can be observed that the interparticle interaction, and in turn the extent of clustering is lower for a low concentration of particles, as depicted in the link 'Slow interparticle interaction at low particle concentrations.'

The actuation scheme can be observed to 'Maximize Trapping Efficiency by employing a frequency sweep.' The video link depicts that the particles respond (move in response) to the acoustic field on actuation, but are eventually levitated only after a frequency sweep gradually drags most of them into the trap.

Once trapped effectively in the nodal plane, this link depicts 'The onset of cluster formation.'

It can be observed that the trapping plane shifts repeatably and predictably within the bandwidth obtained in this work. The next link depicts the 'Demonstration of shifting planes on employing the bandwidth frequency range for actuation.' The video features a trapped particle cluster, which can be seen to shift planes as the frequency is varied within the bandwidth.

The ability of long-duration actuation of the PZT was explored as an add-on step, which has been outlined later in this appendix. The video link herein shows the response of the trapped particles to 'On-Off cycles in actuation.' It can be observed that the particles are trapped immediately upon switching the field on and settle in a few seconds after switching off the acoustic field. This shows that a pulsed actuation with appropriate parameters is a potential solution in case of prolonged actuation challenges such as overheating.

LDV Animation

The Laser Doppler Vibrometry Experiments were carried out to assess the mechanical frequency response of the PZT when attached to the chip. The frequency spectrum has been included in Chapter 5, and the below links depict the mode shape extracted from the LDV measurement grids. Two different locations on the PZT surface show the same thickness expansion mode shape, the mode that is excited to create the acoustic resonance as desired.

Mode Shape-1
Mode Shape-2

Prolonged PZT actuation experiments

In order to assess the potential extrapolation of the acoustic manipulation technique to organoid cultures, a prolonged PZT actuation experiment was conducted on a sample device fabricated by the same protocol and using the same transducer. The PZT was actuated at 1.5 MHz and an input voltage of 28 V_{pp} for 10 hours. Every hour, the frequency response of the PZT was recorded. No significant change in the frequency spectrum was observed over the continuous operation, and the resonance dip appeared at 2.1 MHz consistently (as seen in Figure C.1). There was also no observable difference in the PZT and the chip appearance, the bonding of the PZT with the coupling glue layer, and the fluidic connections, indicating that the heat generated was not high enough to damage the chip, which is a promising find for long-term biological cultures. The chosen piezoceramic PIC 181 (chosen for its temperature stability) was thus found to function as expected, in a promising application direction. The solder connections were also well in place and functional until the end of the actuation period. The intact device after 10 hours of run can be seen in Figure C.2.
This indicates that there is a promising road ahead to employ this technique in live organoid cultures, with the help of add-on temperature estimation techniques and incubation facilities for further longer culture periods.

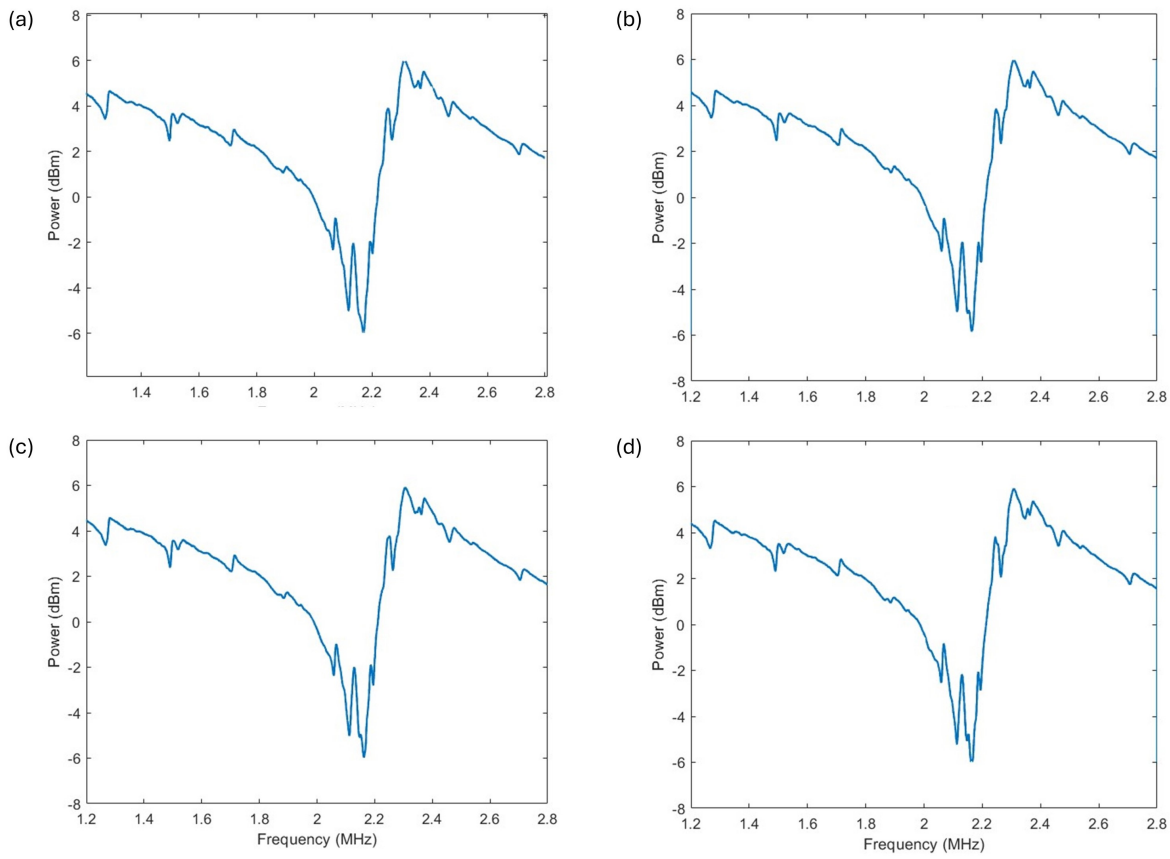

Figure C.1: Resonance characteristics over 10 hours of operation: (a) Before actuation, (b) After 3 hours of continuous actuation, (c) After 7 hours of continuous actuation, (d) After 10 hours of continuous actuation.

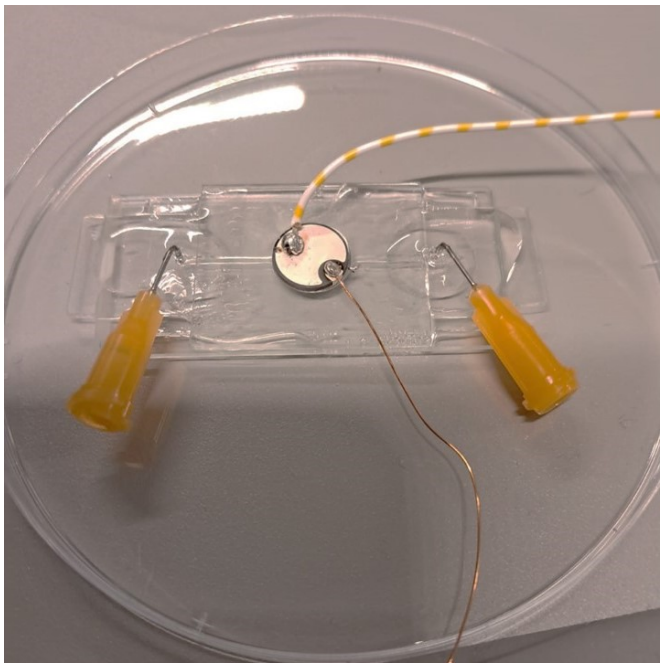

Figure C.2: Chip after 10 hours of actuation.

Images of Clusters

As discussed in Chapters 4 and 6, the nodal plane of the standing wave saw the formation of multiple secondary clusters around a larger primary cell cluster. To demonstrate this, images of the complete fluid well in two different experiments are added as links below. The images were captured using the in-built stitch function in the NIS-elements software of the microscope.

Stitched image of nodal plane- 1
Stitched image of nodal plane- 2

References

[1] Marna Eliana Sakalem et al. “Historical evolution of spheroids and organoids, and possibilities of use in life sciences and medicine”. In: *Biotechnology Journal* 16.5 (2021), p. 2000463.

[2] N Gaio et al. “A multiwell plate Organ-on-Chip (OOC) device for in-vitro cell culture stimulation and monitoring”. In: *2018 IEEE Micro Electro Mechanical Systems (MEMS)*. IEEE. 2018, pp. 314–317.

[3] Mengxi Wu et al. “Acoustofluidic separation of cells and particles”. In: *Microsystems & nanoengineering* 5.1 (2019), p. 32.

[4] Ghulam Destgeer et al. “Microchannel anechoic corner for microparticle manipulation via travelling surface acoustic waves”. In: *Physics Procedia* 70 (2015), pp. 30–33.

[5] Adem Ozcelik et al. “Acoustic tweezers for the life sciences”. In: *Nature methods* 15.12 (2018), pp. 1021–1028.

[6] Wenxing Liu et al. “A review on particle assembly in standing wave acoustic field”. In: *Journal of Nanoparticle Research* 24.4 (2022), p. 81.

[7] David J Collins et al. “Two-dimensional single-cell patterning with one cell per well driven by surface acoustic waves”. In: *Nature communications* 6.1 (2015), p. 8686.

[8] Charis-P Segeritz and Ludovic Vallier. “Cell culture: Growing cells as model systems in vitro”. In: *Basic science methods for clinical researchers*. Elsevier, 2017, pp. 151–172.

[9] Caleb Jensen and Yong Teng. “Is it time to start transitioning from 2D to 3D cell culture?” In: *Frontiers in molecular biosciences* 7 (2020), p. 33.

[10] Flaminia Kaluthantrige Don and Meritxell Huch. “Organoids, where we stand and where we go”. In: *Trends in molecular medicine* 27.5 (2021), pp. 416–418.

[11] Sung-Min Kang et al. “Engineered microsystems for spheroid and organoid studies”. In: *Advanced healthcare materials* 10.2 (2021), p. 2001284.

[12] Mariangela Scalise et al. “From spheroids to organoids: the next generation of model systems of human cardiac regeneration in a dish”. In: *International journal of molecular sciences* 22.24 (2021), p. 13180.

[13] Annett Klinder et al. “Comparison of different cell culture plates for the enrichment of non-adherent human mononuclear cells”. In: *Experimental and Therapeutic Medicine* 17.3 (2019), pp. 2004–2012.

[14] Julia Tischler et al. “An automated do-it-yourself system for dynamic stem cell and organoid culture in standard multi-well plates”. In: *Cell reports methods* 2.7 (2022).

[15] Moritz Hofer and Matthias P Lutolf. “Engineering organoids”. In: *Nature Reviews Materials* 6.5 (2021), pp. 402–420.

[16] Zixuan Zhao et al. “Organoids”. In: *Nature Reviews Methods Primers* 2.1 (2022), p. 94.

[17] Weijie Peng et al. “Challenges in bio-fabrication of organoid cultures”. In: *Cell Biology and Translational Medicine, Volume 3: Stem Cells, Bio-materials and Tissue Engineering* (2018), pp. 53–71.

[18] Maria Tenje et al. “A practical guide to microfabrication and patterning of hydrogels for biomimetic cell culture scaffolds”. In: *Organs-on-a-Chip* 2 (2020), p. 100003.

[19] Mark W Tibbitt and Kristi S Anseth. “Hydrogels as extracellular matrix mimics for 3D cell culture”. In: *Biotechnology and bioengineering* 103.4 (2009), pp. 655–663.

[20] Steven R Caliari and Jason A Burdick. “A practical guide to hydrogels for cell culture”. In: *Nature methods* 13.5 (2016), pp. 405–414.

[21] Clement Rieu et al. “Topotactic fibrillogenesis of freeze-cast microridged collagen scaffolds for 3D cell culture”. In: *ACS applied materials & interfaces* 11.16 (2019), pp. 14672–14683.

[22] Fahima Akther et al. “Hydrogels as artificial matrices for cell seeding in microfluidic devices”. In: *RSC advances* 10.71 (2020), pp. 43682–43703.

[23] Ferdinand Ruedinger et al. “Hydrogels for 3D mammalian cell culture: a starting guide for laboratory practice”. In: *Applied microbiology and biotechnology* 99 (2015), pp. 623–636.

[24] Hongwei Cai et al. “Intelligent acoustofluidics enabled mini-bioreactors for human brain organoids”. In: *Lab on a Chip* 21.11 (2021), pp. 2194–2205.

[25] Joana Costa et al. “Bioreactor with electrically deformable curved membranes for mechanical stimulation of cell cultures”. In: *Frontiers in Bioengineering and Biotechnology* 8 (2020), p. 22.

[26] João Meneses et al. “A multimodal stimulation cell culture bioreactor for tissue engineering: A numerical modelling approach”. In: *Polymers* 12.4 (2020), p. 940.

[27] Richard Novak et al. *Microfluidic devices and systems for cell culture and/or assay*. US Patent 11,229,910. Jan. 2022.

[28] David Wendt et al. “Potential and bottlenecks of bioreactors in 3D cell culture and tissue manufacturing”. In: *Advanced materials* 21.32-33 (2009), pp. 3352–3367.

[29] Yoshikatsu Akiyama. “Design of temperature-responsive cell culture surfaces for cell sheet engineering”. In: *Cyborg and Bionic Systems* (2021).

[30] Toshiyuki Owaki et al. “Cell sheet engineering for regenerative medicine: current challenges and strategies”. In: *Biotechnology journal* 9.7 (2014), pp. 904–914.

[31] Ayidah Alghuwainem, Alaa T Alshareeda, and Batla Alsowayan. “Scaffold-free 3-D cell sheet technique bridges the gap between 2-D cell culture and animal models”. In: *International journal of molecular sciences* 20.19 (2019), p. 4926.

[32] Resmi Raju et al. “Three-dimensional periodontal tissue regeneration using a bone-ligament complex cell sheet”. In: *Scientific Reports* 10.1 (2020), p. 1656.

[33] Jun Kobayashi et al. “Cell sheet tissue engineering: cell sheet preparation, harvesting/manipulation, and transplantation”. In: *Journal of biomedical materials research Part A* 107.5 (2019), pp. 955–967.

[34] Chin-Yi Cho et al. “Development of a novel hanging drop platform for engineering controllable 3D microenvironments”. In: *Frontiers in Cell and Developmental Biology* 8 (2020), p. 327.

[35] TE De Groot et al. “Surface-tension driven open microfluidic platform for hanging droplet culture”. In: *Lab on a Chip* 16.2 (2016), pp. 334–344.

[36] Issac J Michael et al. “Surface-engineered paper hanging drop chip for 3D spheroid culture and analysis”. In: *ACS applied materials & interfaces* 10.40 (2018), pp. 33839–33846.

[37] Wenqian Feng, Erica Ueda, and Pavel A Levkin. “Droplet Microarrays: From Surface Patterning to High-Throughput Applications”. In: *Advanced materials* 30.20 (2018), p. 1706111.

[38] AI Neto et al. “A novel hanging spherical drop system for the generation of cellular spheroids and high throughput combinatorial drug screening”. In: *Biomaterials science* 3.4 (2015), pp. 581–585.

[39] Linfen Yu, Michael CW Chen, and Karen C Cheung. “Droplet-based microfluidic system for multicellular tumor spheroid formation and anticancer drug testing”. In: *Lab on a Chip* 10.18 (2010), pp. 2424–2432.

[40] Madeline G Andrews and Arnold R Kriegstein. “Challenges of organoid research”. In: *Annual Review of Neuroscience* 45 (2022), pp. 23–39.

[41] Paul Rowe, Adam Koller, and Sandeep Sharma. “Physiology, bone remodeling”. In: (2018).

[42] Oriane B Matthys, Ana C Silva, and Todd C McDevitt. “Engineering human organoid development ex vivo—challenges and opportunities”. In: *Current Opinion in Biomedical Engineering* 13 (2020), pp. 160–167.

[43] Jay Gopalakrishnan. “The emergence of stem cell-based brain organoids: trends and challenges”. In: *BioEssays* 41.8 (2019), p. 1900011.

[44] Aswathi Ashok et al. “Towards manufacturing of human organoids”. In: *Biotechnology advances* 39 (2020), p. 107460.

[45] Anil Sebastian, Anne-Marie Buckle, and Gerard H Markx. “Tissue engineering with electric fields: Immobilization of mammalian cells in multilayer aggregates using dielectrophoresis”. In: *Biotechnology and bioengineering* 98.3 (2007), pp. 694–700.

[46] Vi-hung Tsan et al. “Low-cost acoustic force trap in a microfluidic channel”. In: *HardwareX* 14 (2023), e00428.

[47] Vi-hung Tsan. *Numerical and experimental trapping analysis of simple and cost-effective acoustic tweezers*. 2022.

[48] Tingkuan Miao et al. “High-throughput fabrication of cell spheroids with 3D acoustic assembly devices”. In: *International Journal of Bioprinting* 9.4 (2023).

[49] AG Guex et al. “The waves that make the pattern: a review on acoustic manipulation in biomedical research”. In: *Materials Today Bio* 10 (2021), p. 100110.

[50] Gihoon Choi, Zifan Tang, and Weihua Guan. “Microfluidic high-throughput single-cell mechanotyping: Devices and applications”. In: *Nanotechnology and Precision Engineering (NPE)* 4.4 (2021).

[51] Karl Olofsson, Björn Hammarström, and Martin Wiklund. “Acoustic separation of living and dead cells using high density medium”. In: *Lab on a chip* 20.11 (2020), pp. 1981–1990.

[52] Yuliang Xie, Hunter Bachman, and Tony Jun Huang. “Acoustofluidic methods in cell analysis”. In: *TrAC Trends in Analytical Chemistry* 117 (2019), pp. 280–290.

[53] Wei Wei et al. “Microscale acoustic streaming for biomedical and bioanalytical applications”. In: *TrAC Trends in Analytical Chemistry* 160 (2023), p. 116958.

[54] Asier Marzo. “Standing waves for acoustic levitation”. In: *Acoustic Levitation: From Physics to Applications* (2020), pp. 11–26.

[55] Jun Huang Tony Zhang Peiran. *Acoustofluidic systems including acoustic wave generators for manipulating fluids, droplets, and micro/nano objects within a fluid suspension and related methods*. U.S. pat. Feb. 14, 2023.

[56] Chang Tian et al. “Recent advances in microfluidic technologies for organ-on-a-chip”. In: *TrAC Trends in Analytical Chemistry* 117 (2019), pp. 146–156.

[57] Zhuhao Wu et al. “Scaffold-free generation of heterotypic cell spheroids using acoustofluidics”. In: *Lab on a Chip* 21.18 (2021), pp. 3498–3508.

[58] Misa Nakao et al. “Formation of large scaffold-free 3-D aggregates in a cell culture dish by ultrasound standing wave trapping”. In: *Ultrasound in Medicine & Biology* 45.5 (2019), pp. 1306–1315.

[59] Jiyang Mei et al. “Well-free agglomeration and on-demand three-dimensional cell cluster formation using guided surface acoustic waves through a couplant layer”. In: *Biomedical Microdevices* 24.2 (2022), p. 18.

[60] Marialaura Serzanti et al. “Arrangement of Live Human Cells through Acoustic Waves Generated by Piezoelectric Actuators for Tissue Engineering Applications”. In: *Applied Sciences* 10.10 (2020), p. 3477.

[61] Nathan Jeger-Madiot et al. “Self-organization and culture of Mesenchymal Stem Cell spheroids in acoustic levitation”. In: *Scientific reports* 11.1 (2021), p. 8355.

[62] Chloé Dupuis et al. “Towards concentric topology in organoids: Structuration and culture of brain derived spheroids in a Bulk Acoustic Wave resonator”. In: *26th International Conference on Miniaturized Systems for Chemistry and Life Sciences (MicroTAS 2022)*. 2022.

[63] Kejie Chen et al. “Rapid formation of size-controllable multicellular spheroids via 3D acoustic tweezers”. In: *Lab on a Chip* 16.14 (2016), pp. 2636–2643.

[64] Subra Suresh et al. *Three-dimensional acoustic manipulation of cells*. US Patent App. 16/071,641. Jan. 2019.

[65] Dhananjay V Deshmukh et al. “Continuous production of acoustically patterned cells within hydrogel fibers for musculoskeletal tissue engineering”. In: *Advanced Functional Materials* 32.30 (2022), p. 2113038.

[66] Deming Jiang et al. “Surface acoustic wave (SAW) techniques in tissue engineering”. In: *Cell and Tissue Research* 386.2 (2021), pp. 215–226.

[67] Zhichao Ma et al. “Acoustic holographic cell patterning in a biocompatible hydrogel”. In: *Advanced Materials* 32.4 (2020), p. 1904181.

[68] Vivien Marx. “Biophysics: using sound to move cells”. In: *Nature methods* 12.1 (2015), pp. 41–44.

[69] Citsabehsan Devendran, David J Collins, and Adrian Neild. “The role of channel height and actuation method on particle manipulation in surface acoustic wave (SAW)-driven microfluidic devices”. In: *Microfluidics and Nanofluidics* 26.2 (2022), p. 9.

[70] Ivo Leibacher, Peter Reichert, and Jürg Dual. “Microfluidic droplet handling by bulk acoustic wave (BAW) acoustophoresis”. In: *Lab on a Chip* 15.13 (2015), pp. 2896–2905.

[71] Pengfei Liu et al. “Acoustic trapping with 3-D manipulation”. In: *Applied Acoustics* 155 (2019), pp. 216–221.

[72] Alireza Barani et al. “Microfluidic integrated acoustic waving for manipulation of cells and molecules”. In: *Biosensors and Bioelectronics* 85 (2016), pp. 714–725.

[73] SS Sadhal. “Acoustofluidics 13: Analysis of acoustic streaming by perturbation methods”. In: *Lab on a Chip* 12.13 (2012), pp. 2292–2300.

[74] Alexander A Doinikov. “Acoustic radiation forces: Classical theory and recent advances”. In: *Recent Res. Dev. Acoust* 1 (2003), pp. 39–67.

[75] SS Sadhal. “Acoustofluidics 15: Streaming with sound waves interacting with solid particles”. In: *Lab on a Chip* 12.15 (2012), pp. 2600–2611.

[76] Louis Vessot King. “On the acoustic radiation pressure on spheres”. In: *Proceedings of the Royal Society of London. Series A-Mathematical and Physical Sciences* 147.861 (1934), pp. 212–240.

[77] LP Gor’kov. “On the acoustic radiation pressure on spheres”. In: *Sov. Phys. Dokl*. Vol. 6. 1962, p. 773.

[78] Mikkel Settnes and Henrik Bruus. “Forces acting on a small particle in an acoustical field in a viscous fluid”. In: *Physical Review E—Statistical, Nonlinear, and Soft Matter Physics* 85.1 (2012), p. 016327.

[79] MAH Weiser, RE Apfel, and EA Neppiras. “Interparticle forces on red cells in a standing wave field”. In: *Acta Acustica united with Acustica* 56.2 (1984), pp. 114–119.

[80] Martin Gröschl. “Ultrasonic separation of suspended particles-Part I: Fundamentals”. In: *Acta Acustica united with Acustica* 84.3 (1998), pp. 432–447.

[81] MT Pigott and RC Strum. “Observed onset of acoustic streaming”. In: *The Journal of the Acoustical Society of America* 41.3 (1967), pp. 662–665.

[82] Mathias Ohlin et al. “Controlling acoustic streaming in a multi-well microplate for improving live cell assays”. In: *Proceedings of the 15th International Conference on Miniaturized Systems for Chemistry and Life, Sciences (MicroTAS 2011), Seattle, WA, USA*. 2011, pp. 2–6.

[83] JF Spengler, WT Coakley, and KT Christensen. “Microstreaming effects on particle concentration in an ultrasonic standing wave”. In: *AIChE journal* 49.11 (2003), pp. 2773–2782.

[84] Larisa A Kuznetsova and W Terence Coakley. “Microparticle concentration in short path length ultrasonic resonators: Roles of radiation pressure and acoustic streaming”. In: *The Journal of the Acoustical Society of America* 116.4 (2004), pp. 1956–1966.

[85] Johannes F Spengler and W Terence Coakley. “Ultrasonic trap to monitor morphology and stability of developing microparticle aggregates”. In: *Langmuir* 19.9 (2003), pp. 3635–3642.

[86] Peter Glynne-Jones, Rosemary J Boltryk, and Martyn Hill. “Acoustofluidics 9: Modelling and applications of planar resonant devices for acoustic particle manipulation”. In: *Lab on a Chip* 12.8 (2012), pp. 1417–1426.

[87] Andreas Lenshof et al. “Acoustofluidics 5: Building microfluidic acoustic resonators”. In: *Lab on a Chip* 12.4 (2012), pp. 684–695.

[88] J Pohl et al. “Experimental and theoretical analysis of Lamb wave generation by piezoceramic actuators for structural health monitoring”. In: *Experimental Mechanics* 52 (2012), pp. 429–438.

[89] Physik Instrumente GmbH. *Piezoceramic Disks, Rods Cylinders*. July 2024. URL: https://www.piceramic.com/en/products/piezoceramic-components/disks-rods-and-cylinders.

[90] Giorgio Gianini Morbioli, Nicholas Colby Speller, and Amanda M Stockton. “A practical guide to rapid-prototyping of PDMS-based microfluidic devices: A tutorial”. In: *Analytica chimica acta* 1135 (2020), pp. 150–174.

[91] Elveflow. *PDMS Membrane: Thickness of a spin-coated PDMS-layer*. July 2024. URL: https://www.elveflow.com/microfluidic-reviews/soft-lithography-microfabrication/pdms-membrane-thickness-of-a-spin-coated-pdms-layer/.

[92] Sara Carcangiu, Augusto Montisci, and Renato Forcinetti. “Numerical Simulation of Wave Propagation”. In: *Ultrasonic Nondestructive Evaluation Systems: Industrial Application Issues*. Ed. by Pietro Burrascano et al. Cham: Springer International Publishing, 2015, pp. 17–45. ISBN: 978-3-319-10566-6. DOI: 10.1007/978-3-319-10566-6_2. URL: https://doi.org/10.1007/978-3-319-10566-6_2.

[93] Polytec GmbH. *Laser Doppler Vibrometry*. July 2024. URL: https://www.polytec.com/us/vibrometry/technology/laser-doppler-vibrometry.

[94] Jurg Dual and Dirk Möller. “Acoustofluidics 4: Piezoelectricity and application in the excitation of acoustic fields for ultrasonic particle manipulation”. In: *Lab on a Chip* 12.3 (2012), pp. 506–514.

[95] Henrik Bruus. “Acoustofluidics 7: The acoustic radiation force on small particles”. In: *Lab on a Chip* 12.6 (2012), pp. 1014–1021.

[96] Henrik Bruus. “Acoustofluidics 10: Scaling laws in acoustophoresis”. In: *Lab on a Chip* 12.9 (2012), pp. 1578–1586.

[97] Martin Wiklund, Roy Green, and Mathias Ohlin. “Acoustofluidics 14: Applications of acoustic streaming in microfluidic devices”. In: *Lab on a Chip* 12.14 (2012), pp. 2438–2451.

[98] Jungwoo Lee, Changyang Lee, and K Kirk Shung. “Calibration of sound forces in acoustic traps”. In: *IEEE transactions on ultrasonics, ferroelectrics, and frequency control* 57.10 (2010), pp. 2305–2310.

[99] Jungwoo Lee, Jong Seob Jeong, and K Kirk Shung. “Microfluidic acoustic trapping force and stiffness measurement using viscous drag effect”. In: *Ultrasonics* 53.1 (2013), pp. 249–254.

[100] Hae Gyun Lim et al. “Calibration of trapping force on cell-size objects from ultrahigh-frequency single-beam acoustic tweezer”. In: *IEEE transactions on ultrasonics, ferroelectrics, and frequency control* 63.11 (2016), pp. 1988–1995.

[101] John P Lewis. “Fast normalized cross-correlation”. In: *Vision interface*. Vol. 10. 1. 1995, pp. 120–123.

[102] Alon Grinenko. *How to Compute the Acoustic Radiation Force by Perturbation Methods*. July 2024. URL: https://www.comsol.com/blogs/how-to-compute-the-acoustic-radiation-force.

[103] SM Zareei et al. “Three-dimensional numerical simulation of particle acoustophoresis: COMSOL implementation and case studies”. In: *Engineering with Computers* 39.1 (2023), pp. 735–750.

[104] Ce Wang et al. “Acoustic 3D trapping of microparticles in flowing liquid using circular cavity”. In: *Sensors and Actuators A: Physical* 363 (2023), p. 114698.

[105] Michaël Baudoin and J-L Thomas. “Acoustic tweezers for particle and fluid micromanipulation”. In: *Annual Review of Fluid Mechanics* 52.1 (2020), pp. 205–234.

[106] Thierry Baasch, Ivo Leibacher, and Jürg Dual. “Multibody dynamics in acoustophoresis”. In: *The Journal of the Acoustical Society of America* 141.3 (2017), pp. 1664–1674.

[107] D Bazou et al. “Long-term viability and proliferation of alginate-encapsulated 3-D HepG2 aggregates formed in an ultrasound trap”. In: *Toxicology in Vitro* 22.5 (2008), pp. 1321–1331.

[108] Charlène Bouyer et al. “A bio-acoustic levitational (BAL) assembly method for engineering of multilayered, 3D brain-like constructs, using human embryonic stem cell derived neuro-progenitors.” In: *Advanced Materials (Deerfield Beach, Fla.)* 28.1 (2015), pp. 161–167.

[109] Lucile Rabiet et al. “Acoustic levitation as a tool for cell-driven self-organization of human cell spheroids during long-term 3D culture”. In: *Biotechnology and Bioengineering* 121.4 (2024), pp. 1421–1433.

[110] Mauricio Hoyos and Angélica Castro. “Controlling the acoustic streaming by pulsed ultrasounds”. In: *Ultrasonics* 53.1 (2013), pp. 70–76.

[111] Angelica Castro and Mauricio Hoyos. “Study of the onset of the acoustic streaming in parallel plate resonators with pulse ultrasound”. In: *Ultrasonics* 66 (2016), pp. 166–171.

[112] Zuzana Sumbalova Koledova. “3D Cell Culture: Techniques For and Beyond Organoid Applications”. In: *3D Cell Culture: Methods and Protocols*. Springer, 2024, pp. 1–12.

[113] Despina Bazou et al. “Gene expression analysis of mouse embryonic stem cells following levitation in an ultrasound standing wave trap”. In: *Ultrasound in medicine & biology* 37.2 (2011), pp. 321–330.

[114] Gayatri P Gautam et al. “Simple and inexpensive micromachined aluminum microfluidic devices for acoustic focusing of particles and cells”. In: *Analytical and bioanalytical chemistry* 410 (2018), pp. 3385–3394.

[115] Maurits Wassenaar. “The Silent Force: Acoustic Trapping in Microfluidics: Exploring the Design and Fabrication of an Acoustofluidic Device for Microbead Trapping and Manipulation”. In: *TU Delft Repository* (2023).

[116] Changhan Yoon et al. “Multi-particle trapping and manipulation by a high-frequency array transducer”. In: *Applied Physics Letters* 105.21 (2014).

[117] Kanji Ono. “A comprehensive report on ultrasonic attenuation of engineering materials, including metals, ceramics, polymers, fiber-reinforced composites, wood, and rocks”. In: *Applied Sciences* 10.7 (2020), p. 2230.

[118] Paul Wrede et al. “Acoustic trapping and manipulation of hollow microparticles under fluid flow using a single-lens focused ultrasound transducer”. In: *ACS Applied Materials & Interfaces* 15.45 (2023), pp. 52224–52236.

[119] Martin Wiklund. “Ultrasonic enrichment of microparticles in bioaffinity assays”. PhD thesis. Fysik, 2004.

[120] Vincent Miralles et al. “A review of heating and temperature control in microfluidic systems: techniques and applications”. In: *Diagnostics* 3.1 (2013), pp. 33–67.

[121] Qi Zhang et al. “Glass 3D printing of microfluidic pressure sensor interrogated by fiber-optic refractometry”. In: *IEEE Photonics Technology Letters* 32.7 (2020), pp. 414–417.

[122] Carlos DS Brites et al. “Thermometry at the nanoscale”. In: *Nanoscale* 4.16 (2012), pp. 4799–4829.

[123] Jiyu Meng et al. “Microfluidics temperature compensating and monitoring based on liquid metal heat transfer”. In: *Micromachines* 13.5 (2022), p. 792.